

PORATION OF BIOLOGICAL MEMBRANES BY ANTIMICROBIAL PEPTIDES AND
PRESSURE, INSIGHTS FROM COMPUTER SIMULATIONS

Ardeshir Goliaei

A dissertation submitted to the faculty of the University of North Carolina at Chapel Hill in
partial fulfillment of requirements for the degree of Doctor of Philosophy in the Department of
Biochemistry and Biophysics.

Chapel Hill
2016

Approved by:

Max Berkowitz

Barry Lentz

Brian Kuhlman

Qi Zhang

Alexander Tropsha

© 2016
Ardeshir Goliaei
ALL RIGHTS RESERCED

ABSTRACT

**Ardeshir Goliaei: Poration of Biological Membranes by Antimicrobial Peptides and Pressure,
Insights from Computer Simulations
(Under the direction of Max L. Berkowitz)**

The plasma membrane is the boundary of the cell that separates the outside world from its interior. It is the first barrier that any exogenous compound faces upon transferring to the cytoplasm. Additionally, this boundary plays a variety of biochemical roles for the cell including energy transfer, signal transduction, solute transport, etc. Lipids, proteins, and carbohydrates are three major components of the plasma membrane and their type and percentage differs depending on the specific cell, organelle, or tissue type.

The fact that the plasma membrane keeps the integrity of the cell intact can play different potential therapeutical roles depending on the context; opening or disturbing the barrier versus healing or repairing it. More specifically, when the cell membrane we approach belongs to an opportunistic organism such as a bacterium or a virus, we tend to disturb the integrity of their membrane to damage the invading organism (antibiotic therapy). On the other hand, in the context of exposure of the neuron cells to uncontrolled shock waves (blast waves) we tend to avoid damage to the cell membrane since the outcome correlates with brain damage and psychological complications. Understanding the underlying mechanisms for restoring the integrity of a damaged plasma membrane using certain compounds (e.g. polymers) provides invaluable information in our therapeutical approaches.

There are a variety of experimental methods available for membrane research such as X-ray and neutron scattering, AFM, Fluorescence probing, and NMR. Additionally, molecular dynamics computer simulations can also be used in different research settings, to provide more atomistic insight into the processes that take place in the plasma membrane. A variety of force fields are available which provide different levels of atomic representation of the system in question and open the door for more detailed understanding of the nature of the cell membrane and how it behaves.

In this thesis, we used molecular dynamics computer simulations to ask two major questions. First, what mechanisms are involved in opening of the plasma membrane? We studied Antimicrobial peptides (AMPs) and how their mechanism of action can be envisioned by computer simulations. We also investigated shock wave induced nano-bubble collapse and its impact on the plasma membrane. Second, what mechanisms membrane sealants employ to restore the integrity of a damaged membrane? More specifically, we provided molecular pictures of the process of membrane sealing by triblock co-polymers, or Poloxamers.

ACKNOWLEDGMENTS

I would like to express my most sincere gratefulness to my PhD advisor Prof. Max Berkowitz for his generous and constant support throughout my work. Whether it was a scientific question or a personal one, he was always available with helpful comments, ideas, and guidance. I sincerely cannot imagine having a better advisor during my PhD program. I can confidently say that he knew what I liked to do, even better than myself. That is why we had such an amazing communication and his guidance has helped me so significantly.

Very sincerely, I would like to express my gratitude to Prof. Barry Lentz and Lisa Phillippie, for their outstanding support and help during my graduate life. I cannot thank Barry enough for his mentorship, support, and guidance in finding the best lab for my research and throughout my graduate work. The amount of care and attention that I have received from him is beyond my expectations. Additionally, Lisa has played a tremendous role in shaping my graduate time at UNC. At any time that I needed help and advice she was always available with open arms and that means a lot to me. Simply, without Barry and Lisa, continuing graduate school would have been impossible for me and for that reason I am very grateful to both of them.

I would like to thank all the members of my committee Professors Barry Lentz, Brian Kuhlman, Alexander Tropsha, and Qi Zhang for their valuable guidance and support. I appreciate all their help and time. In particular, I would like to thank Prof. Alexander Tropsha. Alex has always been nice to me. He has played a significant role in my professional

development. He was always available when I needed help and advice and I have used his guidance to be a better thinker and a more independent researcher. I appreciate his time and help.

I would also like to thank Sheeba Irudayam, Santo Kolattukudy Poulouse, and Upendra Adhikari, all the members of Berkowitz group. I have always had scientific discussion and fruitful collaborations with them. In addition I would like to thank all my friends and administrative staff in the Department of Biochemistry and Biophysics, the Program in Molecular and Cellular Biophysics, the Program in Bioinformatics and Computational Biology (BCB), and the Biological and Biomedical Sciences Program (BBSP).

Finally, my sincere gratitude and love goes to my mother Sakineh Rineh and my sister Forough Goliaei. Imagining a world without them is close to impossible. What my mother has thought me is love, and she is an illustrative example of it.

TABLE OF CONTENTS

	Page
TABLE OF CONTENTS.....	vii
LIST OF TABLES	xi
LIST OF FIGURES	xii
LIST OF ABBREVIATIONS.....	xv
CHAPTER 1: INTRODUCTION	1
1.1 Plasma membrane and its importance.....	1
1.2 The plasma membrane and its therapeutic potentials	2
1.3 Tools and techniques used for plasma membrane research	3
1.4 Molecular dynamics computer simulation technique	4
1.5 The research goals and approaches taken in this study.....	5
1.6 What mechanisms are involved in opening of the plasma membrane?	6
1.6.1 Antimicrobial peptides (AMPs).....	6
1.6.2 Shock wave induced nano-bubble collapse and its impact on the plasma membrane	7
1.7 What mechanisms membrane sealants employ to restore the integrity of a damaged membrane?	8
CHAPTER 2: LOCAL PRESSURE CHANGES IN LIPID BILAYERS DUE TO ADSORPTION OF MELITTIN AND MAGAININ-H2 ANTIMICROBIAL PEPTIDES: RESULTS FROM COMPUTER SIMULATIONS	11
2.1 Introduction.....	11
2.2 Methods.....	14

2.3 Results and Discussion	18
2.3.1 Membranes Containing 12 AMPs ($P/L = 1/50$).....	18
2.3.2 Membranes Containing 18 AMPs ($P/L = 3/100$).....	20
2.4 Conclusions.....	21
 CHAPTER 3: MECHANISM OF MEMBRANE PORATION BY SHOCK WAVE INDUCED NANOBUBBLE COLLAPSE: A MOLECULAR DYNAMICS STUDY	
3.1 Introduction.....	29
3.2 Methods.....	32
3.3 Results.....	34
3.3.1 Shock Wave Simulations with Particle Velocity (v_p) = 1.0 km/s	35
3.3.1.1 (a) Simulations with $\tau_s = 3$ ps.....	35
3.3.1.2 (b) $\tau_s = 5$ ps.....	39
3.3.2 Shock Wave Simulations with Particle Velocity (v_p) = 0.5 km/s	40
3.3.3 Shock Wave Simulations with a Smaller Nanobubble (Diameter, $D = 20$ nm).....	41
3.3.4 Spontaneous Nanobubble Collapse (without Shock Wave)	42
3.4 Discussions and Summary	43
 CHAPTER 4: OPENING OF THE BLOOD-BRAIN BARRIER TIGHT JUNCTION DUE TO SHOCK WAVE INDUCED BUBBLE COLLAPSE: A MOLECULAR DYNAMICS SIMULATION STUDY	
4.1 Introduction.....	70
4.2 Results and Discussion	72
4.3 Conclusion	76
4.4 Methods.....	76
 CHAPTER 5: PROPERTIES OF POLOXAMER MOLECULES AND POLOXAMER MICELLES DISSOLVED IN WATER AND NEXT TO LIPID BILAYERS: RESULTS FROM COMPUTER SIMULATIONS.....	
	85

5.1 Introduction.....	85
5.2 Methods.....	88
5.2.1 Coarse-Grained Force Field.....	88
5.2.2 Setup of Molecular Dynamics (MD) Runs	88
5.2.3 Simulations of Poloxamers in Bulk water.....	89
5.2.4 Simulations of Poloxamers in the Presence of a Bilayer Membrane	90
5.2.5 Simulations of Poloxamer Micelles in the Presence of a Bilayer Membrane Containing a Pore	91
5.3 Results and Discussion	91
5.3.1 Radii of Gyration (R_g)	91
5.3.2 Interaction of Poloxamers with Membrane.....	92
5.3.3 Interaction of Poloxamer Micelles with the DMPC Bilayer.....	94
5.3.4 Does the P188 Micelle Seal the Pores in the Membrane?	94
5.4 Summary	96
 CHAPTER 6: BEHAVIOR OF P85 AND P188 POLOXAMER MOLECULES: COMPUTER SIMULATIONS USING UNITED-ATOM FORCE-FIELD	
6.1 Introduction.....	109
6.2 Methods.....	112
6.2.1 United-Atom Force-Field Parameters.....	112
6.2.2 Molecular Dynamics Simulations.....	113
6.3 Results.....	117
6.3.1 Simulations of P85 and P188 in Water	117
6.3.2 Simulations of P85 and P188 at the Air/Water Interface.....	118
6.3.3 Interaction of P85 and P188 Poloxamers with the DLPC Model Membrane	119
6.3.4 Self-Assembly of P85 Poloxamers, DLPC Lipid Monomers, and Water	120

6.3.5 Interaction of P85 and P188 Poloxamers with Damaged DLPC Model Membrane.....	121
6.4 Discussion and Conclusions	122
Thesis conclusions and future directions	139

LIST OF TABLES

	Page
Table 3.1: Summary of the results from shock wave simulations.	46
Table 4.1. Impulse and velocity of the shock wave at the time when it hits the bilayer for different piston stopping time (τ_s).	79
Table 5.1: Nonbonded parameters for the interaction of PEO and PPO beads with each other, with polarizable water, and with lipid beads.....	98
Table 6.1: The Gromos 53A6 bonded interactions used in this study.	126

LIST OF FIGURES

	Page
Figure 2.1: Lateral pressure profiles from simulations in the NPT ensemble.....	24
Figure 2.2: Lateral pressure profiles from simulations in the NPzAT ensemble.	25
Figure 2.3: Lateral pressure profiles from simulations in the NPT ensemble.	26
Figure 2.4: Lateral pressure profiles from simulations in the NPzAT ensemble.	27
Figure 2.5: Bilayer structures obtained from some of the simulations performed in this study.	28
Figure 3.1: Representation of systems simulated in this work.	47
Figure 3.2: 2-Dimensional water density maps	48
Figure 3.3: 2-Dimensional water density maps	49
Figure 3.4: Time dependence of the pressure normal to the membrane surface	50
Figure 3.5: 2-Dimensional pressure maps at the membrane position	51
Figure 3.6: Snapshots of the bilayer membrane at various times of the simulations	52
Figure 3.7: Pressure profile at the membrane	53
Figure 3.8: 2-Dimensional pressure maps at the membrane position	54
Figure 3.9: Snapshots of the bilayer membrane at various times of the simulations	55
Figure 3.10: Pressure profiles at the membrane position.....	56
Figure 3.11: 2-dimensional pressure maps calculated at the membrane position.....	57
Figure 3.12: Bilayer membrane at various times of the simulation.....	58

Figure 3.13: 2-dimensional pressure maps calculated at the membrane position.....	59
Figure 3.14: Bilayer membrane at various times of the simulation.....	60
Figure 3.15: Pressure profiles at the membrane position.....	61
Figure 3.16: 2-dimensional pressure maps calculated at the membrane position.....	62
Figure 3.17: Bilayer membrane at various times of the simulation.....	63
Figure 3.18: 2-dimensional pressure maps calculated at the membrane position.....	64
Figure 3.19: Bilayer membrane at various times of the simulation.....	65
Figure 3.20: Pressure profile at the membrane position	66
Figure 3.21: 2-dimensional pressure maps calculated at the membrane position.....	67
Figure 3.22: Bilayer membrane at various times of the simulation.....	68
Figure 3.23: Water density and snapshots of membrane.	69
Figure 4.1: Initial configuration of the model TJ.....	80
Figure 4.2: Shock wave simulations with and without a nanobubble.....	81
Figure 4.3: RMSD curves for each of the claudin-15 proteins.	82
Figure 4.4: Number of contacts between interacting protein pairs.	83
Figure 4.5: Overall progress of the simulation during the 60 ps shock wave propagation	84
Figure 5.1: Time dependence of radius of gyration of P85 poloxamer molecule.....	99
Figure 5.2: Time dependence of radius of gyration of P188 poloxamer molecule.....	100
Figure 5.3: Snapshots of micelles of P85 (aggregation number = 60; left) and P188 (aggregation number = 21; right).....	101
Figure 5.4: Eccentricity of P188 (black) and P85 (red) micelles during 1 μ s simulation.	102

Figure 5.5: Various stages of insertion of Poloxamer P85 into the DMPC bilayer.....	103
Figure 5.6: Various stages of insertion of Poloxamer P188 into the DMPC bilayer.....	104
Figure 5.7: Density profiles	105
Figure 5.8: Interaction of P85 micelle with the DMPC bilayer.....	106
Figure 5.9: Interaction of P188 micelle with the DMPC bilayer.....	107
Figure 5.10: Snapshots of interaction of P188 micelle with the DMPC bilayer containing a pore.	108
Figure 6.1: Chemical structure of poloxamers.....	127
Figure 6.2: The radius of gyration of P85 in water.....	128
Figure 6.3: The radius of gyration of P188 in water.....	129
Figure 6.4: P85 molecules at the interface of air/water.	130
Figure 6.5: P188 molecule at the interface of air/water.....	131
Figure 6.6: Radius of gyration of PPO block of P85 molecules at air/water interface.	132
Figure 6.7: Radius of gyration of PPO block of the P188 molecule at the air/water interface.....	133
Figure 6.8: Interaction of P85 poloxamer with the DLPC model membrane.....	134
Figure 6.9: Interaction of P188 poloxamer with the DLPC model membrane.....	135
Figure 6.10: Self-assembly of P85 poloxamer, DLPC lipid monomers, and water molecules.	136
Figure 6.11: Interaction of five P85 poloxamers with a damaged DLPC model membrane.	137
Figure 6.12: Interaction of three P188 poloxamers with damaged DLPC model membrane.	138

LIST OF ABBREVIATIONS

AA	All atom
AMP	Antimicrobial peptide
BBB	Blood-brain barrier
bTBI	Blast-induced traumatic brain injury
CG	Coarse-grained
COM	Center of mass
DLPC	1,2-dilauroyl-sn-glycero-3-phosphocholine
DMPC	1,2-dimyristoyl-sn-glycero-3-phosphocholine
DOPC	1,2-dioleoyl-sn-glycero-3-hosphatidylcholine
DPPC	1,2-dipalmitoyl-sn-glycero-3-phosphocholine
FF	Force-field
GUV	Giant unilamellar vesicles
HLB	Hydrophilic–lipophilic balance
K	Kelvin
MD	Molecular dynamics
MDR	Multi-drug resistant
mTBI	Mild traumatic brain injury
nm	Nanometer(s)
NPT	Constant pressure simulation
NP _z AT	Constant area simulation

ns	Nanosecond(s)
PBC	Periodic boundary conditions
PDB	Protein data bank
PEO	Poly(ethylene oxide)
PME	Particle mesh Ewald
PPO	Poly(propylene oxide)
ps	Picosecond(s)
PtP	Peak-to-peak
Rg	Radius of gyration
RMSD	Root-mean-square deviation
SPC	Simple point charge
TJ	Tight junction
UA	United atom
μs	Microsecond(s)

Chapter 1: Introduction

1.1 Plasma membrane and its importance

The plasma membrane provides a barrier that separates the interior of the cell from the outside world. Interestingly, this barrier plays a variety of biochemical functions such as: compartmentalization, solute transport and permeability, responding to external signals and signal transduction, conversion of different energy types, and providing a scaffold for intercellular connections. The significance of these functions is highlighted when we realize that eukaryotic cells devote a large number of their genes to synthesize different lipids¹; one of the building blocks of the plasma membrane. Other major components of the plasma membrane are proteins and carbohydrates. Numerous lipid types in combination with varied proteins and carbohydrates at different ratios are responsible for the diversity of biological membranes in a cell (e.g. Golgi or endoplasmic reticulum) or an organism (e.g. eukaryotes or prokaryotes) or a specific tissue (e.g. heart or skin or kidney).

In general, membrane lipid molecules are amphipathic, meaning they have a hydrophilic head group which interacts with the solution on either side of the bilayer, and a hydrophobic tail where its packing with the neighboring lipid tails generates the core of the membrane. Phosphoglycerides, sphingolipids, and cholesterol are three major classes of lipids building biological membranes. The availability of numerous choices of molecules for the head group and the fatty acid moiety of the lipid is the key contributor to the diversity of biological membranes.

1.2 The plasma membrane and its therapeutic potentials

The fact that the plasma membrane is a barrier that keeps the integrity of the cell intact provides a huge potential for therapeutical purposes. Any exogenous compound that is used as a medicine in an organism will face the challenge of being transported to the cell interior or interacting with the signaling receptors residing in the membrane surface. In addition, permeability of the plasma membrane toward water and specific ions play a significant role in the electrochemical gradient across the membrane; a major application of this gradient is observed in neuronal cell signal transduction. Consequently, keeping the membrane healthy and intact is a crucial task and when a factor or trauma results in damage to the cell membrane and its permeability, a disease state is developed which needs medical intervention. There are a majority of traumas that are potentially harmful to the integrity of the membrane such as heat or electric shock.

Keeping the plasma membrane healthy and intact is not always favorable from a therapeutic point of view; it depends on the context and the organism in question. A significant part of medicine deals with preventing opportunistic and pathological organisms, including bacteria, viruses, and fungi from growing and reproduction in the host. Since these opportunistic microorganisms are encapsulated in a plasma membrane, one of the approaches for antibiotic intervention is to interfere with the permeability of the invading microorganism's plasma membrane or its cell membrane synthesis machinery. Daptomycin, as an example, is a lipopeptide antibiotic which targets bacterial cell membrane specifically. Following insertion into the bacterial membrane, it aggregates with other daptomycin molecules and generates holes in the membrane. The leakage from the bacterial cell through these holes results in depolarization of the cell and bacterial cell death². Posaconazole, a broad-spectrum triazole

antifungal drug, works by depleting the ergosterol, resulting in a less stable cell membrane which eventually interferes with all activities of the membrane including transfer of nutrients and chitin synthesis³.

From another perspective, since the plasma membrane is the first barrier in front of any exogenous material, breaking open this barrier in a controlled and reversible manner would be potentially useful for drug and macromolecule delivery to the intercellular space. One promising approach to fulfill this has been the application of shock waves⁴⁻⁸. Needless to say, when the shock wave is produced uncontrollably, similar to the ones that appear during an explosive blast, depending on the case they could be detrimental or pathogenic. More specifically, exposure of neural cells to uncontrolled shock waves, in the human brain, can predispose the individual to blast-induced traumatic brain injury (bTBI)⁹.

1.3 Tools and techniques used for plasma membrane research

A variety of techniques and methods have been used to study the properties of plasma membrane. The experimental techniques used include a large number of methods, to name a few: X-ray and neutron scattering¹⁰, AFM¹¹, Fluorescence probing¹², NMR¹³, etc. In addition to numerous experimental techniques, computer simulations can also provide a very detailed and molecular picture of the dynamic and structure of the model membranes. Molecular dynamics simulations of bilayers can not only independently provide quantitative measures of membrane properties^{14,15}, they can also help interpret experimental data^{16,17}. Nevertheless, it is common practice to evaluate the computational measures and make sure the calculated values are in agreement with the experimental ones. This is of absolute importance since a single force field

that reproduces every aspect of membrane or protein biology is not available and computational experiments always are meaningful within considering certain assumptions.

1.4 Molecular dynamics computer simulation technique

Molecular dynamics is a computer simulation technique in which movement and position of atoms is predicted by numerically solving Newton's equations of motion resulting in trajectories of the particles which represent the way the particles evolve over time. Calculating averages over these trajectories enables us to connect the microscopic representation of the system with the macroscopic experimental measurable quantities.

At the heart of the technique, there is the notion of a force-field (FF), which is defined as a set of parameters to calculate potential energy between interacting particles. It is the force-field that determines the accuracy of the prediction of the particle position at any step; accordingly, to have a reliable prediction and accurate trajectory one requires a carefully defined and evaluated force-field. In other words, the force-field that reproduces the experimentally measured quantities more accurately is a better parameter set.

Force-fields come in with employing different representations of particles. When every atom type in the system is represented as an explicit and separate particle it is called "all-atom" (AA), whereas merging hydrogen with carbon and making individual single particles such as CH, CH₂, or CH₃ types results in "united-atom" (UA) force field. The merging of the hydrogens with the carbons reduces the computational cost of the calculations. In order to reduce the calculation time even more and reach larger size and time scales, sometimes another representation is employed which is called "coarse-grained" (CG). In this type of force fields usually larger atoms or the so-called super atoms are defined which consist of 3 or more particles

merged together, making the representation even more crude. However, the gain is an increase in the speed and the size of the system to be simulated. The factor that determines the choice of the force-field is the research goals and the type of the questions in the study. As an example, if the researcher is interested in studying the interaction of a small molecule or drug with the active site of an enzyme, it makes more sense to use an all-atom representation of the system since understanding the atom-atom interactions are the key. On the other hand, when the research interest is about the bulk properties of a patch of membrane and how they change under different conditions, it is more reasonable to simulate a larger system represented in a coarse-grained force-field, since each individual interaction is not that informative. Among the available force-fields for simulating biological systems, CHARMM¹⁸ (AA), AMBER¹⁹ (AA), OPLS²⁰ (AA), GROMOS²¹ (UA), and MARTINI²² (CG) are more reliable, carefully tested, and more commonly used.

1.5 The research goals and approaches taken in this study

The overall purpose of this dissertation was to utilize molecular dynamics computer simulations technique to study different approaches to the plasma membrane. Our force-field of choice was MARTINI²² (CG) model were the coarse-grained nature of the atomic resolution allowed us to simulate large size patches of membrane and achieve longer time scales. When more detailed output was required, we used GROMOS 53A6²³ (UA).

We followed two general themes: first, what mechanisms are involved in opening of the plasma membrane? In other words, how the barrier of the cell can be opened? Second, what mechanisms membrane sealants employ to bring back the integrity of a damaged membrane to the normal state? As mentioned earlier, the first route, depending on the context, can have either

favorable or pathogenic interpretations; when the purpose of the study is to develop an understanding on how specific molecules attack bacterial membrane selectively and make it leaky, it has favorable pharmaceutical applications (e.g. antibiotic production). However, if we are interested to understand how neural cell membranes react to uncontrolled shock waves impact and how this membrane and cell damage can cause brain injury, it can provide explanation on the pathogenicity of the blast exposure. Interestingly, the same shock wave, when used under control can be utilized in delivery of molecules to the cell, which is therapeutically applicable. In addition, the second route provides molecular pictures on how trauma to the membrane is sealed and its significance in pharmaceutical research and treatment procedures is therefore helpful.

1.6 What mechanisms are involved in opening of the plasma membrane?

1.6.1 Antimicrobial peptides (AMPs)

In Chapter two, we studied two antimicrobial peptides melittin and magainin and how their absorption to the surface of a model lipid bilayer changes the local pressure. Antimicrobial peptides are the first line of defense against bacterial invasion before a more sophisticated host response is involved. Their specificity toward bacteria highlights their role as potential candidate for antibiotic development. The main goal in our research was to shed light on how these peptides disrupt the permeability of the bacterial membrane. The hypothesis comes from experimental observations where melittin seems to generate transient pores²⁴, while magainin initially absorbs to the membrane surface and starts to build a tension in the membrane. Once the tension exceeds a threshold level, as a response, the membrane ruptures, to release the tension and reach equilibrium state²⁵. Since measuring the local tension in each individual leaflet is a

task that is experimentally impossible to do, evaluating this hypothesis on empirical bases was not feasible. However, we employed molecular dynamics computer simulations where the local pressure profile in the membrane, within any arbitrary interval along the normal axis (z) to the membrane surface can be measured. In addition, to better emulate the initial non-equilibrium state of the interaction of the peptides with the membrane, before pore formation or membrane rupture, we tested two ensembles, NPT (constant pressure, temperature, and number of particles) versus NP_zAT (constant normal pressure, area, temperature, and number of particles), to test which one captures the state of the initial absorption better.

1.6.2 Shock wave induced nano-bubble collapse and its impact on the plasma membrane

Chapter three looks at the molecular mechanisms behind membrane damage under the impact of a shock wave. There are numerous studies in the literature highlighting the importance of collapse of bubbles close to biological membranes, upon the impact of a shock wave^{26–31}. Despite these findings, the underlying mechanism by which the collapse of a bubble results in membrane poration is not clear. In other words, when a shock wave hits a membrane with certain velocity, it may not generate pore in the membrane. However, the same shock wave, if it first impacts a bubble (cavitation, whether nano or micro scale) located in close distance to a membrane, the resulting collapse of the bubble generates significant damage to the membrane. Our goal was to understand how the cavitation changes the shock wave impact. We investigated this phenomenon utilizing molecular dynamics computer simulations and measured the pressure distribution at the membrane surface at different states of the shock simulation, in the presence and absence of a nano-scale bubble. Our calculated 2-dimensional pressure distribution profiles, that are impossible to measure experimentally, provided an explanation of the importance of cavitation in shock wave induced membrane damage.

Building on our better understanding of the role of cavitation in shock wave induced membrane damage, we applied molecular dynamics simulations to model how shock wave induced nano-bubble collapse can damage blood-brain barrier (BBB). We describe this part of the work in Chapter four. The idea comes from the pathophysiology of blast-induced traumatic brain injury (bTBI) where exposure to blast shock waves results in BBB openings and consequently leakage of compounds from the blood to the brain tissue. The accumulation of these unwanted compounds in the brain will result in neuro-inflammation and other complications that veterans and military personnel who served in active war zones suffer from³². From another point of view, the same principle can be used in a controlled way to reversibly and temporarily open the BBB to achieve delivery of chemotherapeutical agents to brain tumors; a route which is closed under normal conditions^{33,34}. Interestingly, administration of micro-bubbles into the blood stream, prior to the local shock wave exposure, reduces the energy of the ultra sound required to open the BBB³⁵. Since we already observed how cavitation enhances the damaging effect of the shock wave (Chapter three), we investigated the role of cavitation in the vicinity of a model tight junction (TJ). Our TJ represents a very simple imitation of the connecting blocks of endothelial cells in brain capillaries. Our computer simulations provided evidence on significance of cavitation in the pathophysiology of blast-induced TBI and shock wave exposure.

1.7 What mechanisms membrane sealants employ to restore the integrity of a damaged membrane?

In Chapter five we studied the molecular mechanisms by which membrane sealants restore the damage that is already made in a plasma membrane by a variety of traumatic events. Poloxamers or triblock copolymers are a group of polymers whose main application is in

industry as surfactants. They also have applications in drug delivery and membrane healing^{36–40}. We focused on two prototypical polymers P85 and P188. The former is a hydrophobic polymer with tendency to cross the membrane (drug delivery applications³⁷) and induce conformational changes in membrane proteins⁴¹, while the latter is a more hydrophilic polymer with therapeutical applications in burned patients⁴².

To study how these polymers interact with membranes, we focused on both individual and micelle interaction of triblock copolymers with bilayers. To reduce the cost of calculations and achieve a larger time scale, we developed a set of coarse-grained (CG) parameters for simulating these polymers both in solution and in close proximity of a patch of lipid bilayer. The importance of our simulation was employing polarizable water model in the coarse-grained resolution since polarization of water will capture the interaction of polar groups in Poloxamers with polar or charged groups in the lipids in a more realistic way. In addition, we investigated the interaction of a micelle of P188 Poloxamer close to a damaged model membrane. Our study is the first attempt in providing molecular pictures of membrane healing by P188 micelles in the literature.

Chapter six approached the problem from another resolution; we developed a more detailed united-atom (UA) force field set of parameters to perform molecular dynamics simulation of Poloxamers. This approach provided a better understanding of the way these polymers interact with model intact or damaged membranes. Additionally, there are reports in the literature that show P85 has inhibitory effects on *p*-glycoproteins and as a result it interferes with multi-drug resistance (MDR) in the cells⁴¹. To model these interactions, more specifically, to model the interaction of P85 with membrane proteins, it is much more favorable to have a detailed force-field representation of the system under study. Coarse-grained representation of

proteins will lose most of the side chain resolution of amino-acids and specific interactions will be lost. A higher resolution force-field on the other hand will preserve the interacting particles and provides a better and clearer picture of the way P85 interacts with proteins. Our goal of the study was to provide such a force field.

To achieve this we started by a modified united-atom force field (GROMOS 53A6_OE⁴³) where the van der Waals parameters for an ether oxygen was already available and we fine-tuned the charges to reproduce the experimental radii of gyration of P85 and P188. Additionally, we studied how the individual polymers interact with model damaged membranes. The results obtained by detailed force field were very similar to the coarse-grained one which adds more credibility to our approach and parameter development methodology.

Chapter 2: Local Pressure Changes in Lipid Bilayers Due to Adsorption of Melittin and Magainin-h2 Antimicrobial Peptides: Results from Computer Simulations¹

2.1 Introduction

Antimicrobial peptides (AMPs) often represent the first line of defense against invading bacteria; they work by damaging the invaders membrane. In spite of a large amount of work to understand the molecular mechanism of AMP action, the details still remain unclear⁴⁴. Different scenarios were proposed to explain damage to membranes, including creation of pores of different architecture, like barrel-stave or toroidal, or rupture of membranes by peptides that act as surfactants (so-called carpet model)⁴⁵⁻⁴⁷. Experiments indicate that, once adsorbed on the bilayer surface, different AMPs act in different ways. For example, it is suggested that melittin permeates the membrane and creates transient pores²⁴. As a result of such permeation the number of peptides increases on the other leaflet of the membrane bilayer, until an equal amount of peptides is located on surfaces of both leaflets: after that a permanent toroidal shape pore is created with its walls containing melittin and lipid headgroups²⁴. A different scenario of action is proposed for another AMP, magainin. In this case it is proposed that peptides do not permeate the membrane; instead they create a pore due to tension that exists in the membrane because of the peptides presence on the membrane surface²⁵. These two distinct mechanisms of pore creation in the membrane are consistent with two different patterns of dye leakage from the giant

¹ This chapter previously appeared as an article in the Journal of Physical Chemistry B. The original citation is as follows: Goliaei A, Santo K P, and Berkowitz M L, "Local Pressure Changes in Lipid Bilayers Due to Adsorption of Melittin and Magainin-h2 Antimicrobial Peptides: Results from Computer Simulations," *Journal of Physical Chemistry B* 44, no. 118 (November 2014): 12673.

unilamellar phospholipid vesicles (GUV) exposed to solution of AMPs. When AMP in the experiment is melittin, the dye leakage from the vesicle is graded (gradual),⁴⁸ due to transient pores in GUV and also, perhaps, presence of rather small permanent pores. When AMP is magainin, some of the vesicles open pores under tension and some do not, while magainin does not permeate the membrane and stays on the membrane surface^{25,49}. The dye leaks only from the vesicles with open pores, while no leakage occurs from the vesicles that are intact. Therefore, the mechanism of dye leakage in this case is called all-or-none. While the two mechanisms look different, it is proposed that a common feature for both of them is that peptides exert tension in each case and membrane ruptures, although to a different degree, in order to release this tension.

In addition to a large amount of experimental work that studied the interaction between membranes and AMPs, computer simulations were also performed that can provide detailed molecular information about the interaction between peptides and lipid membranes^{50–63}. To imitate the experimental situation AMPs were often placed on the surface of the bilayer, and the development of the system was followed. Most of the simulations containing lipid membrane and AMPs were performed using constant pressure, constant temperature (NPT) ensemble. In these simulations the pressure was chosen to be equal in all three directions, which is equivalent to setting the value of the total stress experienced by the membrane to zero. Indeed, the stress on the membrane is given by the equation

$$\sigma = - \int_{z_1}^{z_2} [P_L(z) - P_N(z)] dz = - \int_{z_1}^{z_2} P(z) dz \quad (2.1)$$

where $P_L(z) = (P_{xx} + P_{yy})/2$ is the local lateral pressure depending on the z -coordinate which is normal to the membrane surface, $P_N(z)$ is the local normal pressure, which is a constant along the z -direction (z_1 and z_2 are positions on a line along the normal to membrane surface z axis; these

positions are taken to be outside the bilayer where the values of the integrand $P(z)$ are zero). $P(z)$, the difference between lateral and normal pressure, is also often called the lateral pressure, since the shape and values of the $P(z)$ profile are mostly determined by $P_L(z)$. Thus, eq 2.1 predicts that by using an NPT ensemble with equal pressure in all three directions the value of stress equal to zero is obtained for the bilayer. That the total stress on the membrane bilayer is equal to zero in the NPT simulations of systems containing asymmetric distribution of AMPs on the bilayer leaflets does not mean that the stress acting on each leaflet is also zero. Indeed, one can consider the bilayer as two monolayers and, therefore, represent the integral for stress from eq 2.1 as sum of two integrals

$$\sigma = - \int_{z_1}^{z_0} P(z) dz - \int_{z_0}^{z_2} P(z) dz \quad (2.2)$$

where z_0 is the z coordinate of the normal to bilayer line that divides the bilayer into two monolayers. In eq 2.2 every integral represents the stress on the corresponding monolayer.

If all peptides are initially placed on one of the leaflets, and the simulation is performed using the NPT ensemble with equal pressure in all three directions, the total stress on the membrane will be zero, as mentioned above. Nevertheless, the stress on each monolayer will not be equal to zero, due to the imposed asymmetry in the system. It is the existence of this nonzero stress in each monolayer when peptides are adsorbed on the membrane surface that is responsible for the initiation of a pore. Since the total stress in the bilayer is zero, the absolute value of the stress acting on each monolayer will be the same, but stresses on each of the monolayers will have opposite signs. As a result, each monolayer will experience a force due to stress, but the forces will act in opposite directions, producing a pair of forces that may facilitate membrane rupture and also bending. If the initial total stress is not equal to zero when peptides get adsorbed

on the membrane surface, the values of the stress acting on each monolayer are different. In this case the simulations should be performed using a different ensemble, for example constant normal pressure, constant area, and constant temperature (NP_zAT) ensemble when the area is known. Using the latter ensemble, the simulation usually produces a nonzero stress in the bilayer.

In this paper we report the results from simulations performed to study how the local pressure profiles change with the change in the total stress acting on the membrane. Therefore, we perform simulations in both NPT and NP_zAT ensembles, since they produce different total stress in the membrane. Our simulations are done on systems with bilayers containing 1,2-dioleoyl-*sn*-glycero-3-phosphatidylcholine (DOPC) lipids and AMPs, either melittin or magainin, adsorbed on one of the monolayers. We chose the lipid to be DOPC, since experimental data are available to us for the systems containing DOPC and melittin peptides at different P/L ratios⁶⁴. We also want to understand how the difference in stress produced by melittin or magainin can produce a difference in their mode of antimicrobial action. Since the activity of the AMPs depends on their peptide to lipids ratio (P/L), we performed our simulations at different P/L . We use a coarse-grained force field MARTINI⁶⁵ in our simulations, since by using this force field we can run our simulations for longer time to accumulate more data and produce smoother pressure profiles.

2.2 Methods

We employed the coarse-grained MARTINI force field with the improved parameters⁶⁵ and polarizable water⁶⁶ in our simulations. The lipid membrane used in the study is DOPC. All of our simulations were performed using GROMACS⁶⁷ software package version 4.5.5. A patch

of 600 lipid molecules was generated using the “insane.py” script provided by the MARTINI Web site (<http://md.chem.rug.nl/cgmartini/images/tools/insane/insane.py>). Na⁺ and Cl⁻ ions were added to maintain an ion concentration of 0.1 M. The generated membrane was energy minimized and equilibrated for 2 μ s using the NPT ensemble. Temperature at 303 K and pressure at 1.0 bar (semi-isotropic coupling) were maintained using the Berendsen coupling scheme⁶⁸ with time constant of 2 ps. Compressibility value was 3×10^{-4} bar⁻¹ for pressure coupling. The cutoff for the Lennard-Jones interactions was set to 1.2 nm, and the reaction-field scheme⁶⁹ was used for the electrostatics with a cutoff of 1.2 nm and a dielectric constant of 2.5. The time step for integration was 20 fs.

The peptides in this study are melittin and magainin-h2. Melittin has the following sequence: GIGAVLKVLTTGLPALISWIKRKRQQ. The initial structure of melittin was obtained from the available crystal structure^{70,71}. Total charge of +6 was considered, which originates from the following residues: protonated Glycine1 (at physiological condition⁷²), Lysine7, Lysine 21, Arginine 22, Lysine 23, and Arginine 24. The sequence of the second peptide, magainin-h2 is IIKKFLHSIWKFGKAFVGEIMNI. This peptide is an analogue of the magainin-2 which is widely studied experimentally⁷³. Magainin-h2 has a net charge of +3 due to Lysine 3, Lysine 4, and Lysine 11 residues. Initial structure for magainin-h2 was generated by mutating the corresponding residues in the NMR structure of magainin-2⁷⁴ using the Pymol software⁷⁵. In any simulation containing melittin or magainin-h2 a corresponding number of Cl⁻ ions were added to keep the systems neutral. We performed simulations on eight systems containing lipid bilayers and AMPs; in all of our systems peptides were located on just one side of the bilayer. In four of our systems the peptide was melittin, and in the other four it was magainin-h2. Two simulated systems contained 12 peptides and two other systems contained 18,

so our simulations were performed at P/L of 1/50 and 3/100. Each system was simulated in both NPT and NP_zAT ensemble. Initially, in every simulation our peptide molecules were randomly inserted into the bilayer (containing 600 lipid molecules) with peptide helices oriented parallel to membrane surface and located just below the phosphate headgroup regions. The assembled system was energy minimized and equilibrated for 2 μ s.

For the simulations with peptides, performed in the NP_zAT ensemble, we needed to know values of the area, A . Initially we found the area per lipid for pure DOPC bilayer by performing simulations in the NPT ensemble on this system (area per lipid: 67.8 \AA^2). In order to find the area change when melittin peptides were added, we used the available experimental data that showed the change in the hydrophobic length of the membrane with the addition of melittin peptides at different P/L ratios⁶⁴. To find the change in the area, we followed the same argument as used in the experimental analysis. Assuming that the volume of the hydrocarbon region of a membrane does not change upon insertion of a peptide, the value of the final area (in the presence of peptides) relative to the initial area (peptide free membrane) can be obtained from the following formula:

$$V_{initial} = V_{final}, \quad (2.3)$$

or

$$A_{initial} \times Z_{initial} = A_{final} \times Z_{final}, \quad (2.4)$$

where A is the area and Z is the peak-to-peak distance (PtP) measured experimentally from the electron density profiles. Accordingly we have

$$A_{final} = A_{initial} \times \left(\frac{Z_{initial}}{Z_{final}} \right). \quad (2.5)$$

The ratio of $Z_{initial}/Z_{final}$ was obtained from the experimental data⁶⁴ and for the $A_{initial}$ the average value of the area of the DOPC simulation after 2 μ s equilibration was selected (67.8 \AA^2). After calculating the A_{final} , box-X and box-Y values of the protein containing simulations were changed to reach the calculated value, using eq 2.5, for the final area (area per lipid: 71 \AA^2). Since the experimental data for bilayers containing magainin-h2 peptide are not available to us, we assumed that the areas of the bilayers with melittin and magainin-h2 are the same. This allows us to concentrate on the effect produced only by the difference in the composition of the peptides. Experiments show that, for melittin, when the P/L ratio reaches the value of 1/50, the area stops changing with the increase of the P/L ⁶⁴. Therefore, the NP_zAT simulations with $P/L = 3/100$ for melittin were done at the same value for area as when P/L was 1/50. Moreover, since we assumed that areas in NP_zAT simulations with melittin and magainin-h2 were the same, it follows that all our simulations with AMPs in the NP_zAT ensemble were performed at the same value of the area.

Calculations of the pressure profiles in this work were done using the new method developed recently⁷⁶ which relies on a previous local pressure code implementation⁷⁷. The new code correctly provides a constant value of P_{zz} for both coarse grained and atomistic simulations. Prior to pressure calculations each system was equilibrated for 5 μ s followed by the data collection. To estimate the error in stress values we divided the trajectories into four separate pieces of length 300 ns each, during which position and velocities were saved every 5 ps. These generated trajectories were then rerun for calculation of the pressure tensor using the same parameters as used in the equilibration runs. The thickness of slabs for the local pressure

calculations was set to 1 Å. Visualization of the resultant trajectories was performed using the VMD⁷⁸ software. We did not observe any spontaneous pore creation in our simulations.

2.3 Results and Discussion

To study the difference between results obtained from simulations on systems containing AMPs adsorbed on membrane surfaces by using the NPT ensemble with equal pressure in all three directions and simulations where the NP_zAT ensemble was used, we studied systems containing melittin and magainin-h2 peptides adsorbed on the outer surface of the DOPC membrane at different *P/L* ratios. We started our simulations by placing peptides in the phosphate headgroup region of the membrane. This was done because when peptides were placed into the solution on top of the bilayer, they tended to aggregate into a big globular structure, which did not interact with the membrane. Accordingly, our simulations capture the sequence of events following the adsorption of peptides on the bilayer surface. We observed that, during the simulations, several peptides sometimes combined into small aggregates for short periods of time, but most of the time peptides were distributed throughout the whole bilayer area without aggregation.

2.3.1 Membranes Containing 12 AMPs (*P/L* = 1/50)

Four simulations were performed for systems containing 12 peptides: 2 contained melittin and 2 magainin-h2. Figure 2.1 shows the lateral pressure profile obtained from simulations using the NPT ensemble. For comparison we also present a pressure profile for pure membrane, which was obtained using the NPT ensemble. Addition of AMPs to pure bilayer changes the pressure profile: it becomes asymmetric; a hump appears in the region where tails of the lipids in the upper leaflet (the leaflet with adsorbed peptides) are located, corresponding to

stronger repulsion between these tails. This is happening because the AMPs compress the lipids in this leaflet. The local pressure in the tail region of the opposing leaflet is reduced, since the leaflet slightly expands. The negative dips located in the regions of water/headgroup interface of the monolayers are also slightly reduced, indicating a reduction in the hydrophobic tension. It is interesting that the dip is reduced stronger by magainin-h2, indicating that it acts as a better surfactant. We calculated that the total stress on the upper layer due to the presence of melittin is -6.4 ± 0.2 mN/m, while it is 6.9 ± 0.8 mN/m for the lower. These are equal (within an error bar) in their absolute value, as expected. For magainin-h2 the values are -7.7 ± 0.6 mN/m and 7.7 ± 0.3 mN/m for upper and lower layers, respectively. As we can see, the stresses in the monolayers caused by melittin and magainin-h2 are quite similar if the ensemble used is NPT, although magainin-h2 produces a somewhat larger stress. Finally, for comparison, the average area per lipid in the systems with peptides simulated in the NPT ensemble was 72.1 \AA^2 for simulations with melittin and 72.8 \AA^2 with magainin-h2.

Figure 2.2, which looks quite similar to Figure 2.1, shows the pressure profiles obtained from simulations with 12 AMPs, but now performed using the NP_zAT ensemble. The 12 melittin peptides produce a stress of -4.0 ± 0.6 mN/m on the upper monolayer, while it is 7.8 ± 0.6 mN/m on lower. In this case the stresses are not equal in their absolute value, and there is a total stress acting on the membrane which is equal to ~ 4 mN/m. For magainin-h2 the stresses are -7.0 ± 0.5 mN/m and 7.2 ± 0.9 mN/m on upper and lower monolayers, respectively. Interestingly, there is no net stress produced by magainin-h2, but each monolayer experiences a stress.

2.3.2 Membranes Containing 18 AMPs ($P/L = 3/100$)

Four simulations were also performed on systems containing 18 peptides. Figure 2.3 shows pressure profiles from simulations performed using the NPT ensemble. The shapes of the curves are similar to the shapes from Figure 2.1, although the deviations from the curve for the free bilayer are much larger in Figure 2.3. Particularly large deviations are observed in the region of the negative dip, especially in case of magainin-h2. The values of the stress in these simulations are -8.8 ± 0.3 mN/m for upper monolayer and 9.4 ± 0.3 mN/m for the lower bilayer in the case of melittin. For magainin-h2 the corresponding numbers are -10.4 ± 0.7 mN/m for upper monolayer and 11.1 ± 0.4 mN/m for lower monolayer. The absolute value of the stress on each monolayer increased relative to the value of the stress experienced by monolayers, when the ratio was 1/50. Also, the stress due to magainin-h2 was $\sim 10\%$ larger than the stress due to melittin. Average areas per lipid obtained for the systems with peptides simulated in the NPT ensemble were the following: with melittins, 73.6 \AA^2 , and with magainin-h2, 75 \AA^2 .

Figure 2.4 shows pressure profiles when 18 AMPs are situated on the bilayer surface and simulated using NP_zAT ensemble. This time the difference between the curves depicted on this figure and the curves from all other figures is quite substantial. The main change comes from the regions of negative dips, which are strongly diminished, indicating a much lesser contribution of hydrophobic surface tension to stress, pointing out that AMPs are good surfactants. Especially, a large reduction in a negative dip is observed for magainin-h2. Interestingly, the effect of peptides on pressure distribution is not limited to one monolayer on which the peptides are adsorbed; it propagates to the opposing monolayer. The effect is somewhat weak for the case of 12 peptides, stronger when 18 peptides are simulated in the NPT ensemble, and very strong when 18 peptides are simulated in the NP_zAT ensemble. The total stress for the case with melittin is now $-10.4 \pm$

1.4 mN/m for upper leaflet and 8.4 ± 0.3 mN/m for lower leaflet. For the case with magainin-h2 the results for stress are -14.8 ± 0.6 mN/m for upper leaflet and 8.5 ± 0.5 mN/m for the lower leaflet. As we can see, the stress induced by magainin-h2 on the leaflet of the bilayer on which the peptides are adsorbed is much stronger than the stress due to action of melittin. The absolute values of the total stress induced by melittin and magainin-h2 are also different: it is ~ 2 mN/m in case of melittin and 3 times larger value (~ 6 mN/m) for magainin-h2.

2.4 Conclusions

There are two issues we attempt to understand by performing simulations described here. The experimental papers dealing with the AMPs action often refer to the importance of stress caused by the presence of peptides in the system. Therefore, the first issue we consider is related to the somewhat paradoxical situation, that when NPT simulations with equal pressure in three directions are performed, the total stress experienced by the bilayer is zero, even in the presence of AMPs adsorbed on the bilayer surface. The second issue is related to the difference in action of AMPs such as melittin and magainin-h2, and its connection to the difference in stress profiles produced by these AMPs.

Our simulations of the bilayers containing AMPs such as melittin and magainin-h2 confirmed, as expected, that the total stress on the lipid bilayer is zero, when NPT simulations with equal pressure in all three directions are performed. Since most of the simulations of bilayers containing AMPs are done in the NPT ensemble, the total stress on the bilayer in those simulations was zero. Nevertheless, there are still stresses acting on each bilayer leaflet. These stresses are acting in opposite directions and are equal in their absolute values. To remove these stresses pores may be created in membranes, and also because there is a pair of forces acting in

opposite directions on upper and lower leaflets, membranes may bend. In our simulations we observed that the values of the stresses on monolayers we obtained from the NPT simulations of bilayers with melittin and magainin-h2 are similar; this makes it difficult to explain the difference in the mode of magainin versus melittin action as due to difference in stress.

Free lipid bilayers in equilibrium experience no stress. When AMPs are adsorbed on the surface of one of the leaflets, the system may find itself initially in a nonequilibrium state with a total stress not equal to zero. To remove the stress the bilayer will rearrange through creating pores and bending, thus moving to a new equilibrium state with the total stress again equal to zero. The NP_zAT simulations are better in mimicking the initial stage when the total stress is nonzero. In these simulations the stresses on each monolayer, although still different in the sign, are not equal in their absolute values. The action of a pair of forces acting in different directions and of unequal value should result in a creation of a bilayer with a larger curvature. Figure 2.5 shows the shape of the bilayers with the 18 AMPs adsorbed on the upper leaflet when simulations were done in NP_zAT ensemble. For comparison, the shape of the pure bilayer obtained from the NPT simulation is also shown. While there is little curving present in the simulation of pure lipid bilayer, the curving of the bilayers with AMP is clearly seen. Nevertheless, some words of caution are required to be said here: the geometry of our simulations that are performed using periodic boundary conditions may suppress the curving tendency, or produce a wrong curvature.

When AMPs are adsorbed on the bilayer surface they induce stress. To remove this stress the AMPs may either permeate the membrane and initially create transient pores, or just create pores due to large stress on a membrane. Experiments indicate that melittin chooses the first route, while magainin the second. Our simulations on systems with a total stress experienced by

the bilayer (i.e., simulations performed in NP_zAT ensemble) show that magainin-h2 at larger P/L produces a larger stress on the bilayer compared to stress produced by melittin. This observation is consistent with the suggestions about the mechanism of magainin antimicrobial activity made by Tamba et al. based on their experimental work²⁵.

Since our simulations were performed at the same value of area and since both peptides are α helical and are almost of the same length, the major difference between our systems with peptides is in the peptide sequence. Different peptide side chains (amino acids) in these two peptides interact in a different way with the membrane producing the difference in modes of AMPs action. Still, in general, further experimental and computational research on the detailed nature of AMP activity is required to shed more light on this complicated but important problem.

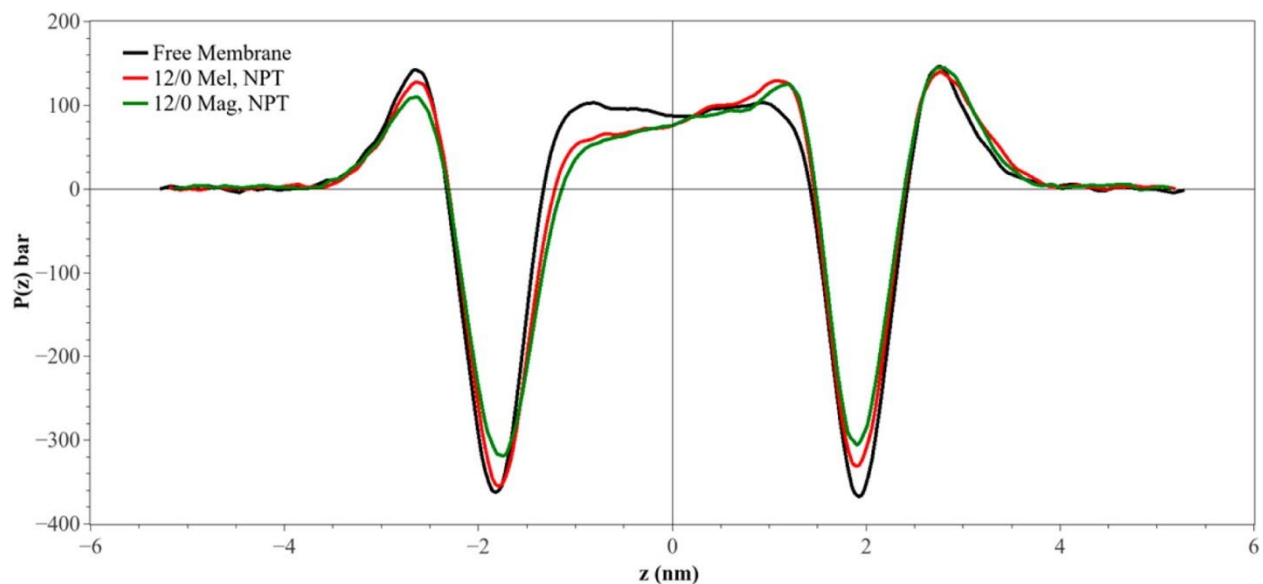


Figure 2.1: Lateral pressure profiles from simulations in the NPT ensemble. Red and green curves depict the pressure profiles obtained from the simulation when 12 peptides were inserted into the top leaflet and no peptides placed into the lower leaflet. Red curve is when peptide is melittin and green curve when it is magainin-h2. For comparison we also present the pressure profile in the peptide free membrane, obtained from the simulation in the NPT ensemble (black curve).

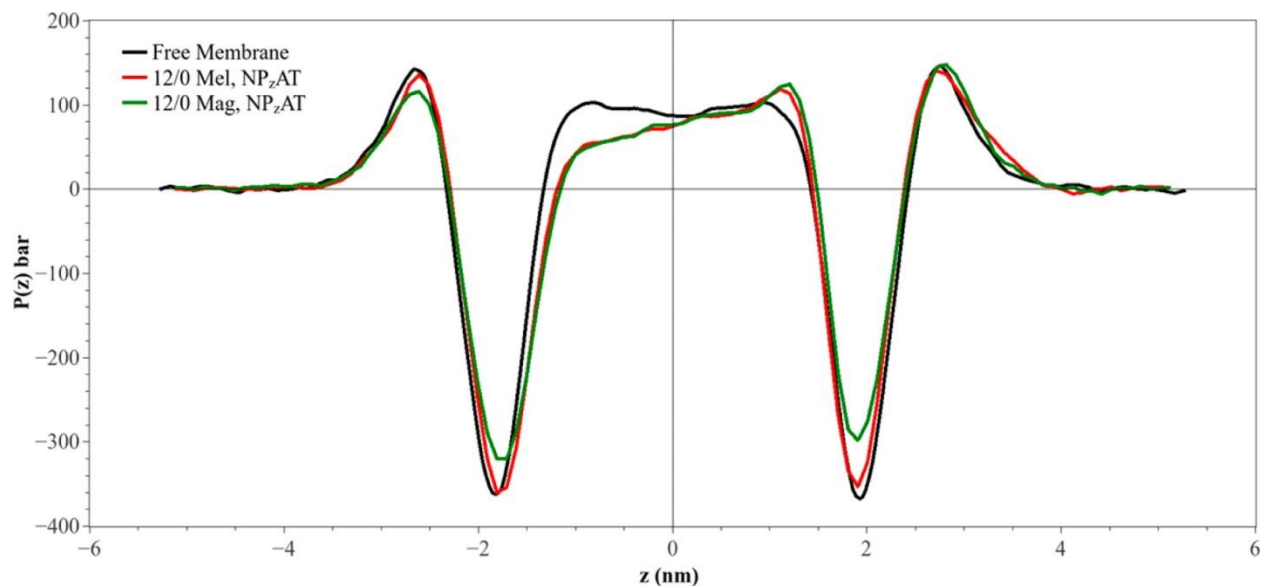


Figure 2.2: Lateral pressure profiles from simulations in the NPzAT ensemble. Red and green curves depict the pressure profiles obtained from the simulation when 12 peptides were inserted into the top leaflet and no peptides placed into the lower leaflet. Red curve is when peptide is melittin and green curve when it is magainin-h2. For comparison we also present the pressure profile in the peptide free membrane, obtained from the simulation in the NPT ensemble (black curve).

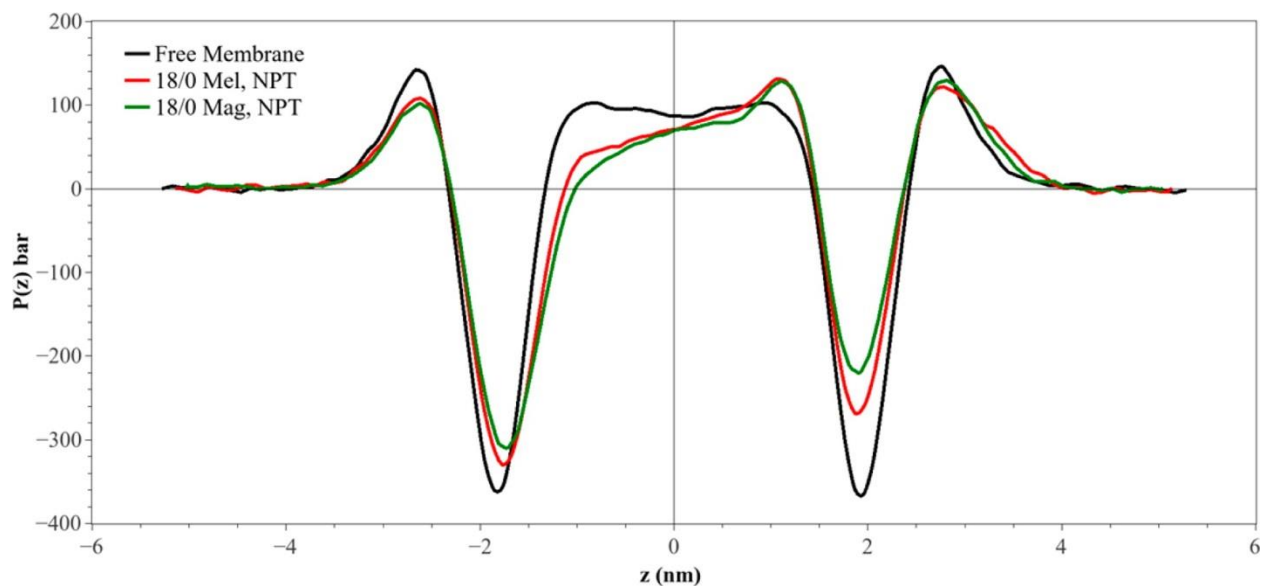


Figure 2.3: Lateral pressure profiles from simulations in the NPT ensemble. Red and green curves depict the pressure profiles obtained from the simulation when 18 peptides were inserted into the top leaflet and no peptides placed into the lower leaflet. Red curve is when peptide is melittin and green curve when it is magainin-h2. For comparison we also present the pressure profile in the peptide free membrane, obtained from the simulation in the NPT ensemble (black curve).

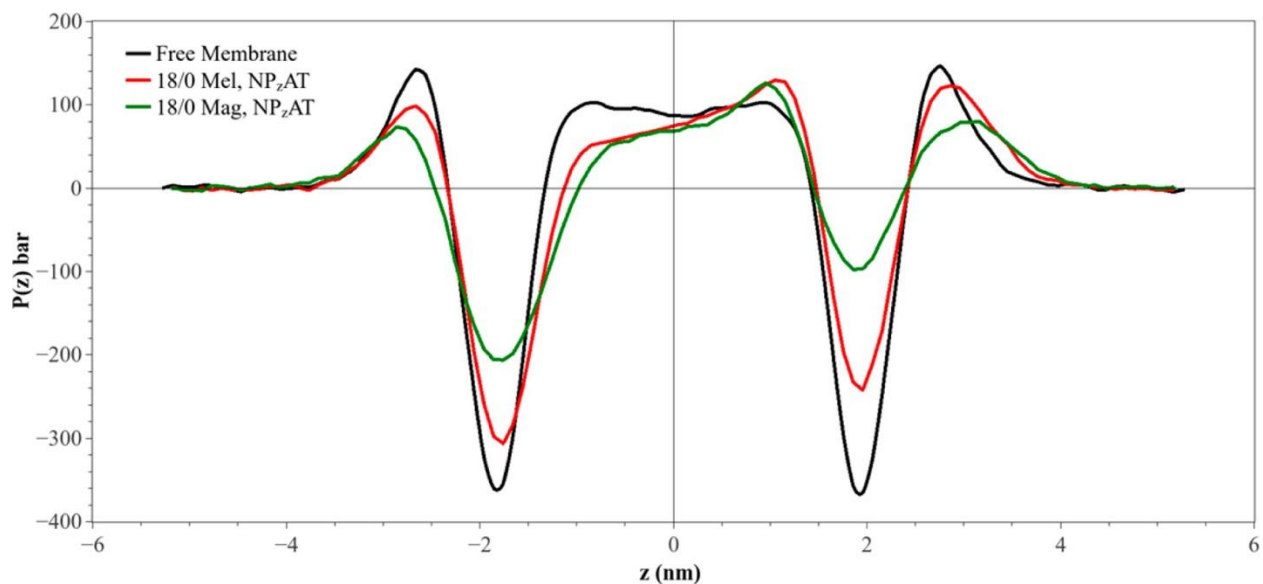


Figure 2.4: Lateral pressure profiles from simulations in the NPzAT ensemble. Red and green curves depict the pressure profiles obtained from the simulation when 18 peptides were inserted into the top leaflet and no peptides placed into the lower leaflet. Red curve is when peptide is melittin and green curve when it is magainin-h2. For comparison we also present the pressure profile in the peptide free membrane, obtained from the simulation in the NPT ensemble (black curve).

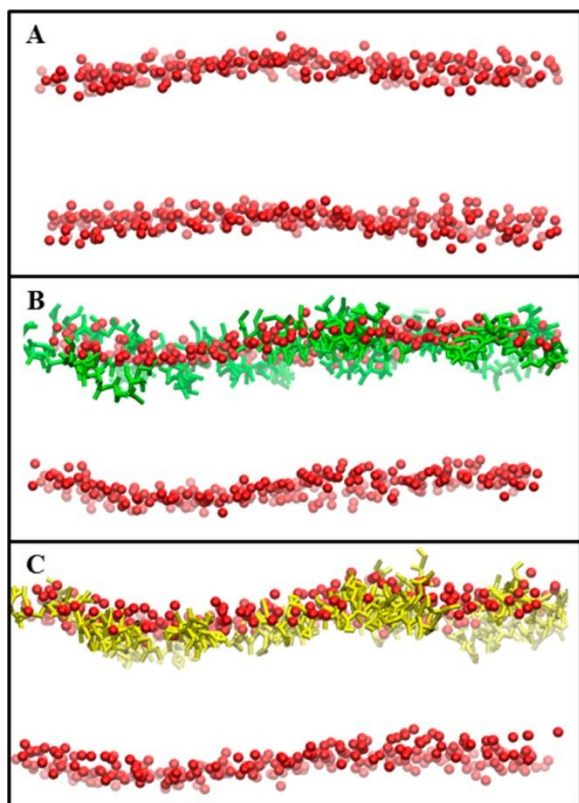


Figure 2.5: Bilayer structures obtained from some of the simulations performed in this study. To see better the curvature in the membrane, carbon chains of the lipids and water molecules are deleted. Only phosphate headgroups (PO4 particles) are represented here in red. Panel A is the membrane without any protein, simulated under the NPT ensemble. Panel B shows a bilayer with 18 melittins (green) in the top leaflet, simulated in the NPzAT ensemble. Panel C represents a bilayer with 18 magainin-h2 (yellow) molecules in the top monolayer, also simulated in the NPzAT ensemble.

Chapter 3: Mechanism of Membrane Poration by Shock Wave Induced Nanobubble Collapse: A Molecular Dynamics Study²

3.1 Introduction

The interaction of shock waves with biological cells is a subject of active research^{79–85}. This interaction can produce both positive and negative effects: controlled shock waves have a potential for medical use, since they increase the permeability of cell membranes⁸⁶ and this allows various macromolecules, such as drugs and also genetic material to enter the cell^{4,26,27,87–92}. On the negative side uncontrolled shock waves produced during a blast may damage brain cells, thus causing blast induced traumatic brain injury (bTBI) and neural cell damage or even its death. To understand the details and the role of shock waves in bTBI, experiments^{9,82,93,94} using shock tubes and also computer simulations^{83,95} have been performed. However, the mechanisms behind the bTBI, especially mild TBI (mTBI) are still not clearly understood, as the severity of TBI depends on several factors, such as shock wave amplitude, duration of exposure, distance from the blast, etc.

The effect of shock waves on biomembranes can be enhanced by the collapse of bubbles present in the vicinity of these membranes^{26–31}. Thus, ultrasound induced collapse of microbubbles is found to be responsible for the permanent poration of cell membranes^{26,96–99} due to the formation of a fluid jet as a result of a bubble collapse. Not only the collapse of

² This chapter previously appeared as an article in the Journal of Physical Chemistry B. The original citation is as follows: Adhikari U, Goliaei A, and Berkowitz M L, “Mechanism of Membrane Poration by Shock Wave Induced Nanobubble Collapse: A Molecular Dynamics Study,” *Journal of Physical Chemistry B* 20, no. 119 (May 2015): 6225.

microbubbles, but also of nanobubbles is considered to have a potential to produce substantial pores in a cell membrane due to a shock wave impact^{79,83,100}. Although there was some debate about the existence of nanobubbles in the past, recent research suggests their viability^{101–106}.

Detailed information about the process of nanobubble collapse due to an impinging shock wave and the resulting damage to a biomembrane can be obtained from molecular simulations. Recently Choubey et al.⁷⁹ observed in their all-atom molecular dynamics (MD) simulations a shock wave induced nanobubble collapse that formed a nanojet. This nanojet had a high velocity and moved toward the membrane, creating a nanopore in it, thus allowing permeation of water and other bigger molecules across the membrane. Our group also investigated recently^{83,100} the effect of shock wave induced collapse of a single and also multiple nanobubbles by using coarse-grained (CG) MD simulations. The results from our CG MD simulations were in a nice agreement with the all-atom simulations performed by Choubey et al.⁷⁹ Although, as we observed, the pores often recovered, some lipids from membranes were expelled out of the bilayer, even forming micelles in some cases, depending on the shock velocities. Also, as we observed, the damage to the membrane depended on the size of the nanobubbles. For instance, the collapse of a nanobubble of a diameter $D = 40$ nm produced a bigger pore and it took a longer time for the membrane to recover, compared to the case when a nanobubble of a diameter $D = 20$ nm collapsed. We also studied the effect on the membrane when multiple nanobubbles, positioned in different arrangements, collapsed under the impinging shock wave¹⁰⁰ and observed that more damage to the membrane was done when two nanobubbles were placed in a serial arrangement with respect to each other, compared to cases when nanobubbles were placed in other configurations, like parallel and/or slanted.

The previous work that studied the effect of shock waves, but in the bubble absence, demonstrated that the peak pressure and the duration of the membrane exposure to the shock wave are major contributing factors that determine the degree of cell membrane damage. It was determined in that work that when the shock wave impinges on the membrane, it is the pressure impulse, rather than the peak value of the pressure, that is usually considered^{80,81,99}. The impulse (I) is defined as the time integral over shock wave pressure profile:

$$I = \int_0^{t^+} P(t) dt \quad (3.1)$$

where $P(t)$ is the shock wave pressure and t^+ is the time duration of the positive phase of the shock wave⁸⁰. It was also observed^{80,86} that when the impulse was above a certain value, the cell membrane as a whole became severely damaged, resulting in a cell death. In the presence of bubbles, a bubble collapse produces a nanojet that causes a localized damage to the membrane by creating small pores in it. Can an impulse, defined above, still be a measure of the possible damage produced by shock waves to membranes when a bubble is present? There are some other questions related to the understanding of a nanobubble collapse induced membrane poration that still require answers. For example, why a shock wave of certain impulse and shock velocity does not form a pore in the membrane, whereas a nanojet formed by a nanobubble collapse produces one? What are the major differences in the shock wave impact in the presence and absence of nanobubbles in the vicinity of the membrane?

This kind of questions probably may be answered by carefully observing mechanistic details of the events, specifically pressure distributions at various stages of shock wave induced nanobubble collapse and nanojets hitting the membrane. Therefore, in this paper we present the results from MD simulations we performed to get an insight into the pressure behavior when

shock waves hit nanobubbles next to lipid bilayers that model cell membranes. In our simulations nanobubbles (diameter $D = 60$ nm) are induced to collapse via shock wave propagating toward the bilayer membrane. Different impulses of shock wave and various particle velocities are chosen to create various magnitudes of damage to the membrane. Pressure distribution at the membrane position is calculated at various stages of shock wave simulation, both in the presence and absence of the nanobubble. Nanobubble with a diameter $D = 20$ nm is also considered for a comparison purpose. We observe that 2-dimensional pressure distributions obtained at the membrane position accurately reflect the difference between the shockwave impact in the presence and in the absence of nanobubbles. We also studied what happens when a nanobubble collapses without the presence of a shock wave and the effects observed in this case are compared with the effects produced in the presence of shock waves.

3.2 Methods

All computer simulations were performed using Gromacs 4.6.6 package,^{67,107–109} except that the pressure calculation was done using Gromacs-4.0.2_local pressure⁷⁷ version of Gromacs. We described the interactions by the CG MARTINI^{22,110} force field, since it is widely and often successfully used in biomolecular simulations of systems containing lipid membranes^{65,73}. Our membrane was modeled by a lipid model bilayer consisting of dipalmitoylphosphatidyl choline (DPPC) lipids. The lipid bilayer contained 32 768 DPPC CG molecules and it was constructed by replicating a small bilayer containing 128 DPPC molecules 16 times in x and y directions. After energy minimization of the bilayer, it was solvated by 11 444 725 (~ 11.5 million) nonpolarizable CG water molecules. This system containing water and lipids was energy minimized and equilibrated in the isothermal–isobaric (NPT) ensemble for 20 ns at temperature of 323 K and pressure of 1 bar under semi-isotropic conditions. The time step in the equilibration

run was 30 fs, and Berendsen's scheme⁶⁸ was used to keep constant temperature and pressure. The time constants for temperature and pressure couplings were equal to 0.3 and 3 ps respectively, and compressibility was 3×10^{-5} bar. Nonbonded interactions were cut off at 1.2 nm using the shift scheme. The size of the system after equilibration was $101.1 \times 103.4 \times 137.5$ nm in x , y and z directions, respectively, with the membrane positioned in parallel to the xy plane at $z \approx 90$ nm.

Shock wave simulations were performed on this equilibrated system with added spherical nanobubbles that were created by removing water molecules from the inside of the bubble (i.e., actually creating a void). The shock waves were generated by using the momentum mirror protocol applied in this kind of simulations in the past^{79,111,112}. In this protocol all particles move with velocity v_p toward the mirror placed at the end of the box in the $-z$ direction; they get reflected upon impact, thus creating a shock wave moving with velocity greater than v_p in the $+z$ direction. This procedure in effect is equivalent to having a massive piston moving toward the $+z$ direction with velocity v_p and reflecting all the particles coming in contact with it, thus creating a shock wave. Periodic boundary conditions (PBC) were applied only in the x and y directions and not in the z direction. A 2 nm vacuum layer was added at the end of the system along the z direction, so that the particles would not overlap and collide with the mirror at the very beginning of the simulation. To mimic the propagation of smaller by value shock pulses, the piston was stopped after a short time and the shock wave formed was allowed to continue with its motion in the $+z$ direction. Various piston stop times were chosen to create shock waves of various impulses. All shock simulations were performed in constant energy ensemble and the cutoff value for interactions was 1.4 nm instead of the usual 1.2 nm for better energy conservation. The neighbor list was updated every 5 steps, instead of the usual 10. The time step

in the shock simulations was 4 fs. The shock velocity was calculated by identifying the discontinuity in density along the $+z$ direction. Pressure was calculated by using the method developed by Ollila et al.⁷⁷ and was obtained by discretizing the system into small cubes of dimensions 0.5 nm. The time intervals reported here are actual simulation times and not the equivalent times often reported for simulations with MARTINI. Figures were created using the VMD program⁷⁸.

For a given choice of a piston velocity or stoppage time, presence or absence of a bubble, we performed a number of simulations that differed from each other by a choice of the initial conditions. In all simulations with the same parameters, but different initial conditions, the results looked very similar and therefore we report here the results from one of each of the simulations of certain type. The types of the systems we discuss in this paper are summarized in Table 3.1

3.3 Results

As stated in the Methods, shock waves were created using the momentum mirror approach, a diagrammatic sketch of which is shown in Figure 3.1. Once the particles hit the piston with velocity v_p (particle velocity), they are reflected and create a region of higher density that moves with a higher velocity v_s (shock wave velocity). After a short time (denoted by “ τ_s ” here) we stopped the piston, but the shock wave continued to propagate in the $+z$ direction. Such shock wave propagation can be clearly seen in the panels shown in Figure 3.2, depicting the 2-dimensional water density plots. At the beginning of the shock wave propagation, at $t = 0$ ps, the shocked region at the extreme left is depicted in bright red. The propagation of the shock region with time is clearly seen in the panels, since the bright red region moves in the $+z$ direction. As

the shock wave continues to propagate, both its intensity and velocity decrease. For completeness and comparison of the density profiles of water when the shock wave propagates in the systems with and without the bubble we show in Figure 3.3 the 2-dimensional water density plots in the presence of the nanobubble. More details about these density plots and water jet properties when the bubble collapses, can be found in the previous work⁸³. In this work we concentrate on the study of pressure profiles in the membrane region.

By stopping the piston at various times, shock waves with various impulses can be created. Similarly, one can vary particle velocities to change the shock wave impulses. Below we report results from simulations using different values of v_p , different τ_s and also different values of the nanobubble diameter. To understand the role of the bubble we also simulated a system with no bubble present.

3.3.1 Shock Wave Simulations with Particle Velocity (v_p) = 1.0 km/s

Here we discuss the results from simulations with $v_p = 1.0$ km/s. To see how the piston stop time influences these results, we performed simulations with $\tau_s = 3$ ps, and 5 ps. Because the shock wave is moving in the z -direction, we calculated the change of the normal pressure component, P_{zz} , and since we are interested in the properties of the membrane, we measured the pressure at the membrane position and studied it as a function of time.

3.3.1.1 (a) Simulations with $\tau_s = 3$ ps

The change in average normal pressure across membrane surface (the pressure profile) for simulation with $\tau_s = 3$ ps of a system without a bubble is shown in Figure 3.4. This pressure profile displays the classical Friedlander curve seen for shock waves. According to Friedlander profile, as the shock wave arrives, there is a sharp rise in pressure (positive phase) followed by a

very rapid decrease of pressure, which reaches a minimum at a negative value, and then the pressure rises again toward the normal pressure. The pressure value remains at 1 bar until the shock wave arrives. Upon the shock wave arrival, the pressure rises very sharply up to a value of 478 MPa (at ~ 40 ps of the simulation time), then it gradually decreases, becoming negative and reaches the peak negative pressure value (-76 MPa) at ~ 104 ps. As in the Friedlander curve, the pressure returns to normal, and in our simulation it happens at time ~ 128 ps. Although the pressure peak value is very high, the duration of the shock impulse is very short and therefore the value of the impulse I from eq 3.1 in our simulation is only 8.96 mPa s. This value is much smaller than the experimentally measured⁸⁰ value of an impulse of 54 Pa s, that caused only an uptake of calcein molecules into the cell, but not the cell death. Therefore, we should not expect that a major damage to the membrane occurs when a shock wave with an impulse of 8.96 mPa s hits a cell membrane. A two-dimensional diagram showing the pressure across the x and y axes of the membrane helps to understand how the distribution of normal pressure changes as the shock wave passes through the lipid bilayer, and this diagram is depicted in Figure 3.5. Notice that the average pressure calculated from the 2-d map at a certain time corresponds to a value of the pressure from Figure 3.4 at that particular time. For instance, the average pressure of Figure 3.5b is equal to 478 MPa corresponding to the value of pressure at point “b” in Figure 3.4. As we can see from Figure 3.5, for a system containing just water and the bilayer and exposed to a shock, the pressure is distributed homogeneously along the surface of the bilayer and the values of the pressure fluctuations are very small. Thus, as the shock arrives at the membrane, the entire bilayer is experiencing the same pressure with forces pointing in the same direction. The snapshots of the bilayer membrane at various shock simulation times are shown in Figure 3.6. As this figure shows, even when a shock wave hits the membrane with an impulse of 8.96 mPa s and

a peak pressure of 478 MPa, the membrane remains intact. Although no pore formation was observed, the bilayer has undergone slight compression as the shock wave reached the membrane at 40 ps, but it returned to an original shape after the shock wave passed through, as can be seen from Figure 3.6.

A completely different scenario is observed when a nanobubble is present in the vicinity of the membrane. In our simulations of systems containing a nanobubble with a diameter $D = 60$ nm, the bubble was placed at a distance about 3 nm away from the membrane and its center coincided with the membrane center in x and y directions. As the shock wave propagated toward the membrane, it initially impinged on the nanobubble and after some period of time hit the bilayer. The shock wave induced nanobubble collapse produced a nanojet of water particles moving with high velocity, and this nanojet moved in the same direction as the shock wave. The profile of the membrane pressure (for simulation with $\tau_s = 3$ ps) in the presence of the nanobubble is shown in Figure 3.7. Several differences can be seen between the profiles from Figure 3.4 (simulation without a bubble) and Figure 3.7 (simulation with a bubble). Although the shock wave hits the membrane at the same time (~ 40 ps), the peak pressure (~ 217 MPa) and the impulse due to the shock wave (2.52 mPa s) measured as an integral over pressure values in the first positive region in Figure 3.7 are smaller in the latter case. These smaller values are due to the presence of the bubble that hinders the shock wave propagation. Another clear difference in this pressure profile can be seen in the behavior of the pressure, after the shock wave pressure enters its negative phase. Unlike in the case of the bubble absence, after the shock wave entered its negative phase, the pressure started to rise toward high positive values reaching a value of ~ 50 MPa delivering an additional 2.93 mPa s of positive impulse. The second peak in pressure is due to the pressure created by the nanobubble collapse. Despite the deliverance of a smaller total

positive impulse and that the peak pressure initially had a smaller value in case when the nanobubble was present, we observed that the collapse of a nanobubble resulted in a formation of a pore in the membrane.

To understand why poration occurred we again looked at the distribution of the pressure on the membrane surface. Since the nanobubble is located next to the membrane center along x and y axes we expected to see a high pressure region at the center of the membrane after the nanobubble collapses into it. Indeed, the 2-dimensional pressure maps at various simulation times, shown in Figure 3.8, display an interesting pattern of pressure distribution along the x and y axes. Before the shock wave hits the membrane (Figure 3.8a), the pressure is close to 0 MPa, just like in the system without a nanobubble. But as the shock wave hits the membrane, the pressure distribution map looks distinctly different from the map for the system without a bubble. At 40 ps (Figure 3.8b), which is the time when the membrane experiences the peak pressure, the pressure is lower at the center (blue color), whereas it is higher (~ 300 MPa) in the surrounding of the small circular central region. The lower pressure region at the center is due to the presence of the bubble in front of it, which hinders the initial shock wave and also lowers the average peak pressure. As the simulation progresses, the shock wave passes the membrane and the negative pressure phase starts to build-up at the membrane at about 60 ps. At the time when the negative pressure is building up, the nanobubble collapses, producing a high-pressure region at the center of the membrane. So, at the same time when the negative pressure is building up in other region of the membrane, a positive pressure build up takes place at the center of the membrane. Figure 3.8 shows that as time progresses from 60 to 70 ps of the simulation, the difference in pressure between the central higher pressure region (red) and lower pressure region (blue) increases. This unequal pressure distribution persist and increases in time up to 80 ps, and

it is responsible for the poration of the membrane, since it produces forces acting on the membrane in different directions. After the nanojet passes through, the pressures gradually decrease and their distribution becomes homogeneous again (Figure 3.8h). The snapshots of the membrane for this simulation are shown in Figure 3.9. We observe that as the difference in pressure values builds up at the membrane, the pore formation starts (~ 80 ps, see Figure 3.9e) and a bigger pore can be observed at ~ 128 ps of the simulation time (Figure 3.9h).

3.3.1.2 (b) $\tau_s = 5$ ps

As expected, similar results are obtained when the piston is stopped after 5 ps of its motion, instead of 3 ps, but the effects of the shock wave impact are much more pronounced in this case. The pressure profiles at the membrane for $\tau_s = 5$ ps are given in Figures 3.10a and 3.10b. Figure 3.10a represents the pressure profile for the system with no bubble. The shock wave hits the membrane at 32 ps, slightly earlier than in case when $\tau_s = 3$ ps, and the peak pressure reaches a value of 1126 MPa, which is more than twice the value of pressure reached in the simulation with $\tau_s = 3$ ps. The positive phase impulse is 17.57 mPa s. The negative phase also starts earlier, at about 78 ps. No pore formation is observed even when transferring this impulse. Just like in case of $\tau_s = 3$ ps, the pressure distribution map shows an equal pressure distribution along the x and y axes of the membrane. The pressure distribution maps and snapshots of the membrane at various simulation times are given in Figures 3.11 and 3.12.

Figure 3.10b displays the pressure profile for the system with a nanobubble. In this case, after the shock wave hits the membrane at 32 ps, the pressure stays positive for a longer time duration. Moreover, the figure shows the presence of two shoulders in the main peak, which are due to the nanobubble collapse. Unlike in case with $\tau_s = 3$ ps, where two separate peaks were

observed due to shock wave and nanojet, in $\tau_s = 5$ ps case the nanojet pressure peak hits almost immediately after the shock wave has passed. This is not surprising given the velocity of the shock wave, so that nanojet moves much faster than in case with $\tau_s = 3$ ps. The total positive impulse is 14.93 mPa s and the peak pressure is 533 MPa. The pressure distribution map is similar to that of the map in case $\tau_s = 3$ ps, but the difference in values for the higher (red at the center) and lower (blue) pressure regions is much larger in this case. This bigger inequality in pressure results in the formation of a larger sized pore and more damage to the membrane. The 2-dimensional pressure maps and snapshots of the membrane at various simulation times are presented in Figures 3.13 and 3.14, respectively.

3.3.2 Shock Wave Simulations with Particle Velocity (v_p) = 0.5 km/s

Two piston stopping times ($\tau_s = 5$ and 10 ps) were chosen for the simulations with 0.5 km/s particle velocity. The pressure profiles obtained at these conditions are shown in Figure 3.15. As the particle velocity is smaller than in the previously described cases, the shock wave velocity also becomes smaller. Because of this reason the shock wave arrives at the membrane later and the peak pressure is smaller as well.

When $\tau_s = 5$ ps, the shock wave arrives at the membrane at about 48 ps. The peak pressure is just 71 MPa and the total positive impulse is 2.27 mPa s. These values are around five times smaller than in case when $v_p = 1.0$ km/s. The pressure wave generated by the nanojet reaches the membrane at 124 ps. The 2-d pressure maps and the snapshots of the membrane at various times are given in Figures 3.16 and 3.17, respectively. As we can see from Figure 3.16, when the nanojet arrives at the membrane and hits it, the pressure at the center of the membrane becomes bigger and decreases as we go away from the center, just like in case when $v_p = 1.0$

km/s. But the unequal distribution of the high and the low pressure regions is substantially smaller (maximum 30 MPa), and as a result no pore formation in the membrane occurs. If $\tau_s = 10$ ps, the shock wave arrives at the membrane at 36 ps, slightly earlier than when $\tau_s = 5$ ps. The peak pressure rises up to 276 MPa and the total impulse is 5.49 mPa s. These values are close to the corresponding ones from simulations with $v_p = 1.0$ km/s and $\tau_s = 3$ ps. The normal pressure distribution along x and y axis at the membrane and size of the pore formed also resemble that of $v_p = 1.0$ km/s and $\tau_s = 3$ ps (as shown in Table 3.1). The pressure maps and snapshots of the membrane at various simulation times are provided in Figures 3.18 and 3.19, respectively. Thus, our simulations show that one can vary either the particle velocity or the time of the piston motion creating the shock wave to produce same result.

3.3.3 Shock Wave Simulations with a Smaller Nanobubble (Diameter, $D = 20$ nm)

A system having a smaller nanobubble ($D = 20$ nm) was also considered for the comparison purposes. Particle velocities of 1.0 km/s, and $\tau_s = 3$ ps were chosen in this case. The pressure profile for this system is shown in Figure 3.20. The peak pressure (~ 348 MPa) and the total impulse (7.19 mPa s) of the shock wave hitting the membrane are slightly larger than in the case of 60 nm bubble due to lesser hindrance posed by the smaller bubble. But the impulse created by the nanojet itself is smaller, and the impact area on the membrane is also smaller. Another difference between the two cases is that the bigger bubble collapse takes a longer time and nanojet hits the membrane after the shock wave completely passes it, whereas in the smaller bubble case the nanojet collapse on the membrane occurs immediately after the shock wave passed. This difference can be clearly seen from the corresponding pressure profiles: separate peaks are seen in Figure 3.7 for the bigger bubble, whereas for the smaller bubble (Figure 3.20) the nanojet pressure peak is overlapping with the shock wave pressure peak. The normal pressure

distribution along the x and y axes of the membrane is similar to the distribution observed in case of the bigger bubble, as expected, but the impact of the nanojet pressure is focused on a smaller area of the membrane. This results in the formation of a smaller pore in the membrane. The 2-d pressure maps and snapshots of the membrane at various times are given in Figures 3.21 and 3.22.

3.3.4 Spontaneous Nanobubble Collapse (without Shock Wave)

The nanobubble can collapse spontaneously. If the surrounding is symmetrical, the bubble collapse will be also symmetrical, but if the bubble is located next to a membrane the collapse is asymmetrical and it may produce membrane damage. To see what happens during the spontaneous collapse of the nanobubble, we simulated a system containing a membrane and a nanobubble with $D = 60$ nm. The time step of 20 fs was used in these simulations. The results depended on the ensemble used. In case of the constant pressure and temperature (*NPT*) ensemble, the bubble collapsed completely at 2.2 ns. Since the membrane is located very closely to the edge of the bubble (~ 3 nm), the bilayer part closest to the bubble bended toward the center of the bubble and membrane became curved, although no pore formation in the membrane was observed. After the completion of the bubble collapse, the bilayer recovered to its original form at 30 ns. Some snapshots of the membrane at various simulations are provided in Figure 3.23. When we performed the simulation in the NPzAT ensemble, where the lateral area of the membrane was kept constant, a complete bubble collapse occurred at about 4.6 ns, which is twice the time interval needed to observe the collapse in the NPT ensemble. We observed that the membrane was less curved in this case, compared to the one from the simulation performed using the NPT ensemble, and that it fully recovered at about 25 ns. Again no pore formation was

observed. Thus, a spontaneous bubble collapse next to the membrane did not produce damage to membrane in the form of a pore.

3.4 Discussions and Summary

To understand the role of cavitation effect in the presence of nanobubbles, we performed simulations on systems containing model membranes and considered what happened when shock waves impinged on them, in absence or presence of the bubbles. As we observed, in the absence of a bubble a shock wave impulse of a rather small value of around 18 mPa s does not damage the membrane. We study cases with a small value of impulse, because we are interested in the possible damage to cell membranes produced during mild traumatic brain injury. We observed that the membrane was compressed for a short duration, but recovered within a short time. Our results are consistent with earlier simulations by Koshiyama et.al⁸¹ that did not see creation of pores in membranes, even when a shock wave had an impulse of 50 mPa s, but are in contradiction with the conclusion from the recently reported in the literature simulation⁸⁶ that an impulse bigger or equal to 0.45 mPa s damages the bilayer to an unrecoverable state. It should be noted that the system considered in that study was very small and a different methodology was applied for shock wave generation.

The presence of a nanobubble next to a membrane changes the result quite dramatically. In this case, once the shock wave impinges on the nanobubble, it induces its collapse, which results in the formation of a nanojet directed toward the membrane. The nanojet impinges on the membrane and makes a pore in it, even if the impulse transferred to a membrane is smaller than the one in pure shock wave case. Why is the membrane not damaged by a shock wave that hit the system when no bubble is present, but a pore is formed when a bubble is present, although the

pressure impulse in the system with no bubble can be larger than in the system with a bubble? To understand this we calculated pressure distributions along the plane of the membrane and found them to be very informative. Pressure distribution maps revealed that when the shock wave passes over the membrane it creates a negative pressure region on the membrane surface. At the same time due to the bubble collapse a positive pressure region appears at the membrane center. For example, in the case when $v_p = 1.0$ km/s, and $\tau_s = 3$ ps, the difference between positive and negative pressures is quite large, around 100 MPa. This unequal distribution of pressures causes a disbalance of stresses acting in different direction on the membrane, resulting in pore formation. Since it is the pressure distribution that is responsible for the membrane damage, we cannot use the impulse delivered to the membrane (eq 3.1) as the quantitative parameter that is correlated to the degree of the membrane damage. One can consider the total impulse that includes the impulse after the first shock and the consequent impulse due to pressure rise after the jet reaches the membrane as a factor in measuring the disruption, but more work needs to be done to establish quantitative criteria that predict membrane damage.

We already mentioned that a choice of parameters τ_s and v_p plays an important role. In fact, the unequal distribution of pressure on the membrane becomes much more pronounced if the piston is stopped at 5 ps instead of 3 ps. When $\tau_s = 5$ ps, the difference between the highest and lowest pressures is larger than 300 MPa, three times the difference observed in case when $\tau_s = 3$ ps. When we reduced v_p from 1.0 km/s to 0.5 km/s the maximum difference between the high and low pressure regions was not larger than 40 MPa and we did not observe a pore formation in the membrane. Interestingly, when the piston was stopped at 10 ps, (but v_p was still 0.5 km/s), the total impulse and the pressure distribution at the membrane was similar to that in the case when $v_p = 1.0$ km/s and $\tau_s = 3$ ps and similar pores in membrane were formed.

In summary, while the shock wave impinging on a lipid bilayer membrane may produce damage to it, the presence of nanobubbles located next to bilayer that are hit by the shock wave substantially increases the damage done to membranes. Since biological membranes represent much more complex systems than membranes containing just one lipid component, considered here, the next step in simulations is to study how the complexity of membranes influence the cavitation effect. Particularly interesting is to study how the proteins, such as channels behave when cavitation of bubbles occur.

Table 3.1: Summary of the results from shock wave simulations.

Bubble diameter, nm	v_p (km/s)	τ_s (ps)	Total I (mPa*s)	Velocity* of the shock wave (km/s)	Maximum velocity of the nanojet (km/s)	Maximum radius of the pore formed (nm)
60	1.0	3	5.45	2.16	2.06	15.3
	1.0	5	14.93	2.55	3.38	20.5
	0.5	5	3.00	1.87	1.06	No pore
	0.5	10	5.49	2.21	2.48	15.5
20	1.0	3	7.18	2.16	2.75	5.3
0	1.0	3	8.96	2.16	-	-
0	1.0	5	17.57	2.55	-	-

*velocity of shock wave at the time when it hits the membrane.

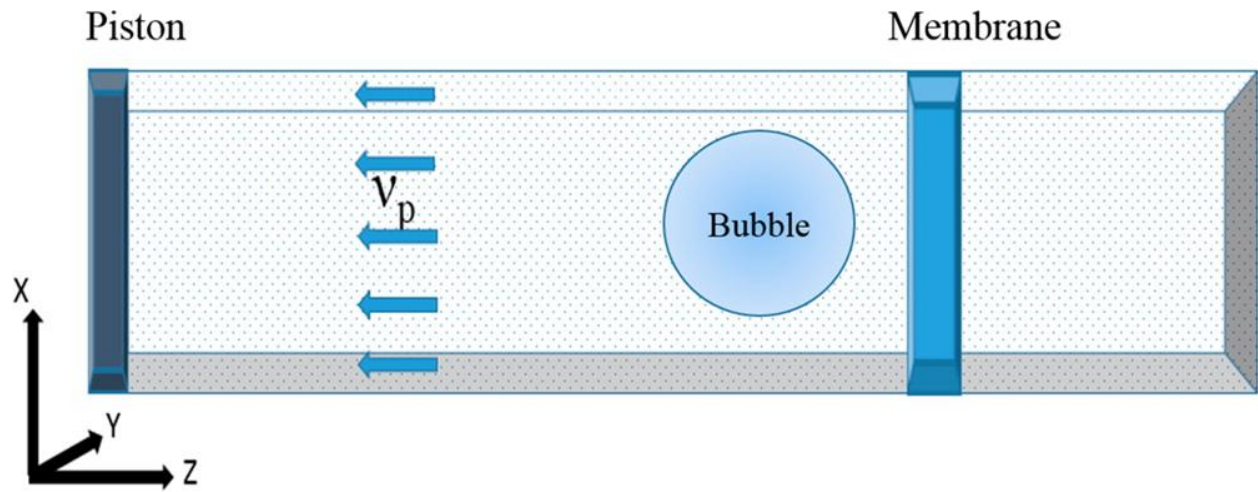


Figure 3.1: Representation of systems simulated in this work. We also simulated a system that did not contain a bubble and a system where a shock wave was not created.

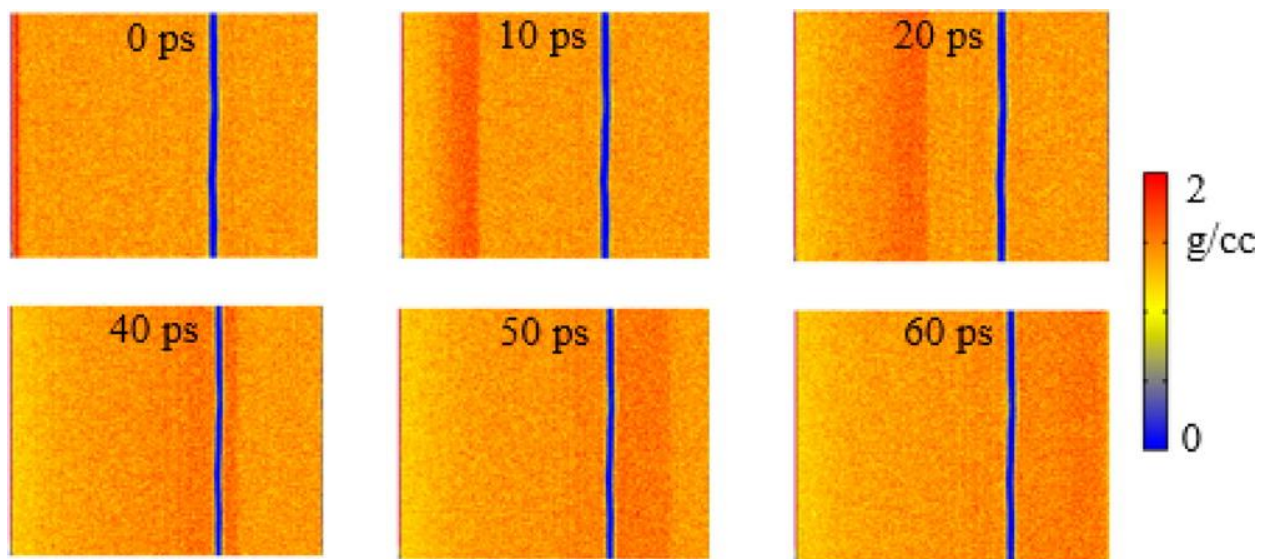


Figure 3.2: 2-Dimensional water density maps showing the propagation of the shock wave in a system without a bubble at various stages of simulations. In this case the piston stopped at 3 ps ($\tau_s = 3$ ps), and $v_p = 1.0$ km/s. The density decreases is coded in change of color from red to blue.

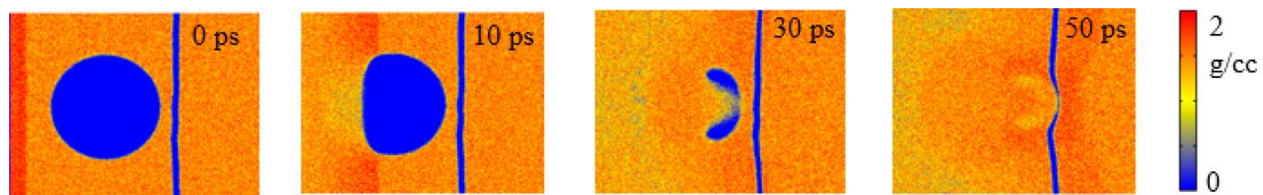


Figure 3.3: 2-Dimensional water density maps showing the collapse of a nanobubble after the shock wave ($\tau_s = 5$ ps and $v_p = 1.0$ km/s) passage. Only a slice of 20 nm in width is considered (from $X = 40$ nm to $X = 60$ nm) for a better view of the bubble collapse.

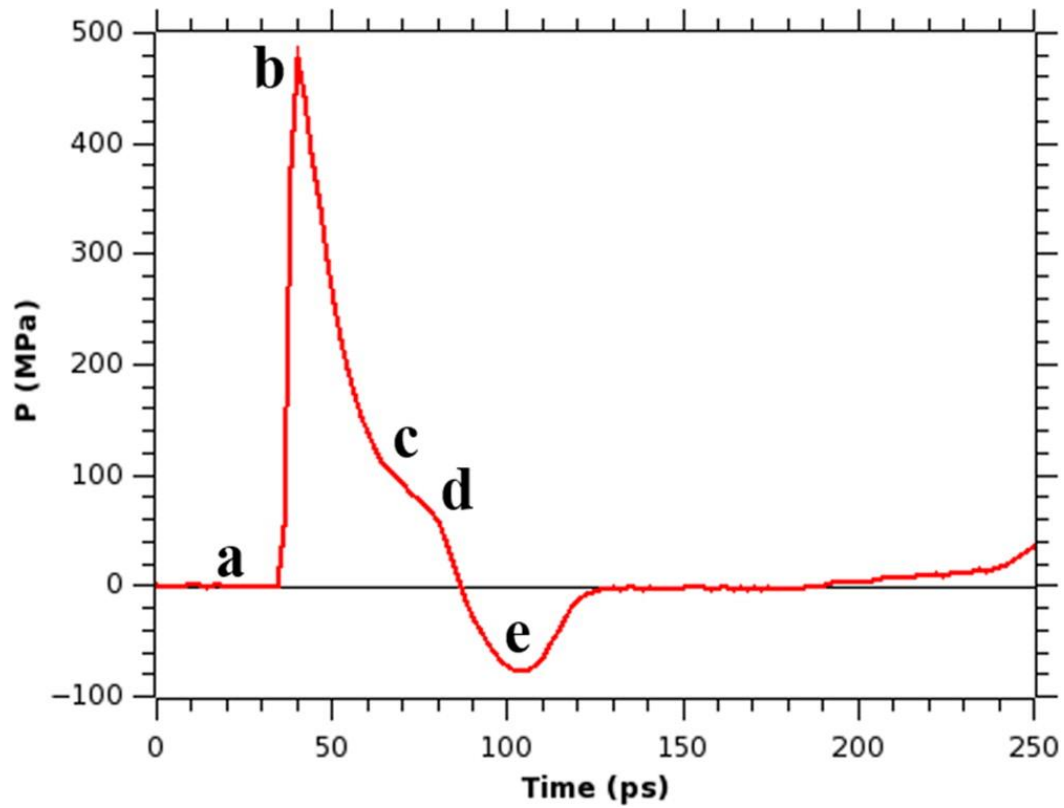


Figure 3.4: Time dependence of the pressure normal to the membrane surface (pressure profile at the membrane position) when $v_p = 1.0$ km/s and $\tau_s = 3$ ps in a system containing no bubble. The letters (a–e) correspond to different stages of the shock wave propagation.

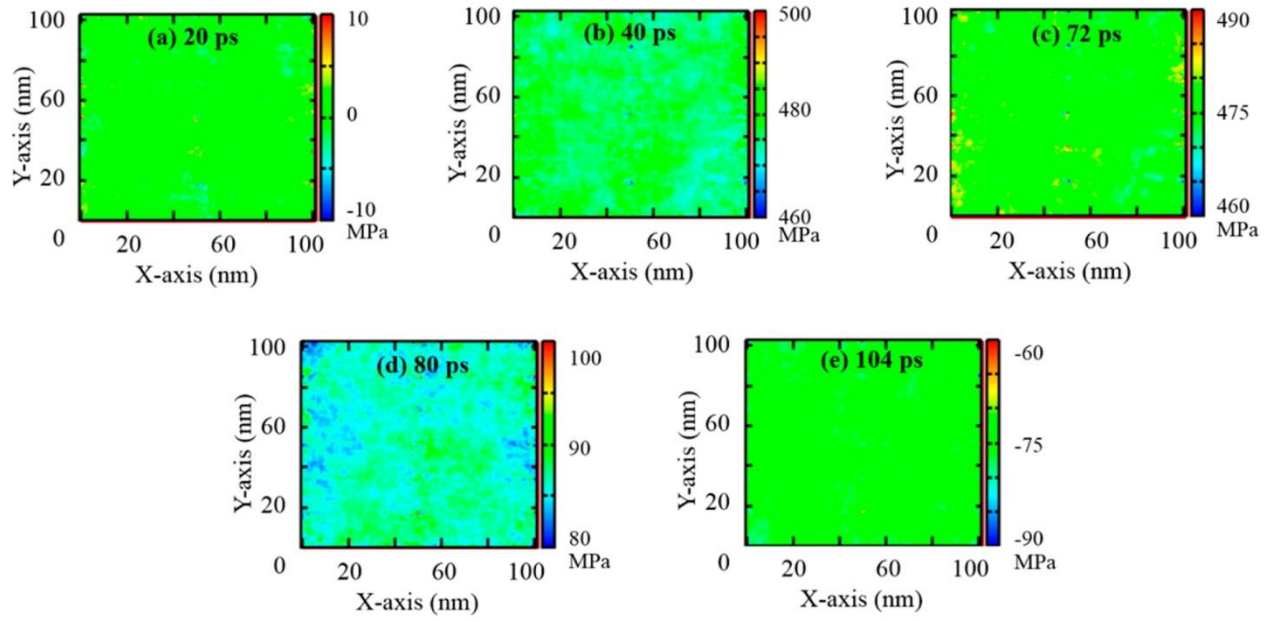


Figure 3.5: 2-Dimensional pressure maps at the membrane position at various times with $v_p = 1.0$ km/s and $\tau_s = 3$ ps in a simulation containing no bubble. The letters a–e correspond to the same stages as in Figure 4.

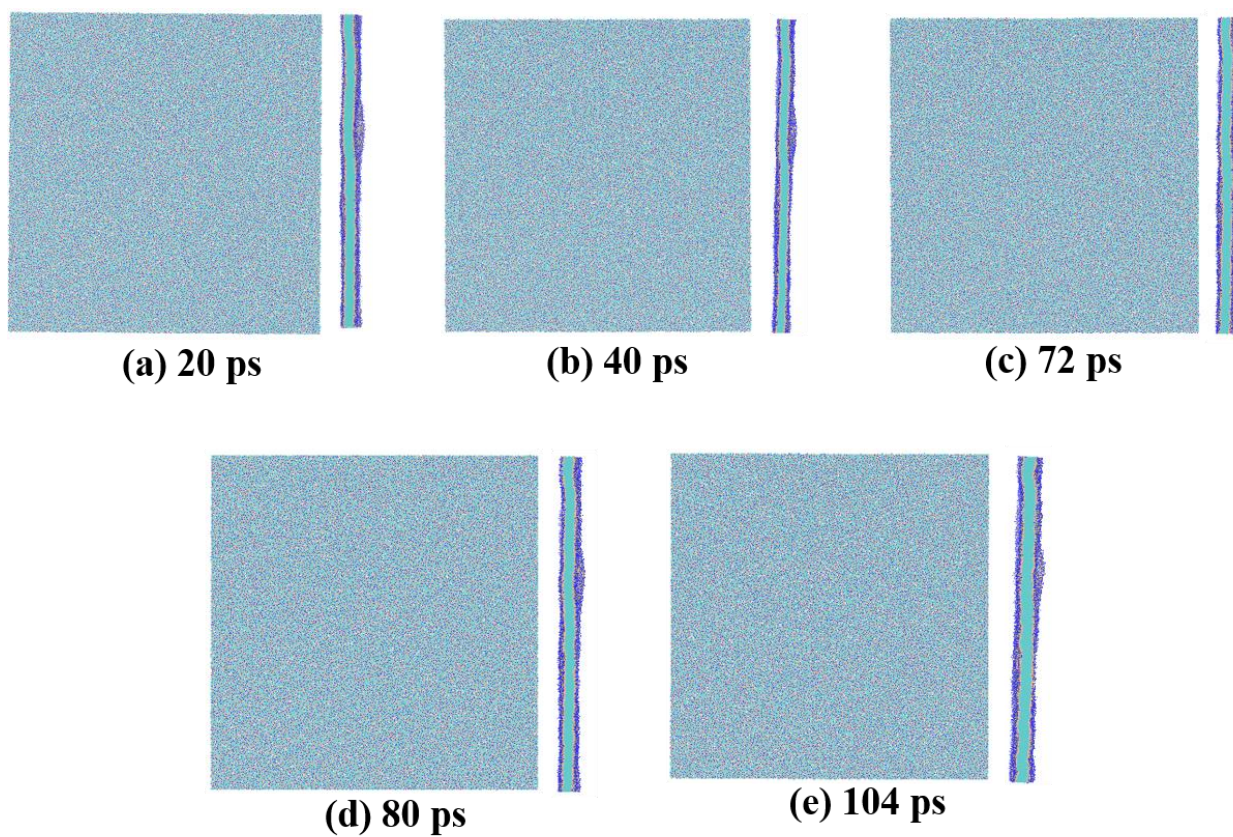


Figure 3.6: Snapshots of the bilayer membrane at various times of the simulations without a bubble when $v_p = 1.0$ km/s and $\tau_s = 3$ ps. The view from the top is on the left and the side view is on the right.

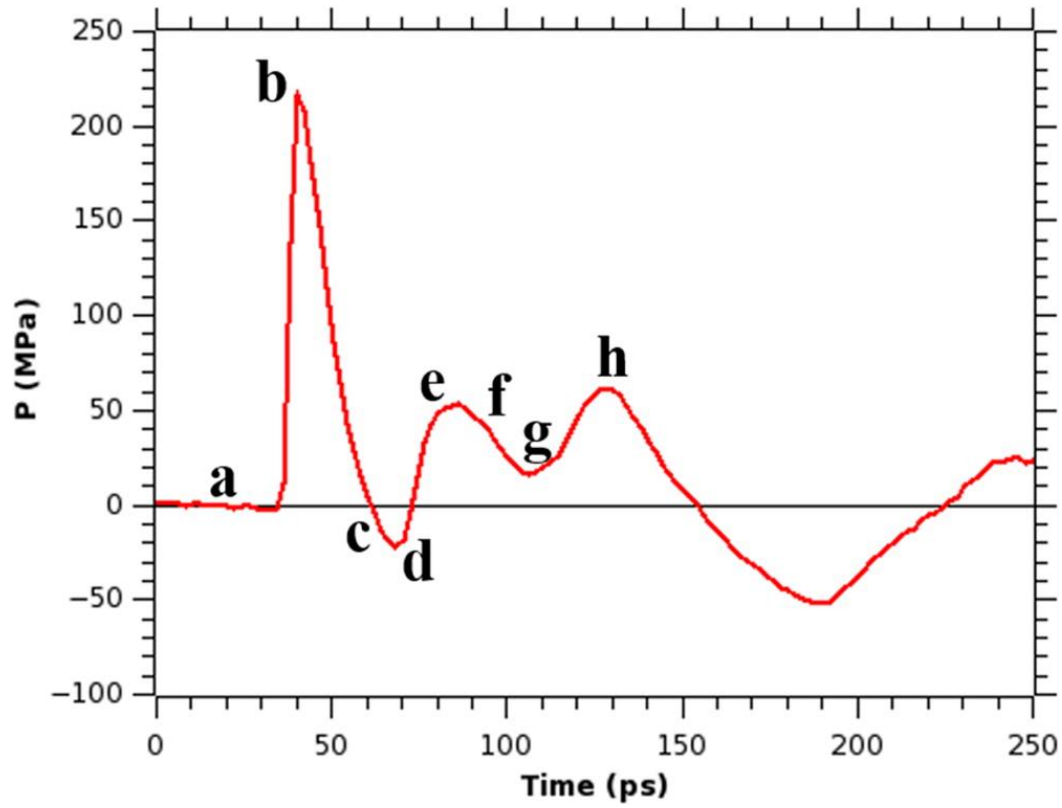


Figure 3.7: Pressure profile at the membrane when $v_p = 1.0$ km/s and $\tau_s = 3$ ps in a system containing a bubble with $D = 60$ nm. The letters a–h correspond to different stages of the shock wave propagation.

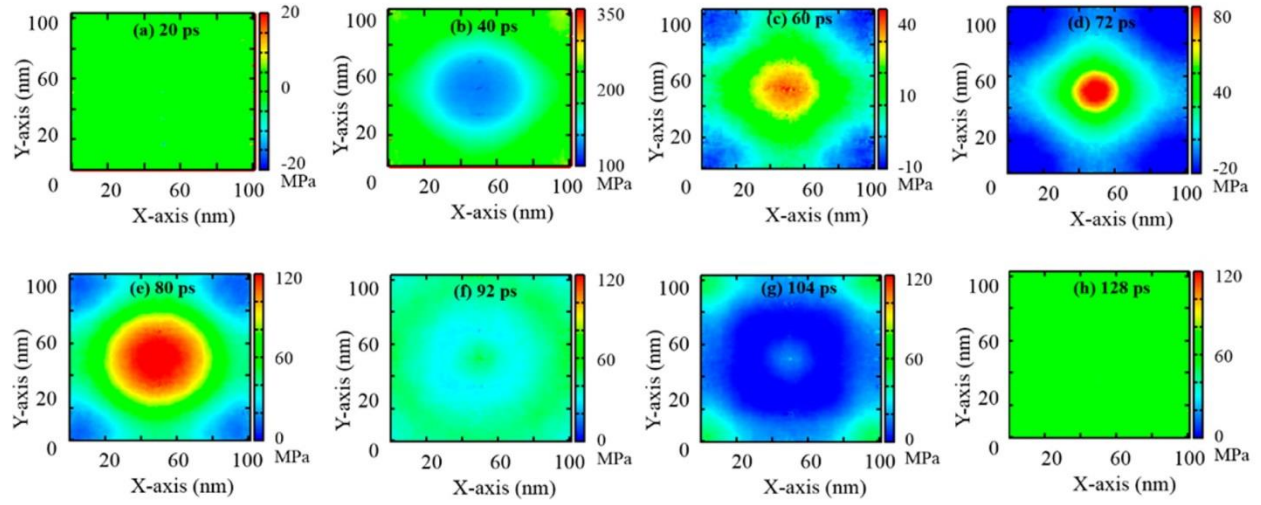


Figure 3.8: 2-Dimensional pressure maps at the membrane position at various times with $v_p = 1.0$ km/s and $\tau_s = 3$ ps in a simulation containing a bubble ($D = 60$ nm). The letters a–h correspond to the same stages as in Figure 6

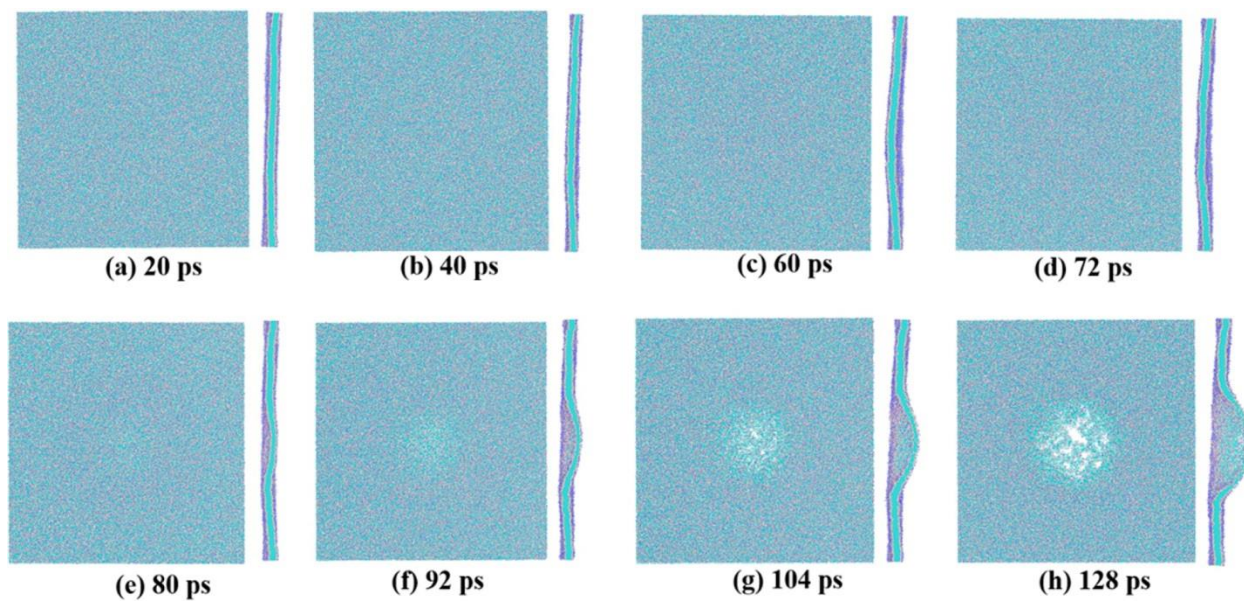


Figure 3.9: Snapshots of the bilayer membrane at various times of the simulations without a bubble when $v_p = 1.0$ km/s and $\tau_s = 3$ ps and $D = 60$ nm. The view from the top is on the left and the side view is on the right.

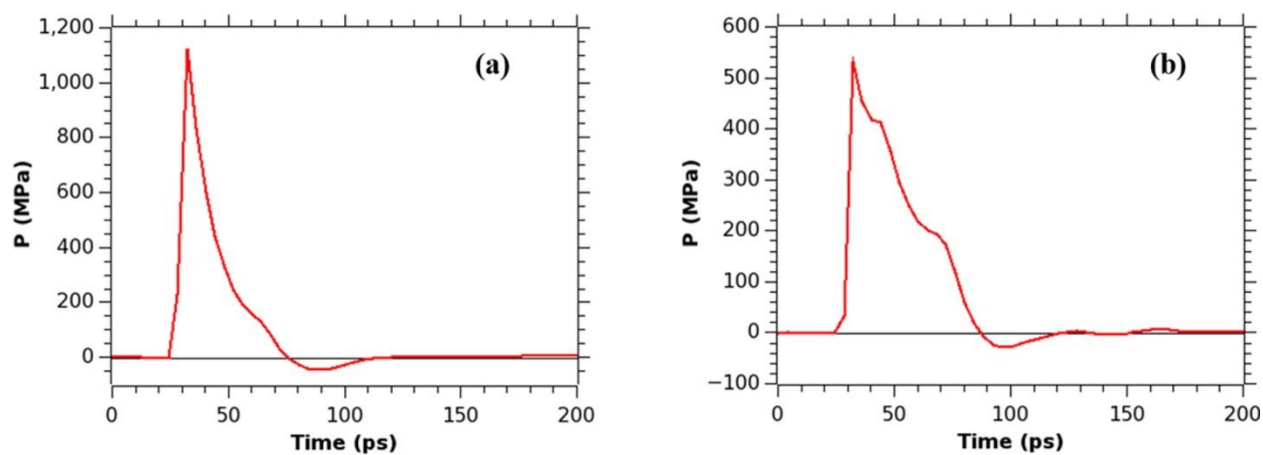


Figure 3.10: Pressure profiles at the membrane position in simulations with $v_p = 1.0$ km/s, $\tau_s = 5$ ps, (a) when there is no bubble is present or (b) when there is a nanobubble present ($D = 60$ nm).

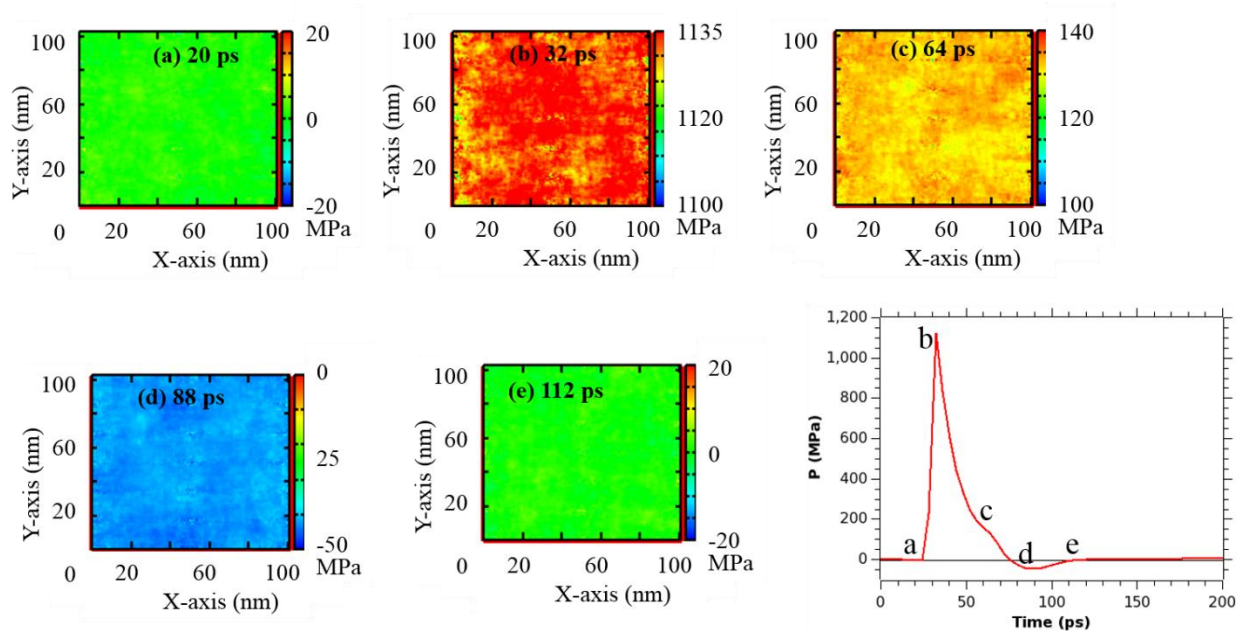


Figure 3.11: 2-dimensional pressure maps calculated at the membrane position at various times for the system containing no bubble and with $v_p = 1.0$ km/s and $\tau_s = 5$ ps. Range of units (in color) is in MPa. 1-dimensional pressure profile is placed on the bottom right side. Letters on 1-d profile refer to same moments of time as on the panels with 2-d profiles.

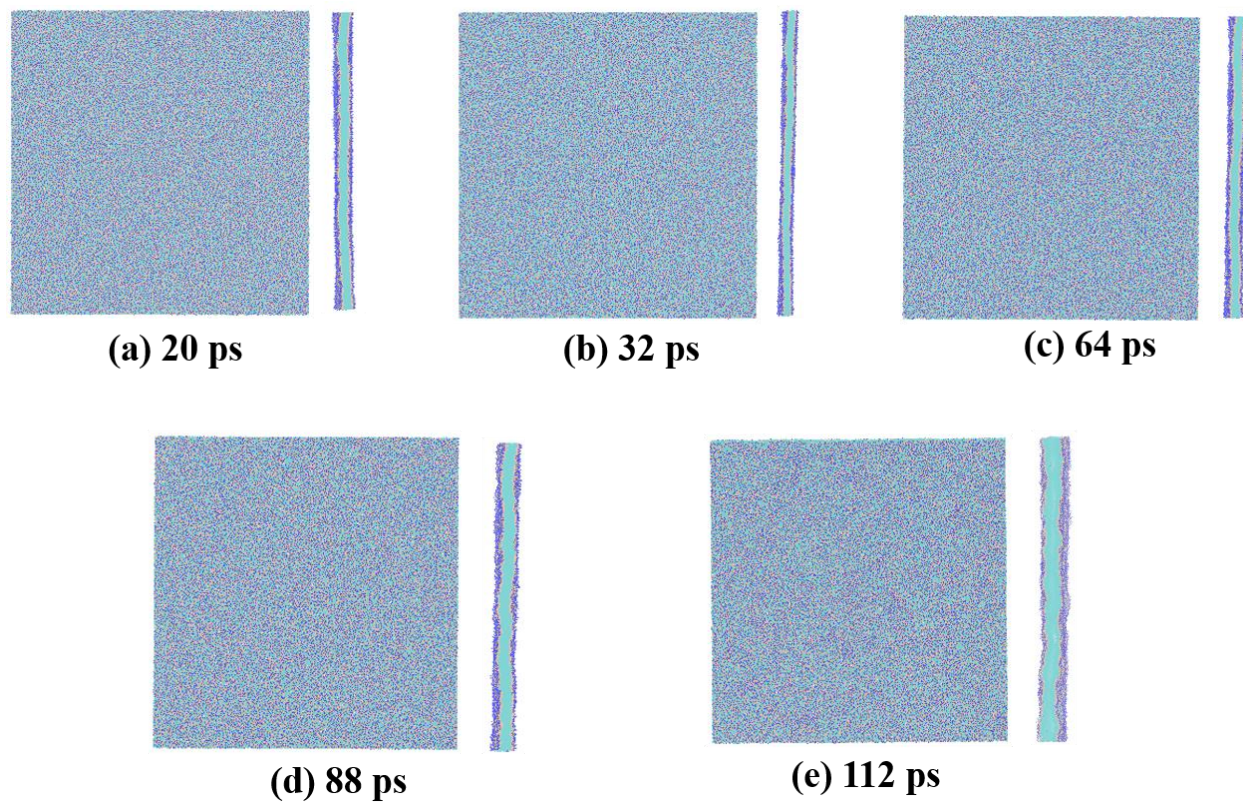


Figure 3.12: Bilayer membrane at various times of the simulation for the system with no bubbles; $v_p = 1.0$ km/s and $\tau_s = 5$ ps. Top views are on the left and cross sectional views are on the right.

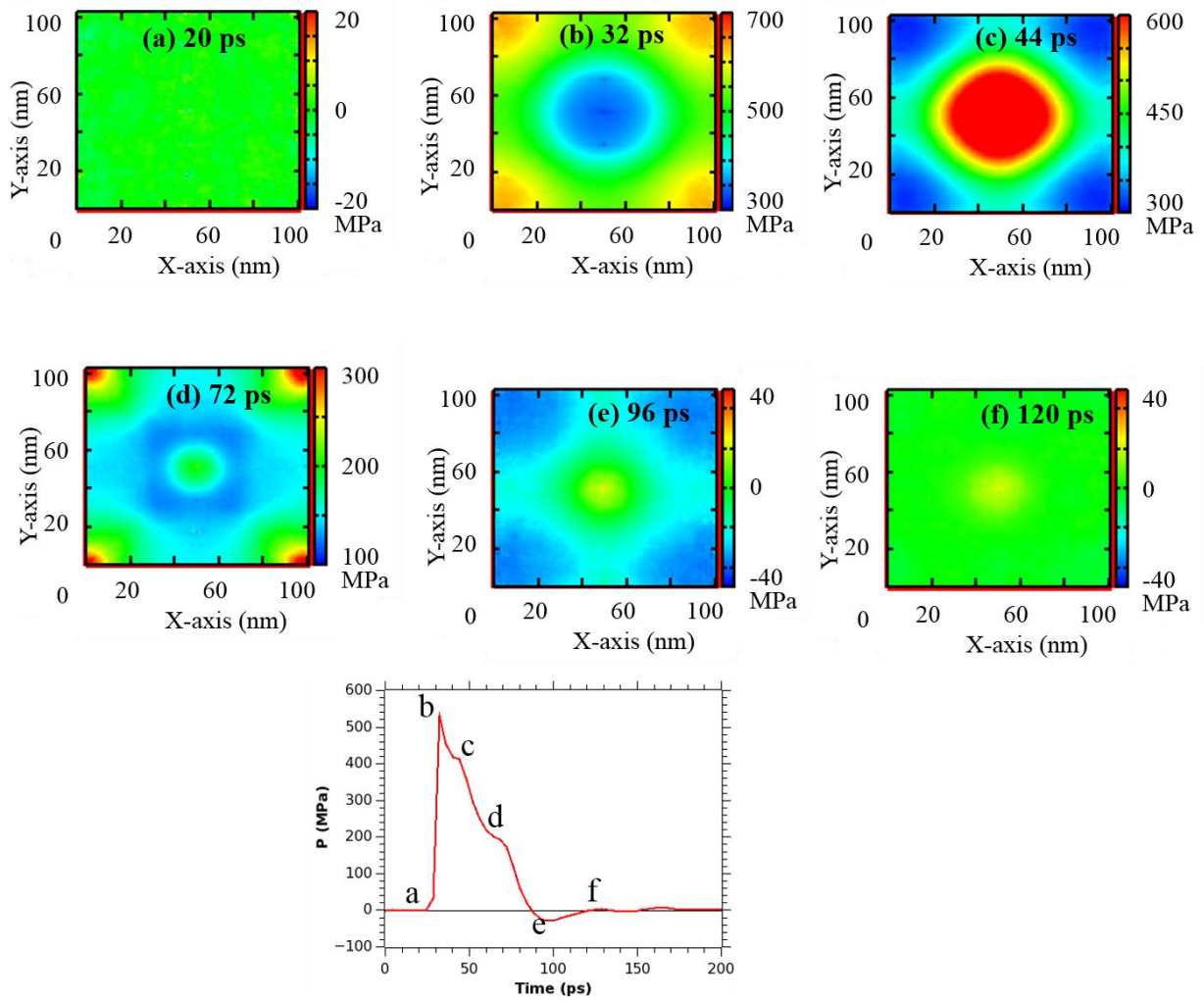


Figure 3.13: 2-dimensional pressure maps calculated at the membrane position at various times for the system containing a nanobubble ($D=60$ nm); $v_p = 1.0$ km/s and $\tau_s = 5$ ps. Range of units (in color) is in MPa. 1-dimensional pressure profile is placed on the bottom. Letters on the 1-d profile refer to same moments of time as on panels with 2-d profiles.

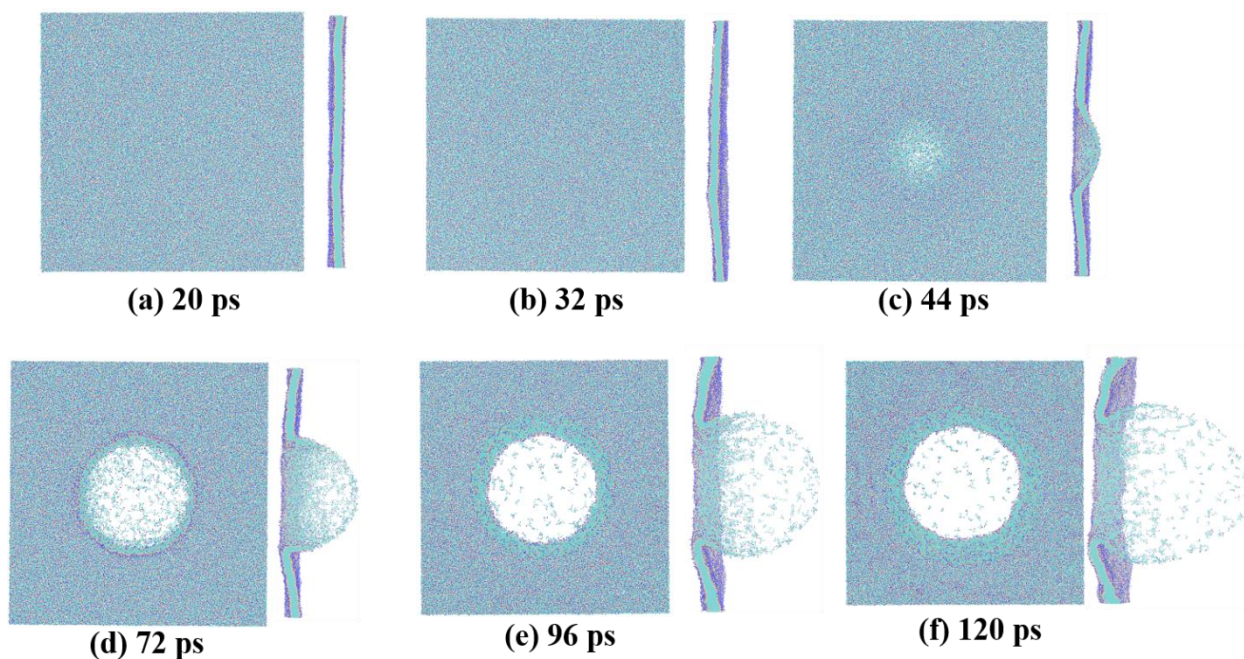


Figure 3.14: Bilayer membrane at various times of the simulation performed on a system containing a nanobubble ($D=60$ nm); $v_p = 1.0$ km/s and $\tau_s = 5$ ps. Top views are on the left and cross sectional views are on the right.

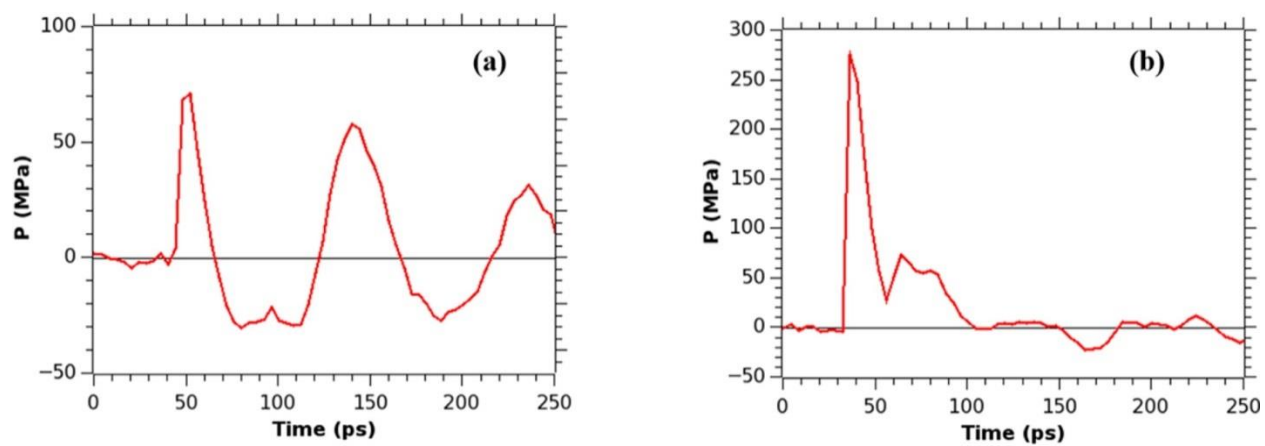


Figure 3.15: Pressure profiles at the membrane position in simulations with $v_p = 0.5$ km/s. (a) $\tau_s = 5$ ps and (b) $\tau_s = 10$ ps; in both cases a nanobubble is present ($D = 60$ nm).

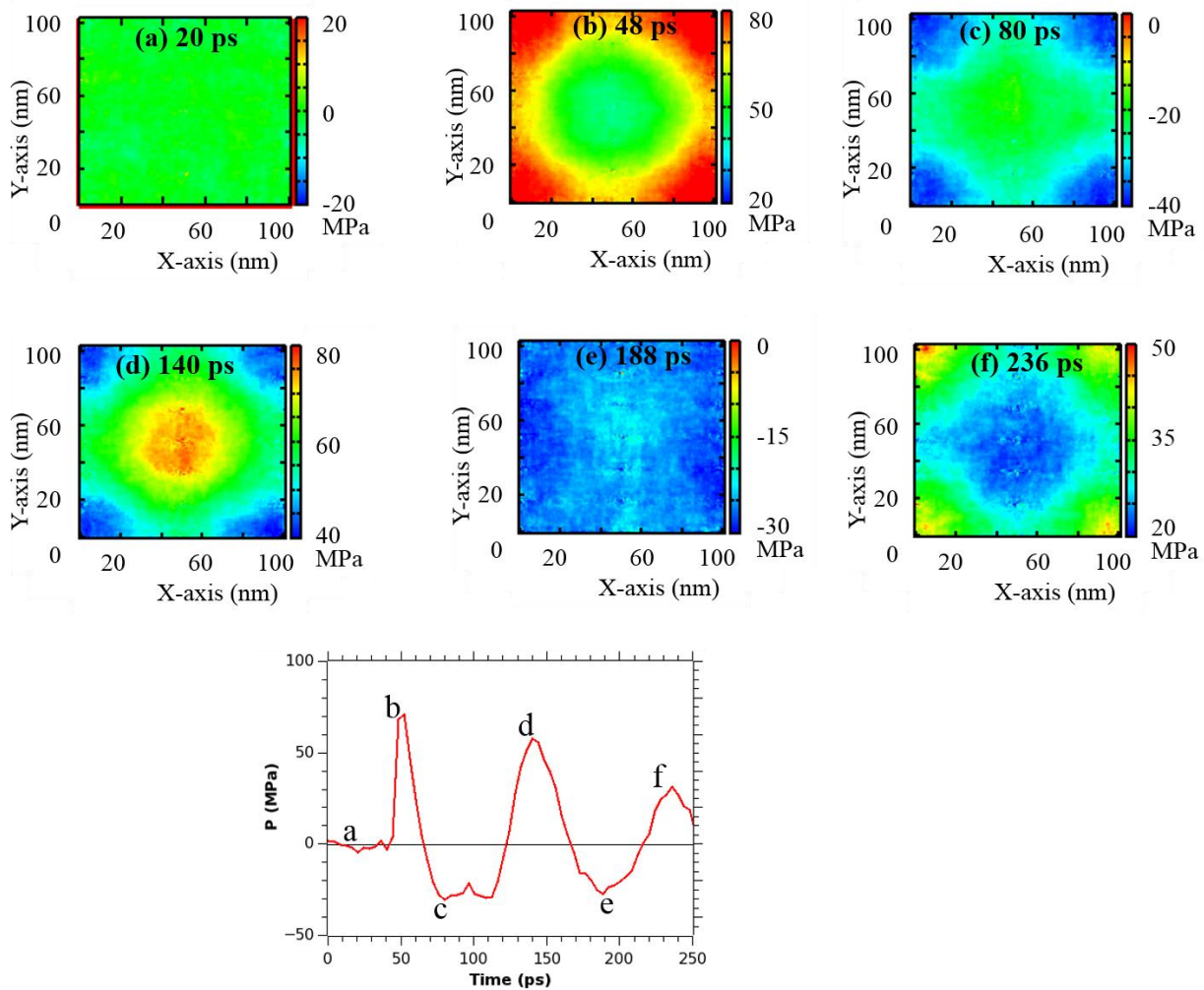


Figure 3.16: 2-dimensional pressure maps calculated at the membrane position at various times for the system containing a nanobubble ($D=60$ nm); $v_p = 0.5$ km/s and $\tau_s = 5$ ps. Range of units (in color) is in MPa. 1-dimensional pressure profile is placed on the bottom. Letters on the 1-d profile refer to same moments of time as on panels with 2-d profiles.

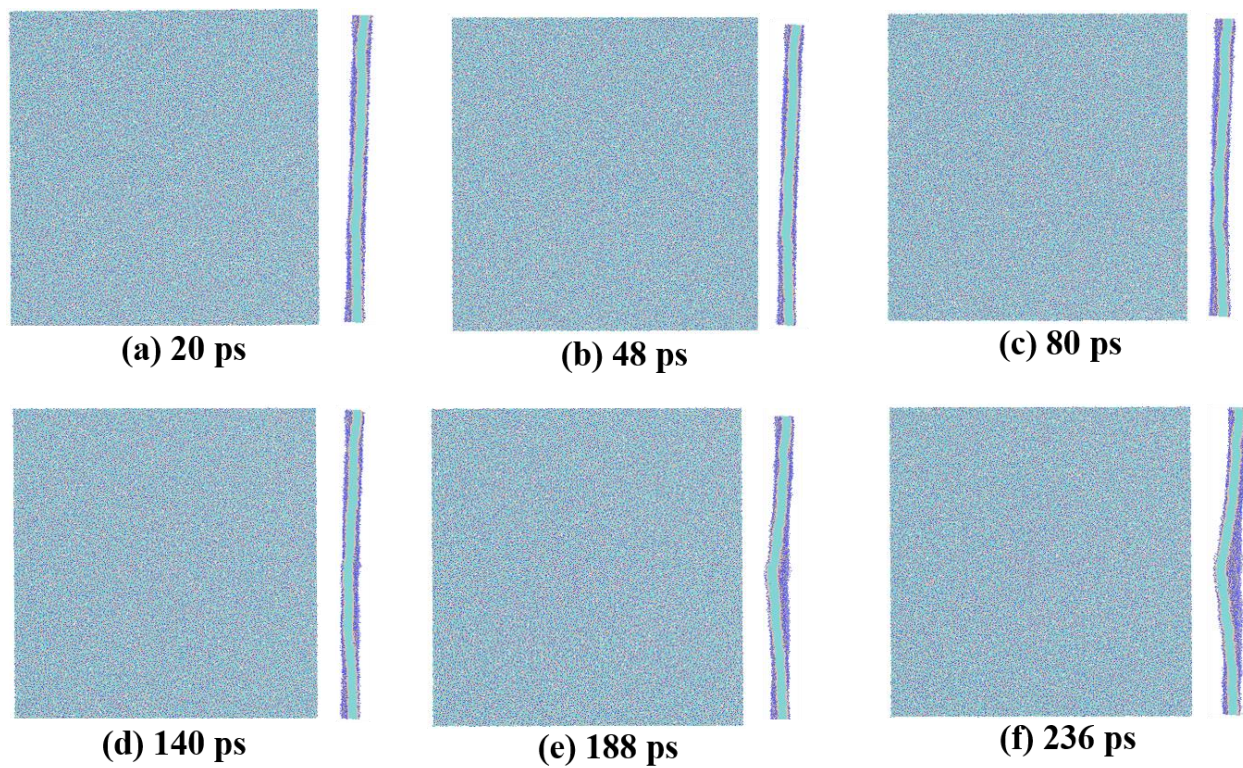


Figure 3.17: Bilayer membrane at various times of the simulation performed on a system containing a nanobubble ($D=60$ nm); $v_p = 0.5$ km/s and $\tau_s = 5$ ps. Top views are on the left and cross sectional views are on the right.

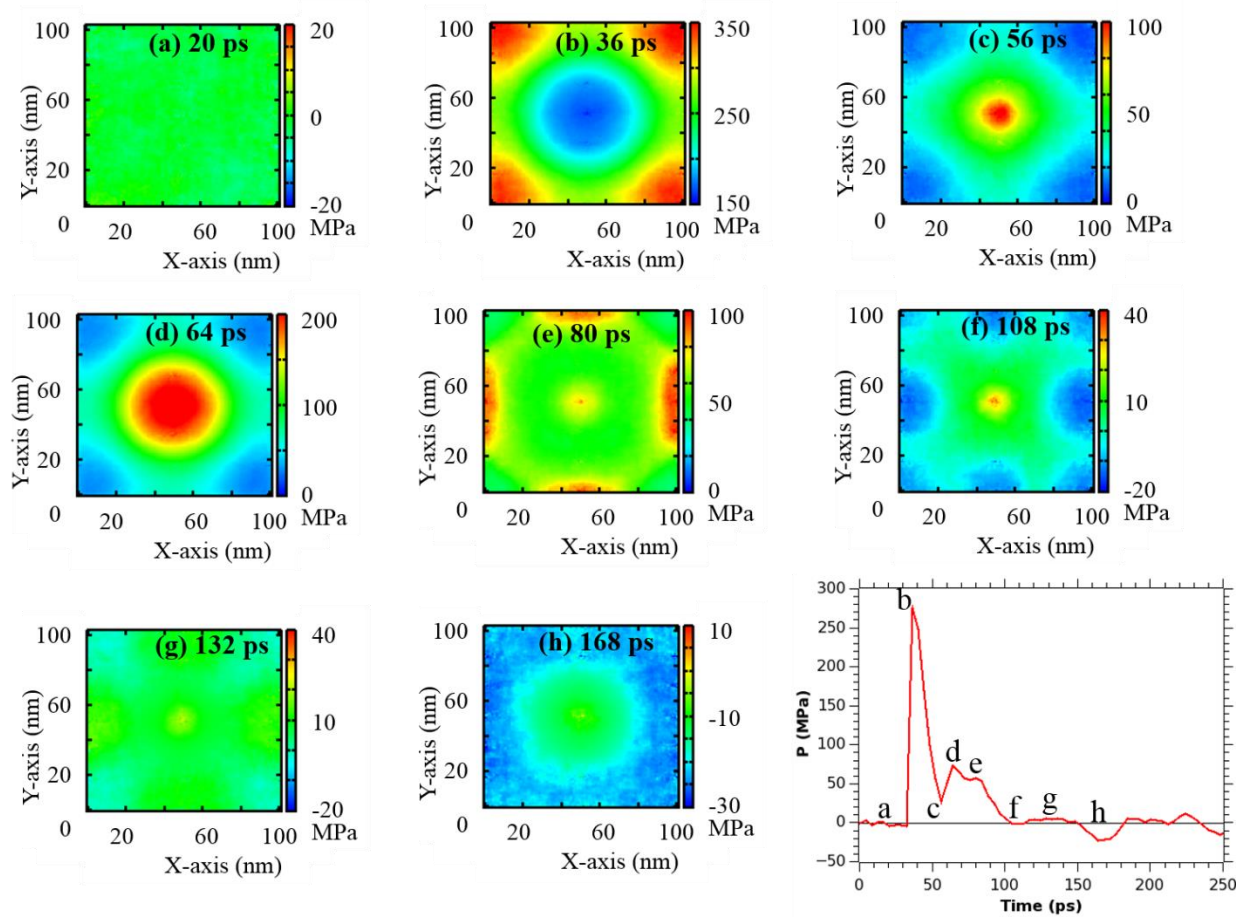


Figure 3.18: 2-dimensional pressure maps calculated at the membrane position at various times for the system containing a nanobubble ($D=60$ nm); $v_p = 0.5$ km/s and $\tau_s = 10$ ps. Range of units (in color) is in MPa. 1-dimensional pressure profile is placed on the bottom right side. Letters on the 1-d profile refer to same moments of time as on panels with 2-d profiles.

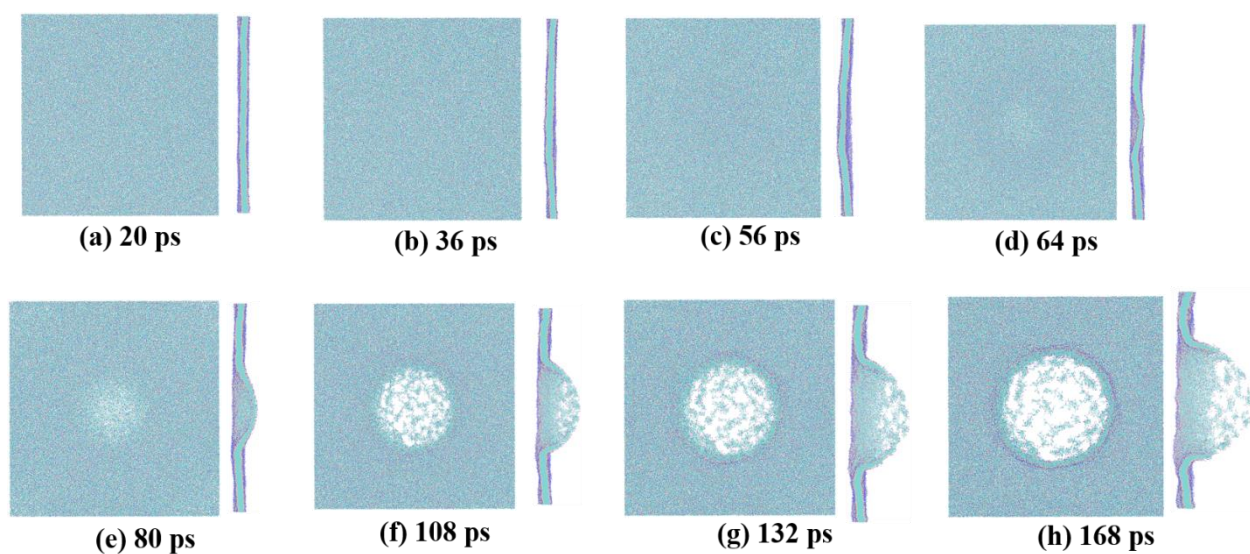


Figure 3.19: Bilayer membrane at various times of the simulation performed on a system containing a nanobubble ($D=60$ nm); $v_p = 0.5$ km/s and $\tau_s = 10$ ps. Top views are on the left and cross sectional views are on the right.

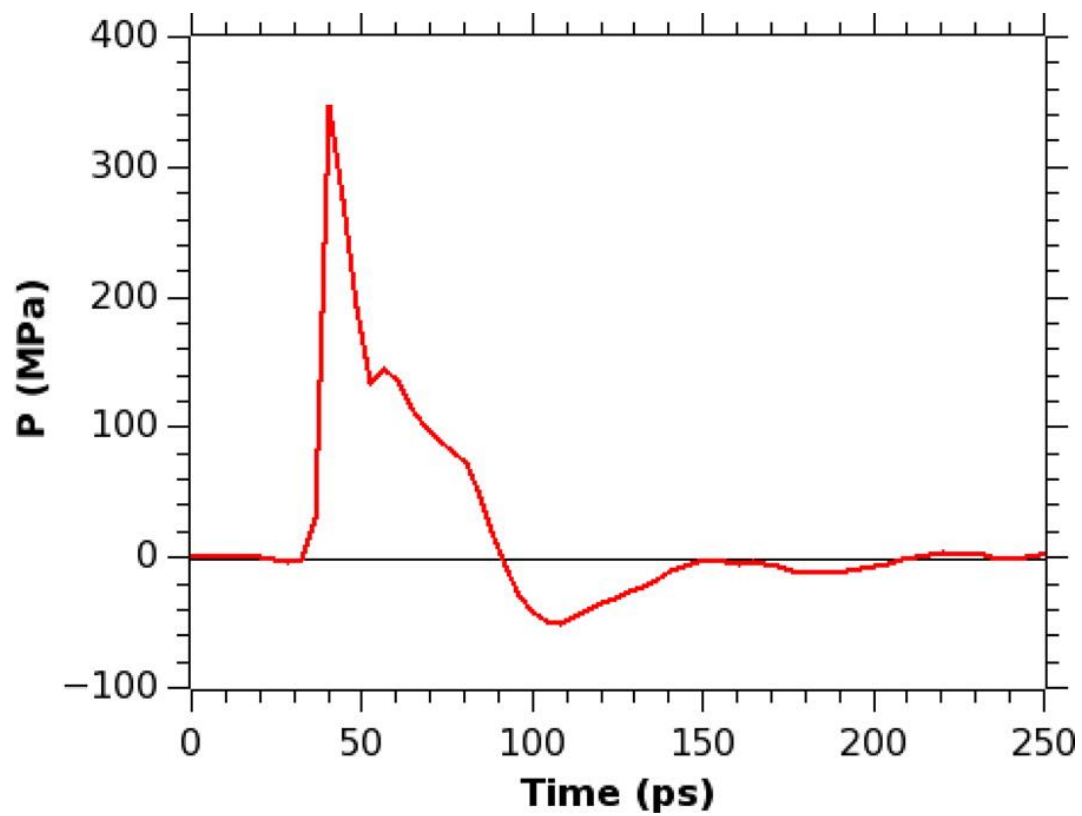


Figure 3.20: Pressure profile at the membrane position in a simulation with $v_p = 1.0$ km/s, $\tau_s = 3$ ps and a nanobubble with a diameter, $D = 20$ nm).

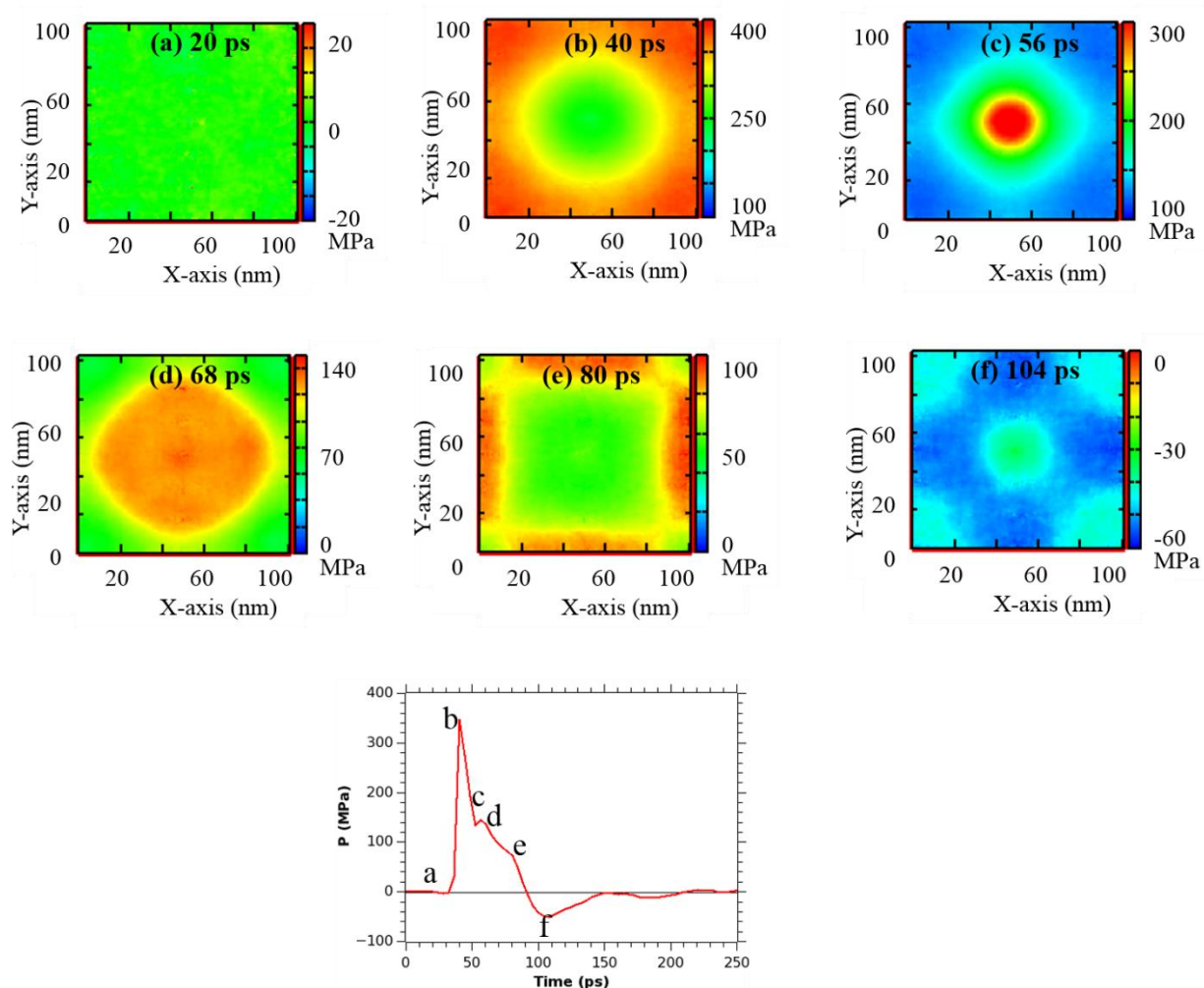


Figure 3.21: 2-dimensional pressure maps calculated at the membrane position at various times for the system containing a nanobubble ($D=20$ nm); $v_p = 1.0$ km/s and $\tau_s = 3$ ps. Range of units (in color) is in MPa. 1-dimensional pressure profile is placed on the bottom. Letters on the 1-d profile refer to same moments of time as on panels with 2-d profiles.

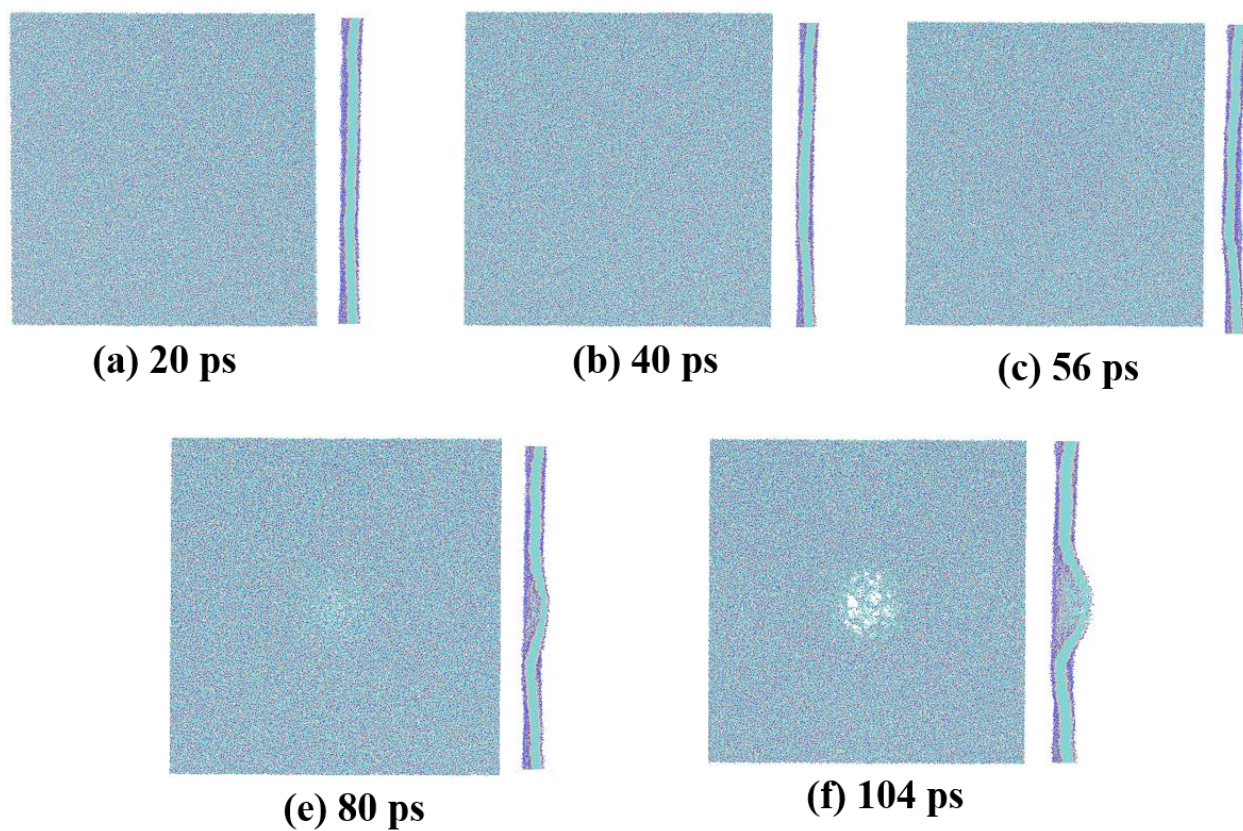


Figure 3.22: Bilayer membrane at various times of the simulation performed on a system containing a nanobubble ($D=20$ nm); $v_p = 1.0$ km/s and $\tau_s = 3$ ps. Top views are on the left and cross sectional views are on the right

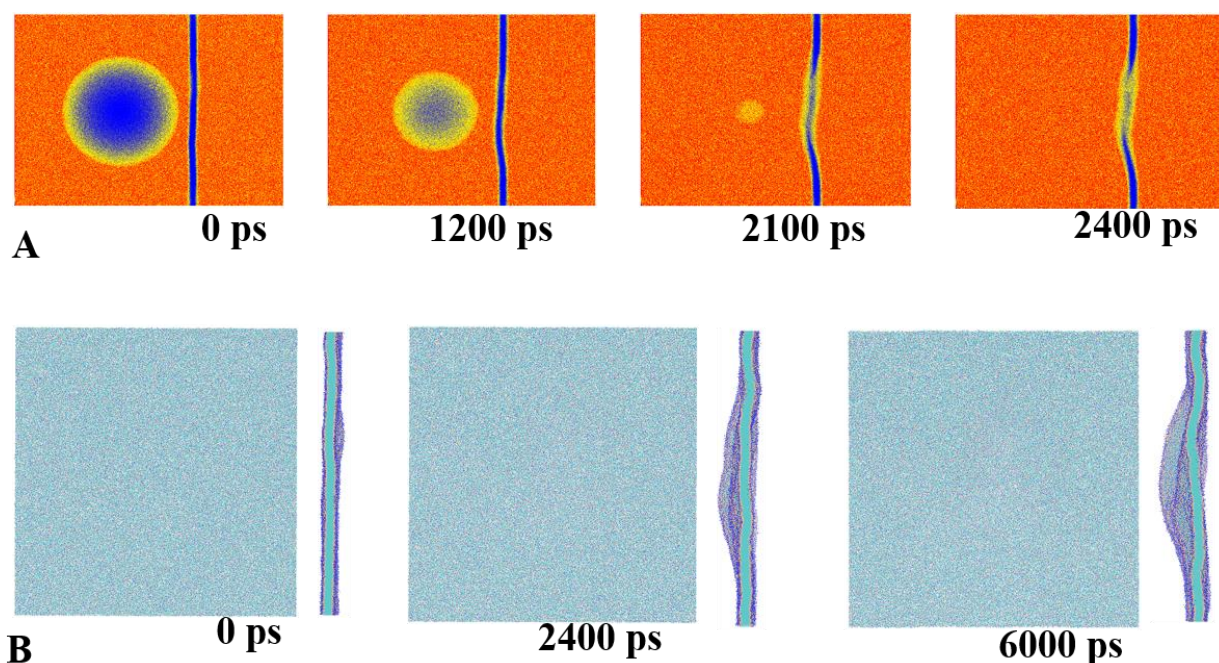


Figure 3.23: Water density and snapshots of membrane. Panel A – 2d water density maps showing the spontaneous collapse of a bubble ($D=60$ nm) in simulations performed using NPT ensemble. Panel B – Snapshots of membrane during the spontaneous bubble collapse at various simulation times.

Chapter 4: Opening of the Blood-Brain Barrier Tight Junction Due to Shock Wave Induced Bubble Collapse: A Molecular Dynamics Simulation Study³

4.1 Introduction

Lately, it was shown that the cavitation effect plays a very important role in the ultrasound assisted drug delivery to specific areas of the human body, including brain areas^{91,113–118}. Delivering drugs to the brain is problematic due to the presence of the blood-brain barrier (BBB), a system that controls the exchange of chemicals between blood and brain regions. Therefore, implosions of microbubbles loaded with drugs, implosions that occur due to cavitation effect induced by the traveling ultrasound, weaken or destroy the BBB, opening the way for drug permeation into the brain. Recently, it was suggested that pressure waves created by blasts, that produce injury in the brain, so-called blast-induced traumatic brain injury (bTBI), may be also connected to damaged BBB^{32,119–125}. Among different reasons that may cause damage to BBB, the cavitation effect (that is present due to implosion of bubbles, microscopic or nanoscopic in size, and created in blood during the passage of shock waves from the blast), was also considered as a possible reason. While some experimental work^{32,119–124} and very recent computational work that used continuum modeling¹²⁵ investigated the connection between bTBI (or TBI in general) and damage to the BBB, no work has yet appeared gearing toward understanding the molecular picture behind this connection.

³ This chapter previously appeared as an article in the ACS Chemical Neuroscience. The original citation is as follows: Goliaei A, Adhikari U, and Berkowitz M L, “Opening of the Blood-Brain Barrier Tight Junction Due to Shock Wave Induced Bubble Collapse: A Molecular Dynamics Simulation Study,” *ACS Chemical Neuroscience* 8, no. 6 (August 2015): 1296.

Computer simulations proved to be a very efficient tool in providing detailed and often molecular detailed pictures of events occurring in biological processes^{126–129}. Detailed simulations describing motion of every atom are used when detailed information is required, for example, to understand such process as a change in the secondary structure of a protein. When the length and time scales of the processes are large in comparison with atomic scales, one can use coarse grained (CG) simulations where, for example, a group of atoms is represented by an effective particle and the interaction between atoms is reduced to interaction between these kinds of effective particles, as it is done in the force field called MARTINI²². Initially constructed to describe model lipid membranes, MARTINI was extended to describe interactions between membranes and proteins,⁷³ often producing a successful nanoscopic description of the processes taking place in these systems¹³⁰. We used MARTINI to study interactions of antimicrobial peptides, such as melittin and/or magainin, with lipid membranes^{50,131,132}. Very recently, we also used MARTINI to study shock wave induced implosions of bubbles situated next to lipid bilayers and the damage to bilayers due to such implosions^{83,100,133}.

In this paper, we report the results from our computational study on how the shock wave induced bubble implosions (cavitation effect) influence the strength of the BBB. Since no previous molecular or even coarse-grained models of BBB are available in the literature, we propose here a first such model. The BBB, as are most of the biological machineries, is quite complicated, especially on a detailed molecular or nanoscopic level. To simulate the BBB damage due to cavitation, our first model needs to be simplified and we concentrated our study on the tight junction (TJ) region between the endothelial cells. In our model, the TJ connecting the gap between two adjacent cell membranes is represented by two pairs of typical TJ proteins, claudins, specifically claudins-15. We chose claudin-15 because its crystal structure was

available¹³⁴ and, more importantly, it is homologously related to claudin-5¹³⁵, which is abundant in brain capillaries¹³⁶. We monitored the degree of the connection between claudin-15 protein pairs when they were exposed to the cavitation effect and observed that bubble implosion plays a crucial role in the serious damage to our model BBB, indicating that the cavitation effect also suspected to exist in the human body after blasts may produce damage and even destroy the BBB, and thus be responsible for the brain damage produced in many blasts, even when they are mild.

4.2 Results and Discussion

We described the interactions between molecules in our systems by using a coarse grained MARTINI force field with improved parameters for proteins⁶⁵ and polarizable water⁶⁶. The improved parameters provide a more realistic description of the proteins and their interactions with lipid bilayers^{65,130}. Since no structure is available for the interacting pair of claudin-15 situated in the extracellular region, we performed long molecular dynamics simulations to get such a structure (see Methods for details). To construct our model of TJ between two cells, we created a large oval shaped vesicle containing DPPC lipids solvated in water (9835 CG DPPC lipid molecules and 727 946 CG polarizable water molecules). On one of the sides of the vesicle, we placed two pairs of interacting claudin-15 proteins. Because of the periodic boundary conditions we use in our simulations, we actually simulate a stack of “cells” (our vesicles) connected through model TJ consisting of two pairs of interacting claudin-15 proteins. Figure 4.1 depicts the stack (panel (A)) containing periodic images of our “cells” and the TJ between them; this picture is reminiscent of a picture of a stack of cells connected by TJ that surround a blood capillary. Panel (B) of Figure 4.1 shows the simulation unit cell containing parts of the membrane with the TJ between them. Following up on the initial preparation step,

we expanded the size of the unit cell of our system in the Y and Z directions by adding CG MARTINI polarizable water. The expansion of number of water molecules to include 3 481 386 CG particles produced a box with sizes $54.0 \times 54.0 \times 144.4 \text{ nm}^3$. This was done with the purpose to incorporate a bubble 30 nm in diameter in the water region located bellow the vesicle. The bubble (nanobubble) was created by removing all water molecules situated in a sphere of diameter 30 nm located in the vicinity of the TJ. The final large-sized unit cell (in some cases containing a bubble, in some without a bubble, to be able to study the effect of a bubble collapse on the integrity of the TJ by comparing results from simulations with and without the bubble collapse) was again equilibrated for another 10 ns, and after this equilibration period our production runs with shock waves impinging on the system were performed. Shock waves were generated by using the momentum mirror approach which was successfully applied in previous simulation work where shock waves were created^{79,83,100,111,112,133}. The procedure we adopted to create shock waves is analogous to having a piston in our system that is moving toward the $+Z$ direction with velocity v_p and reflecting all the particles coming into contact with it. We stopped the piston after a short time (τ_s), and allowed the created shock wave to move in the $+Z$ direction. By doing this, we produced a shock wave impulse traveling toward the TJ. In the present simulations, v_p was 1.5 km/s and we performed simulations with two τ_s values: 2 and 5 ps. The shock wave velocity v_s was calculated in systems containing pure CG polarizable water by measuring the speed of discontinuity in water density profile along the $+Z$ direction. The damage produced by the shock wave on the subject it hits is determined by the shock wave impulse (when no bubbles are present) that is given by the equation $I = \int_0^{t^+} P(t) dt$, where $P(t)$ is the shock wave pressure on the membrane and t^+ is the duration of time it takes for the positive phase of the shock wave to pass⁸⁰. Using the above formula, we calculated the impulse for systems with

no bubbles. The shock wave velocities and impulses for cases when $v_p = 1.5$ km/s and $\tau_s = 2$ and 5 ps are presented in Table 4.1. This table serves as a dictionary that translates values for parameters we use in simulations to parameters describing the shock wave speed and intensity, parameters that are used to report experimental measurements. As we can see from Table 4.1, the shock wave impulse in our simulations corresponds to impulses created by a very mild blast ($I \sim 8.5$ mPa·s when $\tau_s = 2$ ps) and a mild blast ($I \sim 35.6$ mPa·s when $\tau_s = 5$ ps).

The main results from our simulations can be seen depicted in Figures 4.2–5. In the absence of a nanobubble, the passage of a shock wave has a small effect on the interacting pairs of proteins, as can be seen in Figure 4.2. As the figure shows, following the shock passage, the interacting proteins in systems with no bubbles retain their contacts with one another and do not separate from each other. However, in the case of $\tau_s = 5$ ps, upon the collapse of 30 nm in diameter nanobubble caused by the passage of the shock wave, a large change in properties of both vesicle and proteins in our system can be observed in Figure 4.2A. The vesicle parts next to proteins are expanded following the bombardment by high velocity water particles and their shape changes. The proteins completely lose their contacts and pairs become separate entities. On the other hand the effect is less pronounced when $\tau_s = 2$ ps, as shown in Figure 4.2B. Although the proteins in the pair that were hit first (bottom pair in the figure) get separated, the degree of their separation is smaller compared to that in the case with $\tau_s = 5$ ps; the proteins that were hit later (top pair in the figure) still keep their contact. In addition, the vesicle itself has not been changed substantially, as this happened in the case when $\tau_s = 5$ ps. The secondary structure of the proteins also changed as a result of the bubble collapse, as again can be inferred from Figure 4.2. To quantify the change in the secondary structure of our proteins, values for the RMSD from the initial crystal structure were calculated and compared to the values obtained

from simulations with no bubbles being present. Figure 4.3 shows the result of RMSD calculations for simulations performed in this study. Figure 4.3A shows a significant change in RMSD values for the two proteins on the bottom (3 and 4) and a smaller change for the two proteins on the top (1 and 2) when $\tau_s = 5$ ps. Figure 4.3B shows that in the case when $\tau_s = 2$ ps, the values for the RMSD were not that large. The fact that proteins 3 and 4 display large RMSD is expected, since these proteins are closer to the bubble when it collapses and hence they feel a greater force. In comparison, when there is no bubble present, RMSD values do not change significantly in time, as shown by dashed lines in both panels (A) and (B).

To analyze further the effect of bubble collapse on the proteins, the number of contacts between interacting partner proteins was measured. Figure 4.4A indicates that, as expected, when $\tau_s = 5$ ps, the number of contacts between two interacting proteins drops to zero (complete separation) in the presence of the bubble. However, without a bubble present, no significant change in the number of contacts is seen during the 60 ps of shock wave simulation. On the other hand, when the $\tau_s = 2$ ps, as Figure 4.4B shows, only the closest pair to the bubble loses contact completely (black curve), while the top pair (red curve) is still in contact, even after 90 ps of the simulation. An illustration of the structural dynamics of our model of TJ collapse, observed in simulations when the nanobubble was present (and when $\tau_s = 5$ ps), is shown in Figure 5.5. As the simulation progresses, the bubble collapse causes a complete segregation of the two protein pairs and also causes the change in the shape of the lipid vesicle, that gets elongated in the direction of the shock wave propagation.

4.3 Conclusion

Our computer simulations reported here were performed to study the effect of nanobubble collapse that, as it is suggested, can occur in blood capillaries after passage of the blast induced shock waves. It was also suggested that this collapse may cause damage to, or even destruction of, the BBB by damaging (destroying) the TJ between the BBB cells^{114,125}. In our simulations we considered model systems with the TJ containing two pairs of the TJ protein, claudin-15. When no bubble was present in the system, we did not observe any damage done to the TJ upon passage of the shock wave. In cases when bubbles of 30 nm in diameter were present in the system, their collapse under the influence of a very mild shock wave with an impulse of $\sim 8 \text{ mPa}\cdot\text{s}$ produced some small amount of damage to the TJ. When the impulse of the shock wave was more than 4 times larger (but still remained mild in relative values, if compared with the impulse of $54 \text{ Pa}\cdot\text{s}$ observed in experiment when no damage to cell was done⁸⁰), our model TJ was destroyed. Although our simulations were performed on relatively simple systems, they show the crucial role played by the presence of nanobubbles and the cavitation effect in causing severe damage to cell membranes and also proteins embedded in the cell membranes.

4.4 Methods

Our molecular dynamics simulations were performed using Gromacs 4.6.6 package^{67,107–109}. The initial structure of the protein in our study was the available crystal structure of claudin-15¹³⁴ (PDB ID: 4P79). To coarse grain the protein, the martinize.py script⁶⁵, downloaded from the MARTINI force field website, was used. Cysteine residues 47 and 57 were linked together to emulate disulfide bonds in the extracellular region number one (ECL1). The claudin-15 protein

carries a net negative charge of -1 , and therefore, we also placed sodium ions (Na^+) into the system in numbers that were needed to neutralize the system.

The structure of the interacting pair of claudin-15 situated in the extracellular (ECL) region was obtained by performing long molecular dynamics simulations. Initially, one protein was inserted in a cylindrical pore created in the center of a DPPC (1,2-dipalmitoyl-*sn*-glycero-3-phosphocholine) bilayer containing a patch of 150 lipids. This bilayer together with the embedded protein was then replicated, rotated, and translated to the top of the first system so that the two ECL regions of each protein were in water facing each other, but not in contact with each other. This new system (a double bilayer with one protein in each bilayer) was then energy minimized, and a 1 μs molecular dynamics run was performed. During this run, the two proteins found each other and made a head-to-head contact after ~ 100 ns. This contact was stable throughout the rest of the simulation, so we used the created claudin-15 pair as a model of our interacting proteins in the TJ. The 1 μs simulation was done using the NPT ensemble, with temperature kept at 320 K and pressure at 1.0 bar (semi-isotropic coupling) using the Berendsen coupling scheme⁶⁸. The time constants for temperature and pressure coupling were 1 and 2 ps, respectively. Compressibility value for the pressure coupling was set to $3 \times 10^{-4} \text{ bar}^{-1}$. The Lennard–Jones interaction cutoff value of 1.2 nm was used, and the “shift” scheme with a cutoff of 1.2 nm was applied for the electrostatics. The dielectric constant was set to 2.5, and the time step for the integration was 20 fs. The final box size was $X = 7.25$, $Y = 7.25$, and $Z = 17.9$ nm.

Since the goal of our simulations is to study how the proteins of TJ region respond to cavitation during the blast, it is important to have the correct density in our system. Therefore, prior to performing shock wave simulations, we continued the preparation of the system without the bubbles and equilibrated it for 100 ns using the NVT ensemble. To create the shock wave, we

used the mirror approach when all the particles in the system move with certain velocity v_p toward the mirror placed at the end of the box in the $-Z$ direction. The particles get reflected upon impact with the mirror, thus creating a shock wave with velocity v_s larger than v_p and moving in the $+Z$ direction. A 2 nm vacuum layer was added at the end of the $-Z$ direction to avoid the immediate contact between the particles and the mirror at the beginning of the simulation. All shock simulations were performed in the constant energy ensemble with the periodic boundary condition (PBC) turned off in the Z -direction. The time step of 4 fs was used. The cutoff value for the nonbonded interactions was 1.4 nm instead of the usual 1.2 nm, and the neighbors list was updated every 5 steps, instead of the usual 10. Each simulation with $\tau_s = 2$ ps was performed for 90 ps and with $\tau_s = 5$ ps for 60 ps, to make sure the shock front moved across the simulation box and exited on the end opposite from where it initiated. Since shock wave simulations were short in their duration, we performed a number of them, with different initial velocities, but corresponding to the same temperature. All the results were very similar for simulations done with the same value of τ_s . We presented here the results from one typical simulation in each case.

The pressure calculation was done using Gromacs-4.0.2_local pressure⁷⁷ version of Gromacs following the method developed by Ollila et al⁷⁷. The dimension of the small cubes when discretizing the system was set to 0.5 nm.

To study the integrity of the protein pair in its contact, we analyzed the number of contact points between the pair using the Plumed 2.1 plug-in¹³⁷. More specifically, we calculated how many atoms from the first protein are found at a certain distance (1 nm in our case) from the second protein of the same pair. The calculated value was considered as the number of contacts between the two interacting proteins in our study.

Table 4.1. Impulse and velocity of the shock wave at the time when it hits the bilayer for different piston stopping time (τ_s).

τ_s (ps)	Impulse (I); mPa*s	Shock velocity (v^s); km/s
2	8.44	2.27
5	35.59	3.11

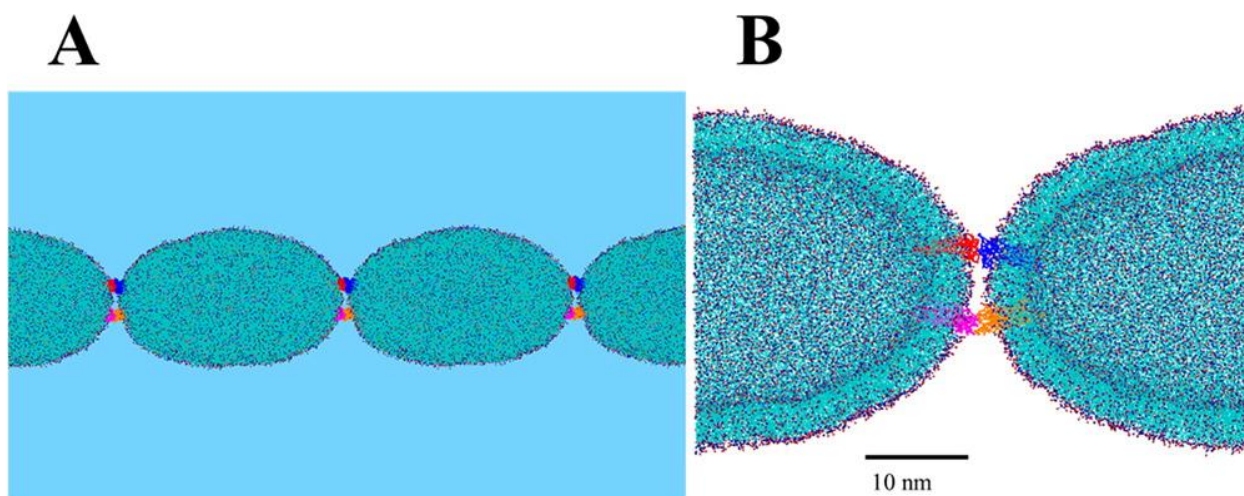


Figure 4.1: Initial configuration of the model TJ. (A) Simulation box (with no bubble present) periodically repeated in the $-X$ and $+X$ directions. Blue background represents water. (B) TJ part in the simulation box where more emphasis on the two pairs of proteins is highlighted. Each one of the interacting claudin-15 molecules is color coded to show the interacting partner.

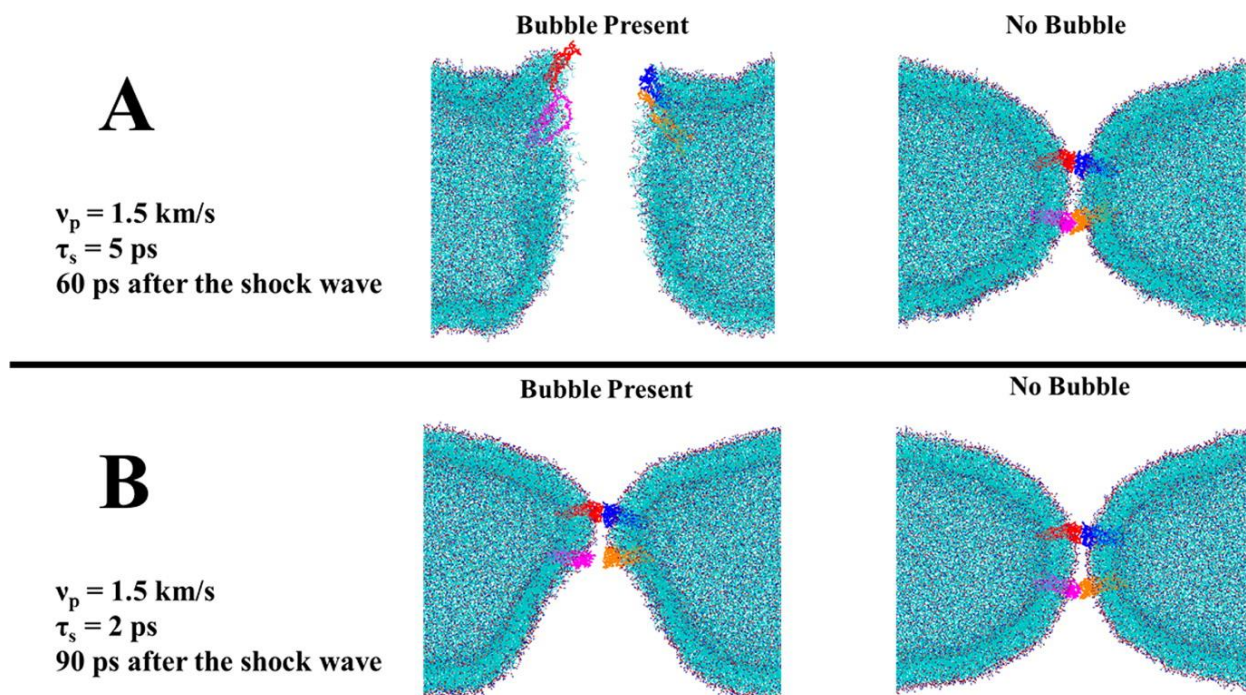


Figure 4.2: Shock wave simulations with and without a nanobubble. The figure shows the configuration of the vesicle and protein pairs after shock. Snapshot from the simulation (A) when $\tau_s = 5 \text{ ps}$ and (B) when $\tau_s = 2 \text{ ps}$. In each panel, the resulting configuration when no bubble is present is on the right, whereas the case when the bubble is present is on the left.

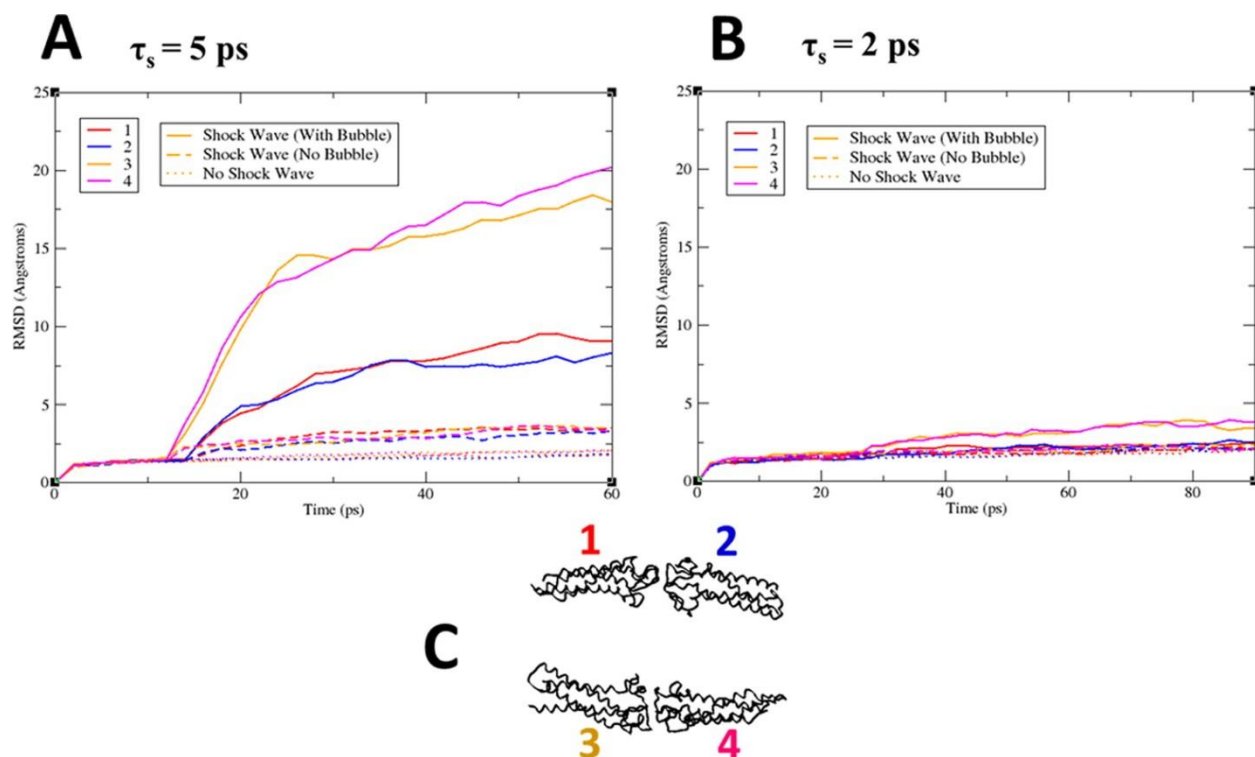


Figure 4.3: RMSD curves for each of the claudin-15 proteins. (A) Change of RMSD values over 60 ps shock wave simulation, when $\tau_s = 5$ ps. (B) Change of RMSD over 90 ps of simulation when $\tau_s = 2$ ps. Each graph is colored and corresponds to the numbered proteins shown in (C). RMSD values for simulation with the presence of bubble are represented by solid lines. Lines for results from shock wave simulation without bubbles are shown as dashed lines. As a control, simulations with no shock waves were also performed and the RMSD values were measured. They are presented in the graphs as dotted lines.

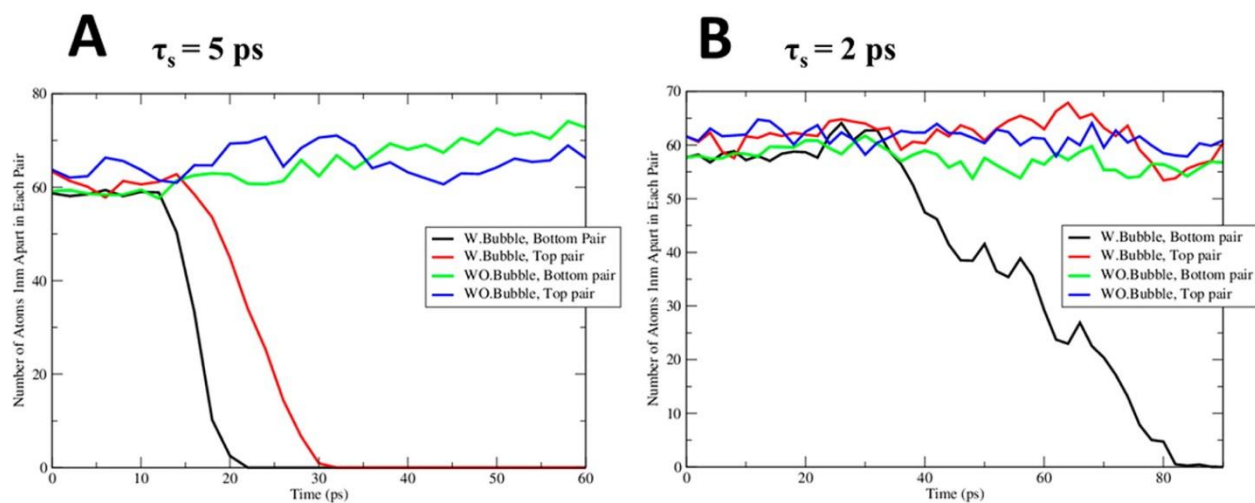


Figure 4.4: Number of contacts between interacting protein pairs. (A) Change in the number of contacts between interacting pairs during 60 ps of shock wave simulation when $\tau_s = 5$ ps. (B) Change in contact number during 90 ps of simulation when $\tau_s = 2$ ps. Black and red curves represent cases when a bubble is present, while green and blue lines represent cases when there is no bubble.

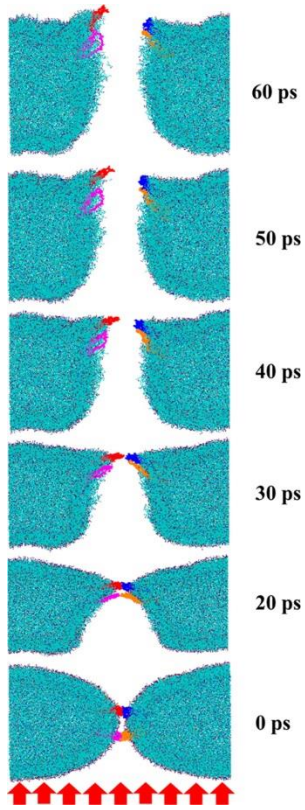


Figure 4.5: Overall progress of the simulation during the 60 ps shock wave propagation in a system when a 30 nm bubble is present and when $\tau_s = 5$ ps. The frames are in the direction of increasing time when observed from the bottom-up. Red arrows at the bottom indicate the direction of the shock wave propagation.

Chapter 5: Properties of Poloxamer Molecules and Poloxamer Micelles Dissolved in Water and Next to Lipid Bilayers: Results from Computer Simulations⁴

5.1 Introduction

Poloxamers are a class of triblock copolymers with the central hydrophobic group flanked by hydrophilic groups on both sides. The hydrophobic block consists of a chain of poly(propylene oxide) (PPO) units, whereas the hydrophilic block is made of poly(ethylene oxide) (PEO) units. The structural formula for poloxamer is therefore PEO–PPO–PEO, and the copolymer has an amphiphilic character. Poloxamers are found in both liquid and solid forms, and their molecular mass can reach values of up to several thousand daltons. One can vary the PEO and PPO chain lengths and produce poloxamers with a variety of properties and functions. Because of their nontoxic nature and high solubility in water they are widely used to facilitate gene/drug delivery, as emulsifying agents, or as agents helping in healing damaged cell membranes^{36–40}.

One of the widely studied poloxamers is a molecule called P85. This molecule is believed to decrease the multidrug resistance (MDR) in cells⁴¹ by inhibiting the activity of the transporter proteins like *p*-glycoproteins by producing changes in lipid environment around the proteins. P85 poloxamers might also be responsible for the conformational changes of membrane proteins. In addition, they also translocate through the cancer cell membrane and affect that cell's

⁴ This chapter previously appeared as an article in the Journal of Physical Chemistry B. The original citation is as follows: Adhikari U, Goliaei A, Tsereteli L, and Berkowitz M L, "Properties of Poloxamer Molecules and Poloxamer Micelles Dissolved in Water and Next to Lipid Bilayers: Results from Computer Simulations," *Journal of Physical Chemistry B* 26, no. 120 (July 2016): 5823.

metabolism. Therefore, micelles consisting of P85 molecules are used to deliver drugs to cancer cells^{37,138}.

Another poloxamer of great interest is P188, which is already commercially used in medical applications, especially in the healing of burned or damaged skin^{42,139–142}. It is believed that P188 inserts inside the damaged bilayer membrane, helping to restore the membrane integrity, and is squeezed out from the membrane once the membrane is healed^{141,143,144}.

Although understanding the nature of interaction between poloxamers and lipid membranes is very important for the effective use of these polymers in biological systems, it is hard to perform experimental investigations that would provide a detailed molecular level picture of these interactions. Therefore, molecular dynamics simulation technique is emerging as one of the best tools to get such a picture. Nevertheless, as of today, there are only a few reports^{145,146} in the literature describing simulations performed to study the interaction of poloxamers with lipid membranes.

Often the time scale and length scale involved in the study of systems containing polymers and lipid membranes are larger than the ones that can be covered by simulations using all-atom or united atom force fields. Most of the time in these situations one uses coarse-grained (CG) force fields that reduce the number of degrees of freedom and accelerate the dynamics of the system, leaving most of the structural and thermodynamics information intact. Thus, parameters for the CG force field describing polyethylene and polypropylene¹⁴⁷, polyethylene glycol and polyoxyethylene alkyl ethers¹⁴⁸, and also PEO and PPO chains¹⁴⁹ are reported in the literature. CG force-field parameters for poloxamers are also reported in the literature^{146,150,151}. For example, the MARTINI CG force field was extended recently to include a 3-to-1 mapping of

PEO and a 4-to-1 mapping of PPO chains¹⁴⁶. This extended force field was used to describe the interaction between poloxamers and membranes containing DMPC lipid molecules.

All previous coarse-grained simulations performed on systems with poloxamers, in the presence or absence of lipid membranes, were performed using nonpolarizable MARTINI water, which does not consider the effect of water polarization. The inclusion of polarization plays an important role in the description of interactions between systems containing charged or polar molecules immersed in water⁶⁶. Although poloxamers are electrically neutral, they contain polar groups and their interactions across water with membranes containing lipids with polar or charged groups and also proteins with polar or charged residues strongly depend on the correct description of coarse-grained water-like particles. Therefore, we performed present simulations, described in this paper, using a polarizable water particle from the CG MARTINI force field⁶⁶. Because the previously developed MARTINI-type CG force field for poloxamers was used in simulations with nonpolarizable MARTINI water¹⁴⁶ we adjusted the poloxamer beads interactions with other beads in the system (see Methods).

An important property of poloxamers is their ability to form micelles^{152–156}. The number of molecules in the micelle, known as the aggregation number, depends on the type of the molecule and the temperature¹⁵⁷. Poloxamer micelles are found to be very important in the drug-delivery process. Nevertheless, no simulations have been performed yet to study the poloxamer micelle–membrane interaction. In view of the importance of both shorter-sized poloxamers, such as P85, and also longer-sized, such as P188, we studied the interaction of both P85 micelles and P188 micelles with the DMPC membrane. We also studied the interaction of P188 micelle with a bilayer containing a pore to investigate the sealing ability of this micelle.

5.2 Methods

5.2.1 Coarse-Grained Force Field

The parameters for the CG force field describing water and lipids in our simulations were taken from the MARTINI^{22,65,66,73,130} force field with polarizable water. To describe poloxamers, we followed the same mapping procedure and adopted the same bonded interactions parameters as was done in ref ¹⁴⁶. Thus, 3-to-1 and 4-to-1 mapping was applied for PEO and PPO, respectively. To take into account that water particles are represented as polarizable MARTINI water, we adjusted the parameters describing the potential strength (ϵ) of the Lennard-Jones (LJ) nonbonded interactions of PEO and PPO with themselves, with the polarizable water, and with the coarse-grained lipid beads. The adjustment was performed by using a trial procedure. We tested the validity of our modified force field in simulations containing either one poloxamer molecule dissolved in water or a micelle containing poloxamer molecules, also dissolved in water. In both types of systems we compared the calculated from the simulations radii of gyration with the radii measured in experiment. The new nonbonded LJ parameters ϵ we used in our simulations for the various interbead interactions are given in Table 5.1. The rest of the force-field description and parameters can be found in ref ¹⁴⁶.

5.2.2 Setup of Molecular Dynamics (MD) Runs

We performed all molecular dynamics simulations using Gromacs 4.6.6 package^{67,107–109}. Most of the simulations were performed in the NPT ensemble, although simulations of systems containing pores in membranes were done using NP _{ϵ} AT ensemble because pores are unstable when the NPT ensemble is used. The temperature 293 K was kept constant for systems with a single poloxamer, and 320 K was kept constant for systems containing micelles and the

membrane; we used the velocity-rescaling scheme¹⁵⁸ to keep the temperature constant. The pressure was set at 1 bar (isotropic for poloxamer simulations and semi-isotropic for systems containing the membrane) by using the Parrinello–Rahman pressure coupling scheme^{159,160}. Time constants for temperature and pressure couplings were taken to be 1 and 12 ps, respectively. Pressure compressibility was set to 3×10^{-4} bar. The Lennard-Jones interaction cutoff was set to 1.2 nm using the shift scheme, and the dielectric constant was set to a value of 2.5. The time step was 20 fs in all simulations. Before our production MD runs were performed, all systems were energy minimized.

5.2.3 Simulations of Poloxamers in Bulk water

We considered two different poloxamers, P85 and P188, because they have different sizes of PEO and PPO units. The former has a shorter PEO block (26 monomers) and a longer PPO block (40 monomers), whereas the latter one has a longer PEO block (80 monomers) and a shorter PPO block (27 monomers).

To calculate the radius of gyration, R_g , of a single P85 poloxamer, we simulated a cubic unit cell with a size of 8.5 nm in each direction that contained a poloxamer molecule solvated by 5284 polarizable water particles. In the case of P188 poloxamer a bigger cubic unit cell with a size of 13 nm in each direction was used. In this case the poloxamer was solvated by 18 203 polarizable water particles. In both cases molecular dynamics simulation was performed for 1 μ s.

On the basis of the experimental result¹⁵³ we chose the aggregation number of P85 micelle to be 60 at 320 K. The aggregation number for P188 was chosen as 21^{154,161}. Because the self-assembly of these poloxamers into micelles starting from a random configuration of poloxamers can take a very long time, we constructed our micelles using the following

procedures: (a) For P85, four sets of 15 poloxamers were allowed to self-assemble, each forming a micelle. After that, four of these micelles, each containing 15 poloxamers, were placed close to each other and an MD simulation was performed until a stable micelle containing 60 P85 poloxamers was formed. (b) Similarly, for the P188 micelle formation, initially three sets of seven P188 molecules were allowed to self-assemble. After that these micelles were placed close to each other to assemble into a big micelle containing 21 P188 molecules. In both cases, the final step in the micelle preparation was run for 200 ns. Upon the completion of stable micelle preparation, each micelle was immersed into a cubic box with the size of ~ 29 nm containing $\sim 200\,000$ polarizable water molecules. The simulation runs containing micelles were performed for 1 μ s in the NPT ensemble.

5.2.4 Simulations of Poloxamers in the Presence of a Bilayer Membrane

A single poloxamer was allowed to interact with a lipid bilayer containing 288 (144 in each leaflet) 1,2-dimyristoyl-*sn*-glycero-3-phosphocholine (DMPC) lipids. The DMPC bilayer was initially constructed using insane.py¹⁶² script. MD simulation was run for 1 μ s to observe the various stages of interaction between a single poloxamer and the DMPC bilayer. The final unit cell size for the P85-DMPC system was $9 \times 9 \times 13$ nm³, and it contained 6873 polarizable water particles, whereas in the case of P188 poloxamer the cell size was $9 \times 9 \times 17$ nm³ and it contained 10 637 polarizable water particles. Micelles were allowed to interact with a comparatively bigger DMPC bilayer containing 1568 lipids (784 in each leaflet). The final cell size for this simulation was $\sim 22 \times 22 \times 30$ nm³ containing $\sim 108\,000$ polarizable water particles. These simulations were run for 5 μ s.

5.2.5 Simulations of Poloxamer Micelles in the Presence of a Bilayer Membrane Containing a Pore

A DMPC bilayer with a pore was created using insane.py script¹⁶². The bilayer was made up of 1424 lipids and the pore size was ~ 7 nm in diameter. The size of the simulation cell was $22 \times 22 \times 32$ nm³ containing 121 879 water particles. A micelle containing P188 poloxamers was placed on the top of the pore. The MD simulation was performed for 1 μ s.

5.3 Results and Discussion

5.3.1 Radii of Gyration (R_g)

We present the instantaneous values of R_g as a function of time during 1 μ s of the simulation run in Figures 5.1 and 5.2. The time average R_g for P85 is 2.16 ± 0.36 nm. This value is in a good agreement with the experimental value of ~ 1.95 nm¹⁵³ and the value of ~ 2.2 obtained in simulations with a nonpolarizable water¹⁴⁶. The value of R_g for the P85 micelle (aggregation number = 60) at 320 K is 4.61 ± 0.11 nm, which is also close to the experimental value of ~ 4.7 nm¹⁵³. From Figure 5.1 we observe that R_g fluctuates in time and the value of fluctuations for a single P85 is relatively large, while it is small for the micelle. Figure 5.1 also indicates that fluctuations in the shape of P85 micelle may have a low-frequency component. From the data shown in Figure 5.2 we found that R_g of a single P188 poloxamer at 293 K is 4.10 ± 0.87 nm. The experimental value of the hydrodynamic radius of P188 at 293 K is reported to be ~ 2.5 nm¹⁵⁴. This is consistent with the observation that a radius of gyration of a nonspherical system (like a P188 molecule) is usually larger than the hydrodynamic radius¹⁶³. Our calculated value of R_g is also larger than the experimental value of $R_g = 3.1$ nm for a similar F68 poloxamer¹⁵⁶ containing two blocks of PEO, each with 75 units and a block of 30 units of PPO.

The R_g value of the P188 micelle (aggregation number = 21) at 293 K is found to be 6.74 ± 0.20 nm. This value is close to the hydrodynamic radius of P188 micelle at 320 K (~ 7 nm)¹⁵⁴.

Because for spherical micelles the radius of gyration and the hydrodynamic radius are comparable, the result from our simulation is consistent with the experimental result. Snapshots from our simulations of micelles in water are shown in Figure 5.3.

The shape of a micelle can be examined by calculating the eccentricity (ϵ), defined as

$$\epsilon = 1 - \frac{I_{min}}{I_{avg}}$$

where I_{min} is the smallest moment of inertia and I_{avg} is the average moment of inertia. If I_{min}/I_{avg} is equal to 1, the micelle is spherical, whereas the value smaller than 1 indicates ellipsoidal shape^{164–166}. We find that both of our P85 and P188 micelles are not perfectly spherical, although the P85 micelle is close to being spherical, having a I_{min}/I_{avg} value of 0.90 (0.85 for the central hydrophobic PPO core). As one can see from the structure shown in Figure 5.3, P188 micelle is much less spherical. Indeed the I_{min}/I_{avg} ratio for this micelle is equal to 0.73, and it has a really small value of 0.37 for the rod like hydrophobic PPO core. This smaller value of I_{min}/I_{avg} for the P188 micelle is partly due to the presence of long PEO chains floating in water, which constantly move away and come back to the center of the micelle. The time dependence of the eccentricities of P85 and P188 micelles during 1 μ s simulation run is shown in Figure 5.4, indicating that the shape of the micelles remains nearly the same during the run.

5.3.2 Interaction of Poloxamers with Membrane

To study the interaction of a P85 poloxamer molecule with a lipid bilayer, we placed one P85 molecule in close proximity to the bilayer containing DMPC lipids. Snapshots showing

different stages of the simulation are presented in Figure 5.5. We observed that after a short time period (~ 10 ns) the hydrophilic PEO parts of the poloxamer quickly got engaged in the interaction with the headgroup region of the bilayer. As the PEO groups kept interacting with the lipid headgroups, the PPO region kept floating in the water. This continued for ~ 100 ns, after which the PPO block found a path to cross the hydrophilic barrier formed by the lipid headgroups. As one can see from the snapshots in Figure 5.5, it takes ~ 1 ns for the complete insertion of PPO block into the hydrophobic region of the bilayer. We continued the simulation for $5\text{ }\mu\text{s}$ and observed that the PPO block, when inserted into the hydrophobic region of the membrane, remained there, while the PEO blocks kept interacting with the lipid headgroups and nearby water particles.

We observed similar results from the simulation of the system where we studied the interaction of the P188 poloxamer with the DMPC bilayer (see snapshots in Figure 5.6). The insertion of the PPO chain also occurred after a time period of order ~ 100 ns, and again it took a very short time period (~ 1 ns) for the complete insertion of the PPO into the hydrophobic part of the membrane. Similarly, the simulation performed up to $5\text{ }\mu\text{s}$ showed that PPO block stayed inside the hydrophobic core of the bilayer, while PEO blocks were interacting with the lipid headgroups and with water. Density profiles that describe the locations of the bilayer headgroups and poloxamers blocks are shown in Figure 5.7, in panel A for P85 and in panel B for P188. These plots confirm that PPO block spends most of its time inside the hydrophobic core of the bilayer, whereas PEO blocks mostly stay in the hydrophilic region of the bilayer.

5.3.3 Interaction of Poloxamer Micelles with the DMPC Bilayer

To study the interaction between a P85 poloxamer micelle with a lipid bilayer, we placed a previously prepared micelle containing 60 P85 molecules in a close proximity to a DMPC bilayer containing 1568 lipids (see the snapshot on the left of Figure 5.8). As the simulations proceeded, half of the PEO chains of poloxamers got engaged in the interaction with the lipid headgroups, but during the time period of 1 μ s only one of the P85 molecules got inserted inside the hydrophobic core of the bilayer. The bilayer curved substantially, as the snapshot from Figure 5.8 shows, but the barrier formed by the hydrophilic lipid headgroups was strong enough to keep the micelle out of the bilayer. Continuation of the simulation for another 5 μ s resulted in the insertion of only one more P85 molecule into the bilayer, while the micelle lost its spherical shape and spread on the surface of the bilayer (see the right panel of Figure 5.8).

Basically similar in general, but slightly different in detail results were obtained in case of P188 micelle. When this micelle was placed near the membrane, almost all of the PEO chains got engaged in the interaction with the hydrophilic lipid headgroups. Unlike in case of P85 micelle, we did not observe any significant curving of the bilayer or insertion of the poloxamer molecule into the bilayer within 1 μ s of simulation. After the simulation run was performed for 5 μ s, only one P188 molecule got inserted inside the bilayer. Figure 5.9 shows some snapshots from the simulation of P188 micelle with the DMPC bilayer.

5.3.4 Does the P188 Micelle Seal the Pores in the Membrane?

P188 poloxamer molecules are widely used as membrane sealants and, as observed in the experiments, they help to heal the damage caused to the membrane by closing pores in them^{39,40,42}. Despite the fact that it is important to understand the molecular detailed picture of

the pore closure assisted by the P188 poloxamer, experiments did not provide such a picture, and we hope that computer simulations can help in this case also. Our present simulation showed (see Figure 5.3) that after a 1 μ s run the hydrophobic part that is the core of the P188 micelle forms a rod-like structure with length and width of ~ 6 and ~ 3 nm, respectively, although the overall structure of the micelle had a more spherical shape. It was also noted in the literature¹⁵³ that at higher temperature there is a possibility of formation of cylindrical and lamellar types of micelles.

It is known^{130,167,168} that MARTINI force field does not reproduce membrane pore closure event in simulations that are performed in the NPT ensemble. Therefore, to study pore closure and still use MARTINI, we used the NP_zAT ensemble. In separate simulations containing a bilayer and a pore of ~ 7 nm in diameter, we observed that the pore closed in few nanoseconds, if we used NPT ensemble, and stayed open during a 250 ns run, when NP_zAT ensemble was used. To study the interaction between the membrane with a pore and the P188 micelle, we prepared a system containing a bilayer with a pore of size ~ 7 nm diameter and placed a P188 micelle above the membrane on top of the pore. The snapshots of the system in various stages of the simulation can be seen in Figure 5.10. At the beginning of the run, the PEO blocks of the micelles started to interact with the lipid headgroups, and within 50 ns of the simulation the hydrophobic PPO core of the micelle reached the membrane pore. At this moment the PPO core of the micelle began entering the hydrophobic lipid bilayer through the edge of the pore. Because the pore usually has a toroidal shape, the density of hydrophilic headgroups near the pore edge is reduced. This facilitated the reduction of the barrier for the permeation of the micellar hydrophobic core. At the same time the interaction between the hydrophilic PEO chains with the lipid headgroups located at the edge of the pore also might facilitate the permeation of the micellar core by pulling the

lipid headgroups from the edge toward the rest of lipid headgroups. As the simulation continued, the PPO core of the micelle continued its permeation into the membrane, and ultimately the pore closed before the simulation reached 250 ns. We continued the simulation up to 1 μ s and observed that all of the hydrophobic PPO chains previously located in the core of the micelle spread out into the bilayer's hydrophobic part and the pore closed completely.

5.4 Summary

In this work, we used MARTINI force field to study the behavior of two poloxamers, P85 and P188, in water and at the surface of the lipid bilayer membrane. Use of the force-field parameters reported here for the poloxamers, in the presence of the polarizable MARTINI water model, nicely reproduce the experimental values of radii of gyration and the expected behavior at the bilayer–water interface. We also performed simulations of poloxamer micelles that are formed when individual units self-assemble in the presence of water. We observed that the P85 micelle ($N = 60$) is almost spherical in shape, whereas the P188 micelle ($N = 21$) is distorted from a spherical shape. In the latter case, the hydrophobic PPO core of the micelle forms a rod-shaped structure. As expected, the hydrophilic PEO chains interact with the lipid headgroups of the bilayer and remain at the interface, whereas the PPO chains prefer to insert into the central hydrophobic region of the bilayer. We did not observe the translocation of the poloxamers through the bilayer in our simulations. We observed that poloxamer micelles although interacting strongly with the lipid bilayer remain attached to the bilayer surface. Only a few PPO units get inserted in the bilayer in a 5 μ s long MD run. The micelles at the bilayer surface lost their nearly spherical shape and curved the membrane at the place of their attachment.

Our MD simulations support the suggestion that P188 micelles help in healing damaged membranes. In a simulation containing a P188 micelle and a bilayer membrane with a pore, the PPO chains of the micelle move into the bilayer through the pore region. This insertion helps to diminish the pore size, ultimately closing the pore in the membrane and thus sealing the damaged bilayer membrane.

Table 5.1: Nonbonded parameters for the interaction of PEO and PPO beads with each other, with polarizable water, and with lipid beads. POL refers to central bead of polarizable water molecule. Q0, Qa, Na and C1 refers to MARTINI lipid bead types corresponding to choline (NC3), Phosphate (PO4), glycerol ester (GL1/GL2), and apolar lipid tails (C1/C2) respectively.²²

Interaction	ϵ (kJ/mol)
PEO - PEO	3.0
PEO - PPO	2.9
PPO - PPO	2.8
PEO -PW	4.0
PPO -PW	3.2
PEO – Q0	4.5
PEO – Qa	5.0
PEO - Na	4.0
PEO – C1	2.7
PPO – Q0	2.3
PPO - Qa	2.7
PPO - Na	2.9
PPO – C1	4.0

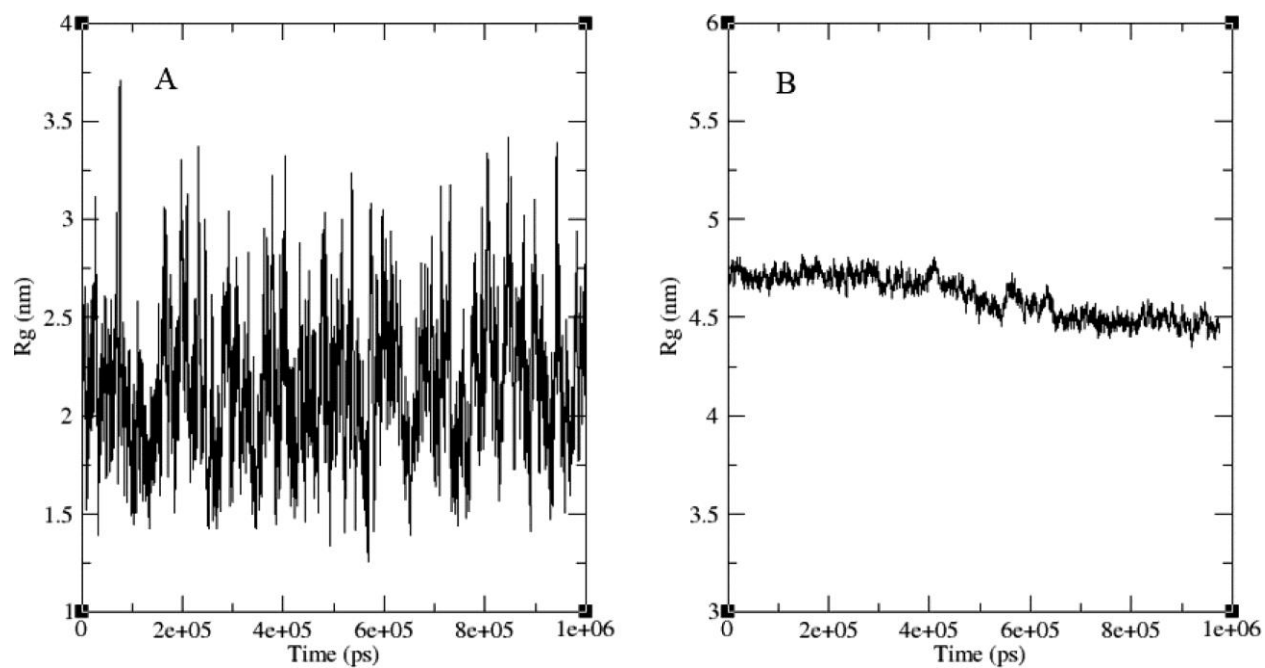


Figure 5.1: Time dependence of radius of gyration of P85 poloxamer molecule at 293 K (A) and micelle (N = 60) at 320 K (B).

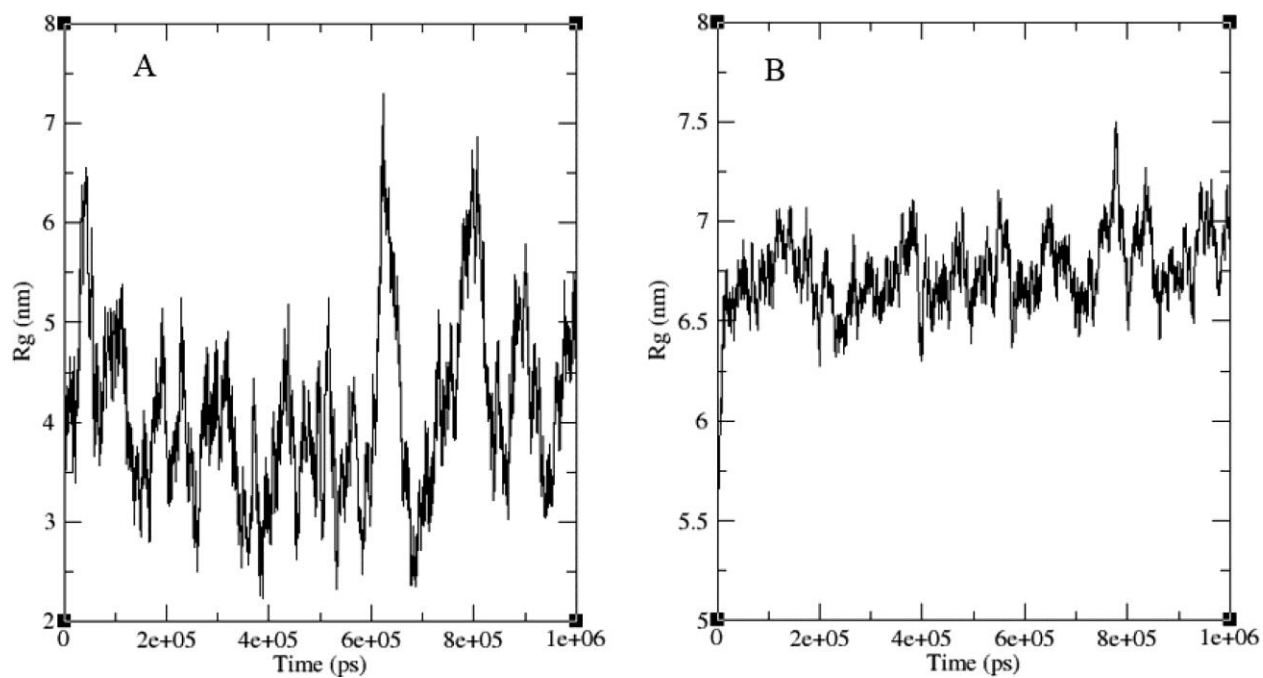


Figure 5.2: Time dependence of radius of gyration of P188 poloxamer molecule at 293 K (A) and micelle ($N = 21$) at 320 K (B).

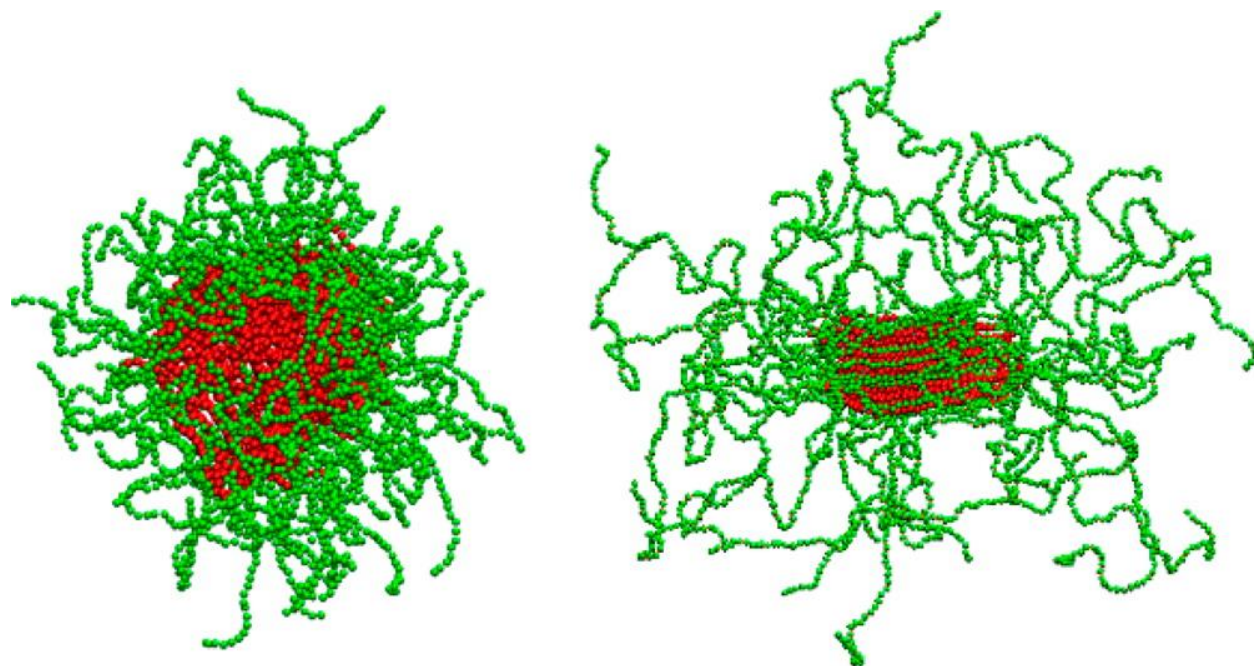


Figure 5.3: Snapshots of micelles of P85 (aggregation number = 60; left) and P188 (aggregation number = 21; right) at 320 K. PEO and PPO blocks are colored in green and red, respectively.

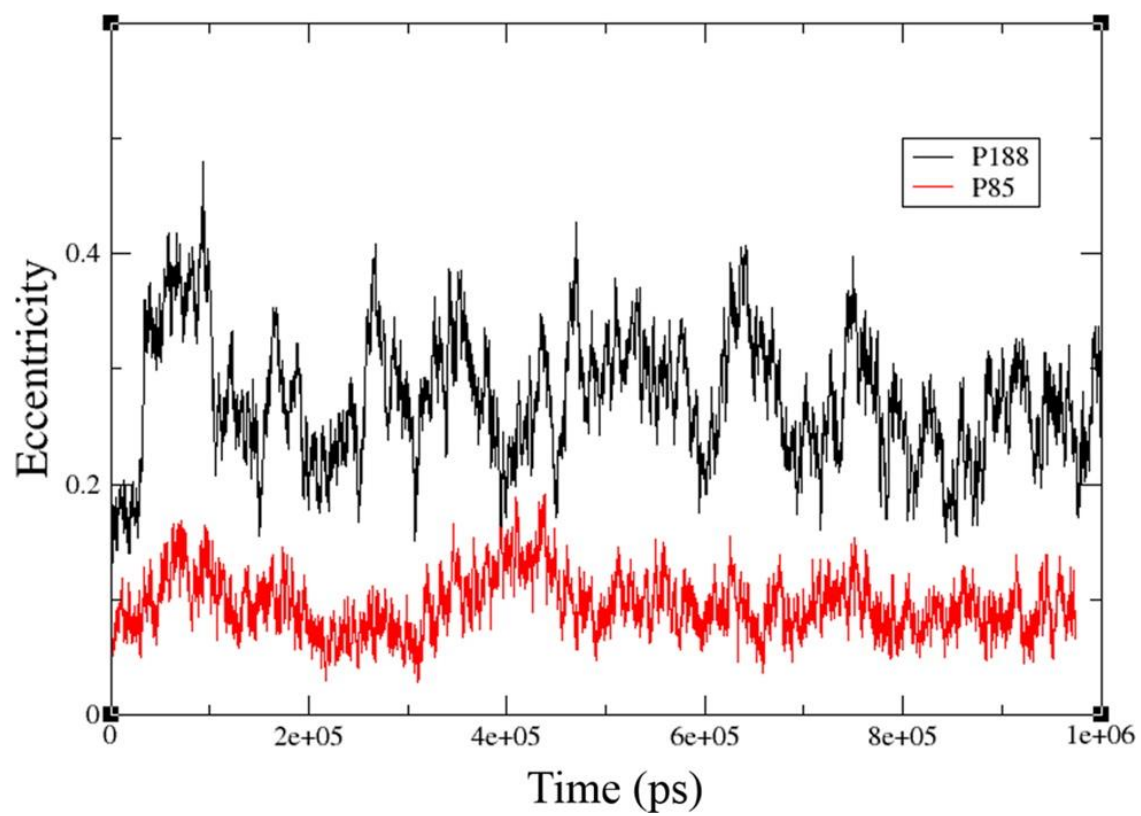


Figure 5.4: Eccentricity of P188 (black) and P85 (red) micelles during 1 μ s simulation.

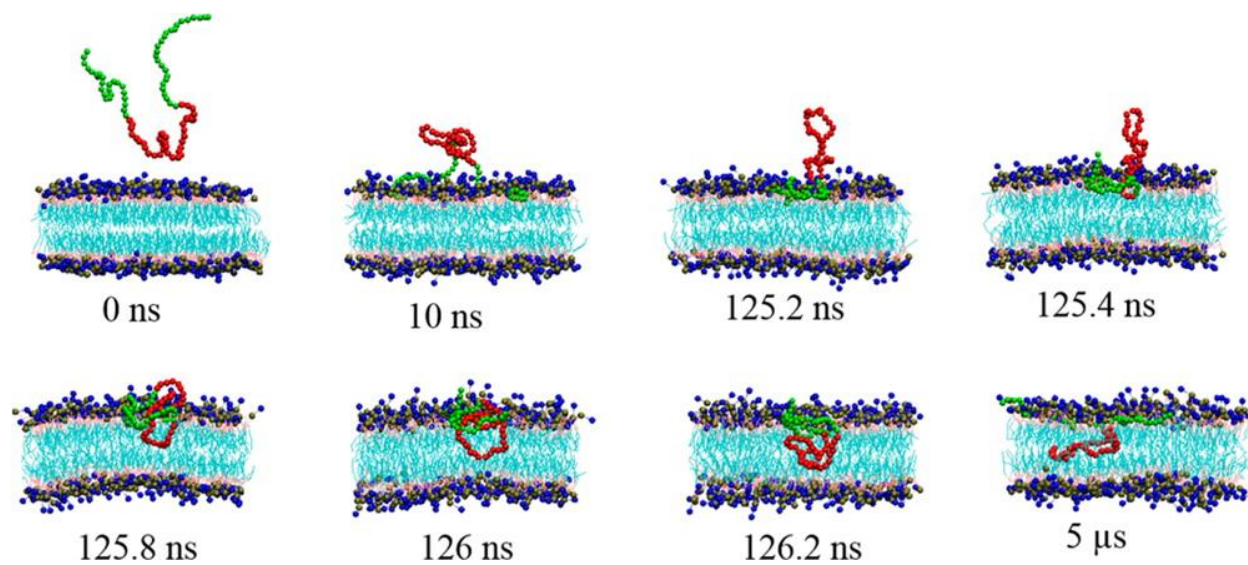


Figure 5.5: Various stages of insertion of Poloxamer P85 into the DMPC bilayer. PO4 bead is shown in brown, NC3 in blue, and lipid tails are in cyan. PEO and PPO blocks are colored in green and red, respectively. Water is not shown for clarity purpose.

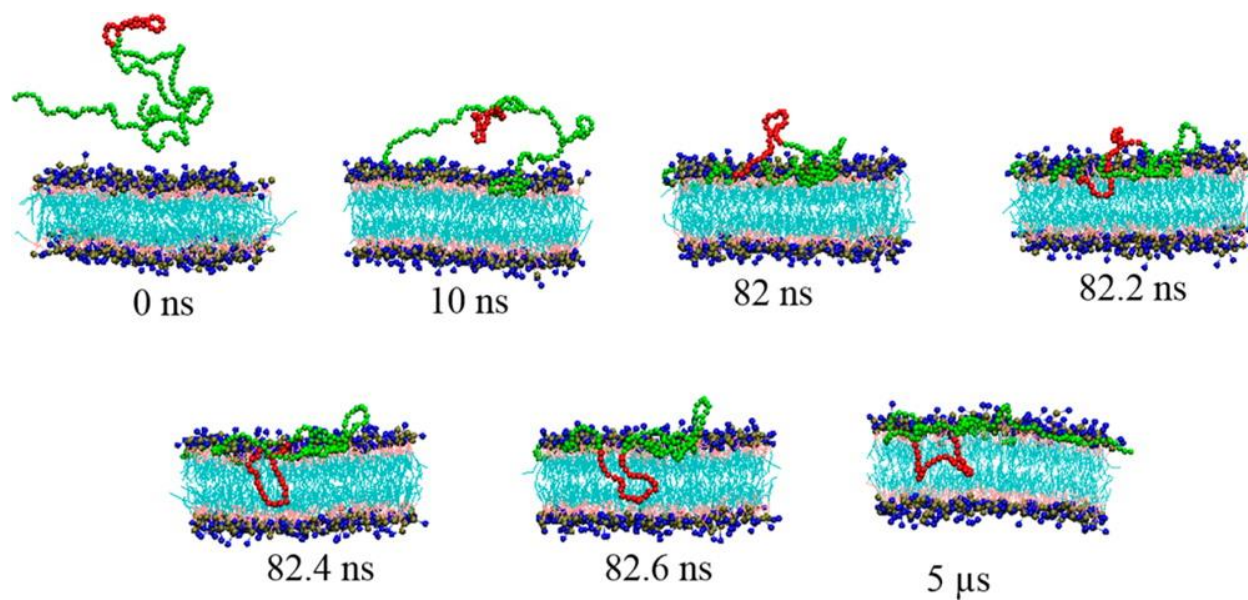


Figure 5.6: Various stages of insertion of Poloxamer P188 into the DMPC bilayer. PO4 bead is shown in brown, NC3 in blue, and lipid tails in cyan. PEO and PPO blocks are colored in green and red, respectively. Water is not shown for clarity purpose.

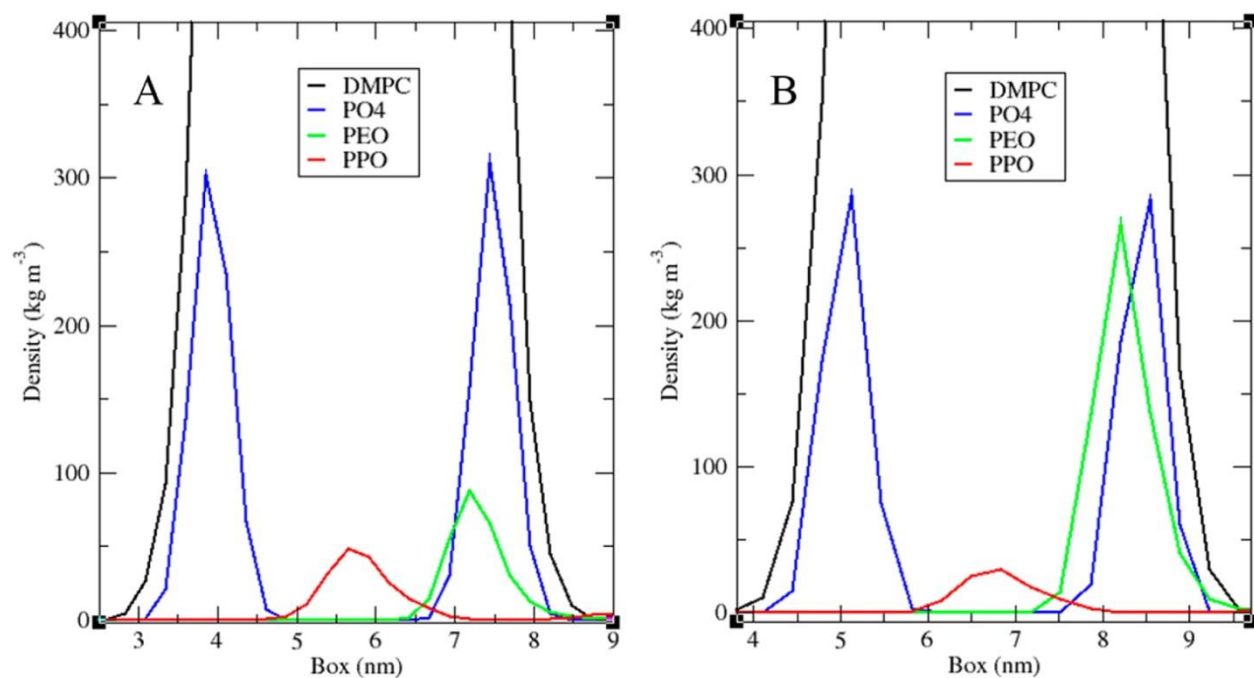


Figure 5.7: Density profiles for cases when P85 (A) and P188 (B) molecules interact with DMPC bilayer during the 1 μs simulations.

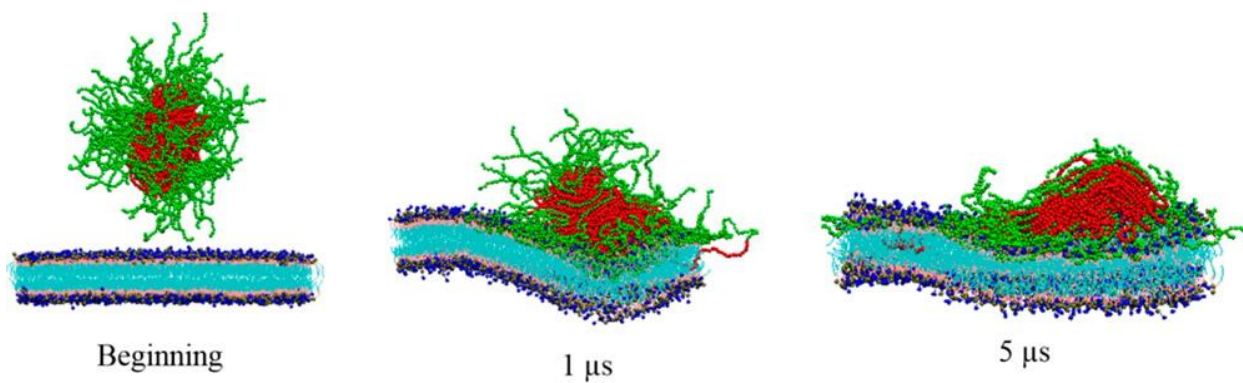


Figure 5.8: Interaction of P85 micelle with the DMPC bilayer. PO4 bead is shown in brown, NC3 in blue, and lipid tails in cyan. PEO and PPO blocks are colored in green and red, respectively. Water is not shown for clarity.

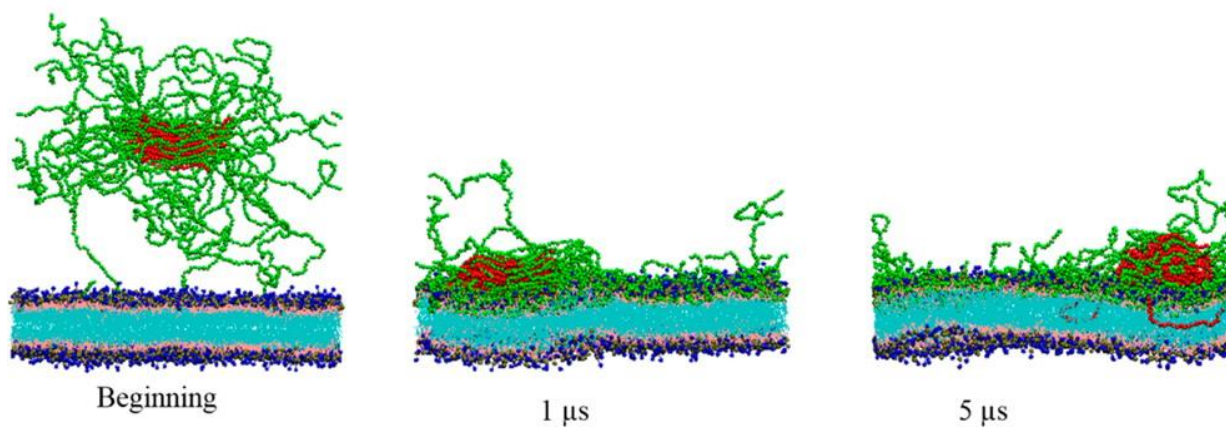


Figure 5.9: Interaction of P188 micelle with the DMPC bilayer. PO4 bead is shown in brown, NC3 in blue, and lipid tails in cyan. PEO and PPO blocks are colored in green and red, respectively. Water is not shown for clarity.

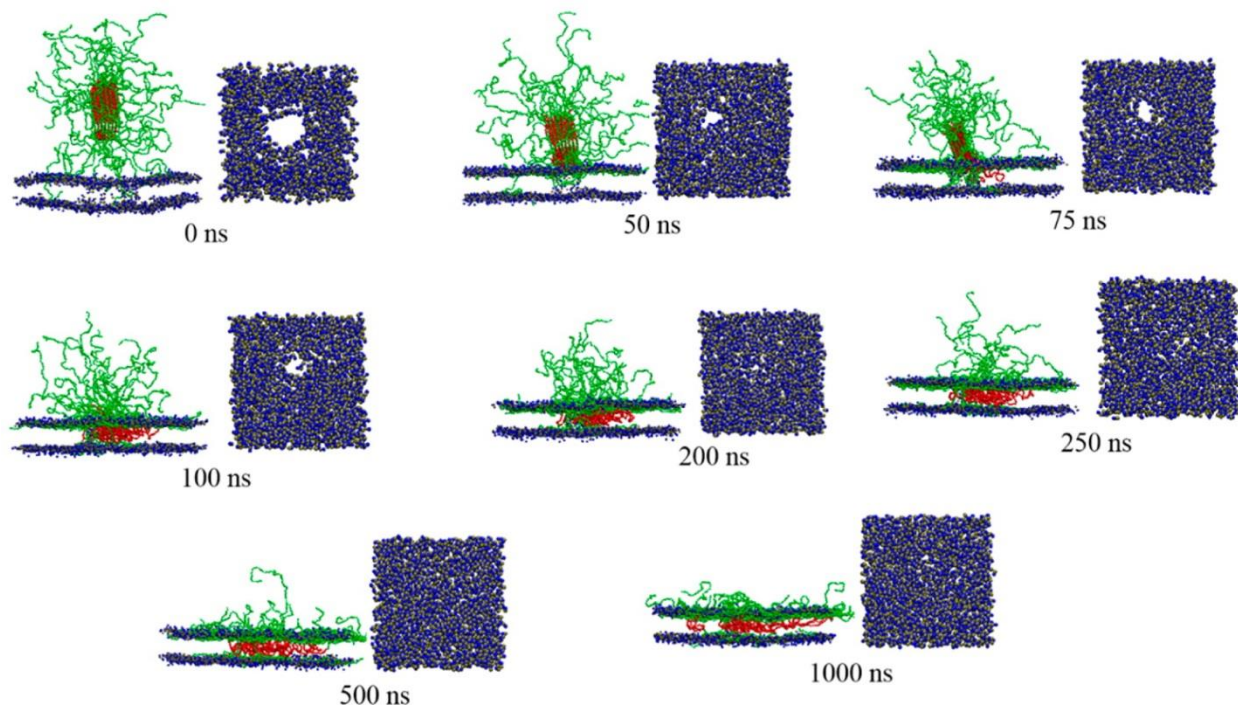


Figure 5.10: Snapshots of interaction of P188 micelle with the DMPC bilayer containing a pore. For clarity, only PO4 (brown) and NC3 (blue) beads of lipids are shown. The picture on the right shows the top view of the pore in the membrane. PO4 beads are shown in brown and NC3 beads in blue. PEO and PPO blocks are colored in green and red, respectively. Water is not shown for clarity.

Chapter 6: Behavior of P85 and P188 Poloxamer Molecules: Computer Simulations Using United-Atom Force-Field⁵

6.1 Introduction

Poloxamers are a group of triblock copolymer molecules (these molecules are also known by their commercial names, one of which is Pluronics) that have been intensely studied recently due to their wide application in industrial and research environments^{169–182}. Poloxamers consist of a central hydrophobic poly(propylene oxide) (PPO) block that is flanked by two hydrophilic poly(ethylene oxide) (PEO) blocks. The number of units in the PEO blocks is the same, and therefore the general formula of a poloxamer molecule is $(\text{PEO})_m-(\text{PPO})_n-(\text{PEO})_m$ (see Figure 6.1A). The hydrophilic/lipophilic character of the polymer is determined by the so-called HLB (hydrophilic–lipophilic balance) index that can be determined by the empirical formula: $\text{HLB} = -36n/(2m + n) + 33$ ¹⁸³. Understanding the nature of poloxamer-lipid bilayer interactions^{41,145,146,175–179,181,182,184,185} is of particular interest since poloxamer molecules are often used as constituents of nanoparticles engineered for drug delivery^{41,172,186}. Clearly this interaction strongly depends on the PEO and PPO block sizes and the poloxamer HLB value, therefore poloxamer molecules with different m , n , and HLB values can be used for different purposes. For example, a poloxamer called P85 ($m = 25$, $n = 40$) with $\text{HLB} = 17$ is used in the pharmaceutical industry to facilitate drug permeation across membranes¹³⁸. Another poloxamer,

⁵ This chapter previously appeared as an article in the Journal of Physical Chemistry B. The original citation is as follows: Goliaei A, Lau E Y, Adhikari U, Schwegler E, and Berkowitz M L, “Behavior of P85 and P188 Poloxamer Molecules: Computer Simulations Using United-Atom Force-Field,” *Journal of Physical Chemistry B* 33, no. 120 (August 2016): 8631.

P188 ($m = 80$, $n = 27$) with HLB = 27.8 is used as a “healer” for damaged membranes, as it acts as a sealant of membranes with compromised integrity¹⁸⁷.

A variety of experimental techniques have been used to study the behavior of poloxamers at membrane interfaces^{177–179,181,182}, but often it is difficult to extract detailed molecular level information from the experiments. Computer simulations techniques, such as molecular dynamics or Monte Carlo, play an important role in providing us with this kind of information, and they were successfully applied to study the structure and dynamics of biological molecules and biological systems^{128,188,189}. Computer simulations were also used recently to study the molecular specifics of membrane/poloxamer interactions^{145,146,151,185,190–192}. Since systems containing polymer molecules, such as poloxamers and lipid bilayers, usually require inclusion of a large number of atoms and since the simulations should be performed over extended periods of time, most of the simulations of polymer/membrane systems are done either using some simple generic models^{176,185}, or using coarse-grained (CG) force-fields^{146,151}. Nevertheless, in some cases a detailed understanding of poloxamer/lipid interactions is required, and therefore it is necessary to consider performing all-atom or at least united-atom force-field simulations, which provide molecular scale resolution. Lately researchers have started to employ multiscale simulations, where in some cases a different resolution is used for a portion of the system, while in other cases the difference in resolution is employed for different time intervals during the simulation^{193,194}. In any case, to perform multiscale simulations one needs to know the force-fields on both coarse-grained and detailed molecular resolution level (all-atom or united-atom). Recently, we reported the results from our coarse-grained simulations where we studied the interaction of two types of poloxamer molecules, P85 and P188, with lipid bilayers¹⁹⁰. We also

studied structures of micelles of these molecules and the interaction of the micelles with a lipid bilayer.

Experimentally, it has been observed that lipid peroxidation has a damaging effect on biological membranes¹⁹⁵. It was also observed that poloxamer molecules with a high HLB index (hydrophilic poloxamers), such as P188 molecule (HLB = 27.8), effectively protect lipids from peroxidation, while poloxamers with a hydrophobic HLB index, like P333 ($n = 60$, $m = 17$, HLB = 10) or P335 ($n = 56$, $m = 37$, HLB = 17; this HLB index is the same as the index of the P85 poloxamer) do not prevent lipids in membranes from peroxidation¹⁹⁶. The difference in protecting ability of poloxamers was explained as due to the difference in the polymer behavior when interacting with the lipid membrane. It was suggested that hydrophobic poloxamers penetrate the membrane, while hydrophilic poloxamers are just adsorbed on the membrane surface, covering it and therefore providing a barrier against oxidants entering the bilayer¹⁹⁶. From our previous coarse-grained force-field simulations¹⁹⁰, we observed that both hydrophobic P85 and hydrophilic P188 poloxamers behaved similarly: they inserted their hydrophobic block into the bilayer. To determine whether this behavior is due to the use of a coarse-grained force-field, we decided to simulate systems containing the same poloxamers, P85 and P188, but using a more detailed united-atom force-field. Since some of such force-fields reported in the literature displayed problems when we attempted to calculate radii of gyration of poloxamers solvated in water, we had to modify some of the force-field parameters, as we describe below. Determining united-atom force-field parameters for poloxamer molecules is also important when simulations need to consider details about poloxamer/protein interactions, like it may be needed to be done for understanding how these copolymers reduce the multidrug resistance of the cells⁴¹.

In this paper we report the results from simulations on systems containing P85 and P188 poloxamer molecules by using more detailed united-atom force-field. The emphasis in our work is to consider the interaction of these poloxamer molecules with lipid membranes. We chose not to study poloxamer micelles here, since simulations of these systems using all-atom or united-atom description would require considerable computational resources.

6.2 Methods

6.2.1 United-Atom Force-Field Parameters

An important requirement for performing molecular dynamics simulations of systems containing poloxamer molecules using atomic resolution force-field is to have a set of reliable parameters able to describe the nonbonded interactions of the polymer's ether oxygen with the other atoms in the system. In this work we use a modified version⁴³ of the standard GROMOS 53A6²³ united-atom force-field, where the values for the van der Waals parameters are the same as in standard GROMOS, but the ether oxygen parameters have been changed to reproduce the experimentally observed behavior of α,ω -dimethoxypolyethylene glycol in aqueous solutions. Since the revised GROMOS-like force-field was available for simulations of PEO only, we had to augment the force-field with parameters for the PPO block. We used the same van der Waals parameters as for PEO, and adjusted the charges on the poloxamers. The new set of charges was obtained by performing quantum chemical calculations on small molecules representing monomers in the triblock copolymers. The charges of poly(ethylene oxide) (PEO) monomers, dimethoxyethane (Figure 6.1B), and poly(propylene oxide) (PPO) monomers, 1,2-dimethoxypropane (Figure 6.1C) were obtained by using Gaussian 09/b1 program¹⁹⁷ with the MP2/6-31+G** level of theory, using Natural Bond Orbital method¹⁹⁸. The quantum chemical

calculated charges for the PPO monomer (Figure 6.1C) were further fine-tuned by a series of simulations with reduced charges, each 200 ns in duration, to get the proper radius of gyration in water (see the Results section for further details). The general structure of poloxamers with the final charges used in this work are displayed in Figure 6.1A. The components of the force-field describing bonding interactions were adopted from the GROMOS 53A6 force-field and are reported in Table 6.1. Since the propylene oxide monomer in the PPO block has a chiral carbon, parameters for an extra improper dihedral were added to the original GROMOS 53A6 set of bonded parameters and denoted gi_4 ($\xi_0 = -35.26439$ degrees, $k_\xi = 334.84617$ kJ mol⁻¹ rad⁻²). These dihedral parameters are the same as the original gi_2 parameters ($\xi_0 = 35.26439$ degrees, $k_\xi = 334.84617$ kJ mol⁻¹ rad⁻², with the same numerical value for the angle and same force constant), except that the angle in our case is opposite in sign and accounts for the left-handed isomer.

6.2.2 Molecular Dynamics Simulations

To calculate the radii of gyration of our poloxamer molecules, we performed simulations where a single poloxamer molecule was placed in a box of solvent. We also investigated the behavior of poloxamers at the water/air interface. The emphasis of our work was to study poloxamer interactions with lipid membranes and their ability to “heal” damaged membranes. Thus, we studied systems containing lipid bilayers with and without pores in them. All our molecular dynamics simulations were performed using the Gromacs 4.6.5^{67,107–109} suite of programs. Both P85 and P188 were constructed in such a way that a random distribution of right handed and left handed isomers of propylene oxide monomers was present in the PPO block. To simulate the system with P85 solvated in water, we used a cubic box $15.9 \times 15.9 \times 15.9$ nm³ in

length containing 131,682 SPC water molecules¹⁹⁹, while for the system with P188, the box size was $16.37 \times 16.37 \times 16.37 \text{ nm}^3$ and contained 143,883 SPC water molecules.

The simulation with P85 at the air/water interface was performed using a cell with dimensions of $8.9 \times 8.9 \times 24.9 \text{ nm}^3$. A slab of water containing 25,420 SPC water molecules and one P85 molecule was placed at each interface between water and air (total of two P85 molecules in the cell). An air/water interfacial simulation for the P188 molecule was performed in a cell with the size of $16.37 \times 16.37 \times 26.37 \text{ nm}^3$. The cell contained 143 883 SPC water molecules in a slab, and in this case only one poloxamer molecule was placed on one of the air/water interfaces.

Two simulations, each 600 ns long, were performed to study the interaction of P85 with 1,2-dilauroyl-*sn*-glycero-3-phosphocholine (DLPC) lipid bilayer. Additionally, two simulations, each 800 ns long, were performed to study the interaction of P188 with the DLPC bilayer. In these simulations a patch of a lipid bilayer containing 200 DLPC lipid molecules (34 016 SPC water molecules, box $8 \times 8 \times 19.5 \text{ nm}^3$) represented in the united-atom resolution was used to model a biological membrane. DLPC parameters were obtained from Poger et al²⁰⁰. In all united-atom simulations, the short-range cutoff for nonbonded interactions was set to 1.2 nm and for the long-range electrostatics the particle mesh Ewald (PME) algorithm^{201,202} was used. Periodic boundary conditions in all directions were applied, and the simple point charge (SPC) water model¹⁹⁹ was used. To achieve constant temperature and constant pressure, the Nosé–Hoover thermostat^{203,204} and the Parrinello–Rahman barostat^{159,160} were used, respectively. The time constants for the thermostat and barostat were set to 0.5 and 5 ps, respectively, and compressibility was set to $4.5 \times 10^{-5} \text{ bar}$. Trajectories were visualized using the VMD⁷⁸ software. The time step for solving the equations of motion was set to 2 fs.

To study the influence of the initial arrangement of the poloxamer with respect to the membrane, we prepared the initial configuration of a system containing a P85 poloxamer using coarse-grained simulations. The simulations were done using a force-field where poloxamers were described by modified MARTINI parameters^{65,190} and polarizable water⁶⁶. We simulated a system containing one P85 molecule solvated in an $8 \times 8 \times 8 \text{ nm}^3$ box containing ~ 2800 polarizable water particles and 200 DLPC lipid monomers in a random arrangement and allowed the molecules to self-assemble. Coarse-grained simulations were performed under NPT ensemble, where temperature was kept constant using a velocity-rescaling scheme¹⁵⁸, and pressure was kept constant at 1 bar using the Parrinello–Rahman pressure coupling scheme^{159,160}. The time constants for temperature and pressure couplings were 1 and 12 ps, respectively and compressibility was set to 3×10^{-4} bar. The cutoff for electrostatics and Lennard-Jones interactions was set to 1.2 nm using the shift scheme and the dielectric constant was set to 2.5. All coarse-grained simulations used a 20 fs time step. Initially the system was simulated for 10 ns under isotropic pressure coupling ($T = 320 \text{ K}$) to achieve a bilayer formation. The simulation was continued for another 10 ns using semi-isotropic boundary conditions to obtain the correct lipid configuration. Finally the conversion from MARTINI to united-atom resolution was done using the Backward²⁰⁵ tool and 400 ns simulation under NPT ensemble ($T = 320 \text{ K}$) was performed. This procedure was repeated two more times to provide a total of three simulation replicas.

To prepare a model of a damaged membrane (membrane containing a hydrophilic pore) a patch of a DLPC membrane containing 200 lipid molecules and 8500 water particles was generated using the “insane.py” script¹⁶². We chose to simulate DLPC membranes due to our observation that a DLPC lipid produces more stable pores. The system had a box size of $7.5 \times$

$7.5 \times 20 \text{ nm}^3$. We used a coarse-grained MARTINI force-field²² to describe it. The generated structure was simulated under NPT ensemble ($T = 320 \text{ K}$) for 10 ns; following this equilibration period an electric field ($E_z = 0.7 \text{ V nm}^{-1}$) was applied for a short time in the Z direction until a pore was formed. The produced structure was further simulated under NPT ensemble ($T = 320 \text{ K}$, isotropic pressure coupling) for 10 ns in order to produce a stable pore. The resulting pore had a diameter of about 6 nm. At this point, the system was transformed to the united-atom resolution for further experiments. To study the effect of poloxamers on membranes with a pore, P85 and P188 molecules were placed in water, all on the same side with respect to the bilayer. We placed five P85 molecules and three P188 into separate porated membrane systems. The combined systems (pore and poloxamers) were simulated for about 25 ns under NPT ($T = 303 \text{ K}$, semi-isotropic pressure coupling) conditions in order to reduce the diameter of the pore to 3 nm. During this time, poloxamers were kept frozen using a harmonic potential with spring constant of $1000 \text{ kJ mol}^{-1} \text{ nm}^{-2}$. Once the pore diameter reached $\sim 3 \text{ nm}$, the ensemble was switched to NP_zAT, the constraints on poloxamers were removed and the simulation was continued for 400 ns. We performed five simulations of systems containing P85 molecules and three simulations on systems with P188 molecules; each simulation was done starting with different initial configurations. For each case we also simulated the membrane with a pore but without the poloxamer to use as a control. To monitor the closure of the pore we counted the number of water molecules in the pore. This was done using the PLUMED 2.1 plug-in¹³⁷ for GROMACS. Thus, at any time step, the center of mass (COM) of the bilayer was calculated, and we counted the number of water molecules having their Z coordinates of oxygen atoms above or below a certain distance from the Z coordinate of the bilayer's COM. This distance was set to 1.5 nm for each leaflet. Water molecules that had their Z coordinates in this interval were considered to be

located in the pore. This analysis was performed for both control systems and the ones that included bilayers with pores and poloxamer molecules.

6.3 Results

6.3.1 Simulations of P85 and P188 in Water

To validate our new force-field parameters for poloxamers, we tested whether our simulations could reproduce experimentally measured values for the radii of gyrations of individual P85 and P188 molecules solvated in water. The experimental value for the radius of gyration of a P85 molecule solvated in water at 20 °C is in the range of 1.7 to 2.0 nm¹⁵³. To test whether our constructed force-field can reproduce a value in the same range, a single P85 molecule was solvated in a box of water (for details of this simulation and other described below, see Methods section) and a molecular dynamics run was performed for 400 ns. We initially performed the run using the full charge values obtained from quantum chemical calculations. However, we observed that using these charges, the molecule had a somewhat linear structure and its radius of gyration $R_g = 2.5 \pm 0.51$ nm was substantially larger than the value from the experimental range. To reduce the interaction of the hydrophobic core of the P85 with water, the charges of PPO monomers were decreased. The first attempt was to divide the charges by half, which resulted in a completely globular form of the molecule ($R_g = 1.1 \pm 0.07$ nm). Following this step, a series of simulations were performed, where each one had the charges of the PPO monomers reduced by 20%, 25%, and 30%. We observed that when the charges of the PPO hydrophobic core were reduced by 30%, the radius of gyration reached a value within the experimental range ($R_g = 1.73 \pm 0.36$ nm; these values were obtained from the last 350 ns of the

400 ns trajectory). The instantaneous values of R_g along the trajectory are shown in Figure 6.2). The reduced charges we used for all further united-atom simulations are shown in Figure 6.1A.

The same set of charges we obtained from the P85 simulation in water was used to simulate P188 in a box of water. The experimental value for the radius of gyration of P188 in water is 3.1 nm¹⁵⁶. To verify that our force-field can produce a value close to this, a molecule of P188 was solvated in a box of water and following this we performed an MD run for 765 ns. Figure 6.3 shows the fluctuations of the radius of gyration during this run. The average radius of gyration for P188 was calculated from the last 400 ns of the simulation, since, as Figure 6.3 shows, the fluctuations in R_g stabilized within this time interval. The calculated $R_g = 2.76 \pm 0.4$ nm, which is in good agreement with experiment.

6.3.2 Simulations of P85 and P188 at the Air/Water Interface

For a further qualitative validation of the force-field we studied the distribution of each of the polymeric blocks of the poloxamers at a hydrophobic/hydrophilic interface and therefore we considered systems containing poloxamers at the air/water interface. Since the PPO block is hydrophobic and PEO is hydrophilic, the expectation was to find PEO in water and PPO at the interface for the majority of the simulation time. To study the behavior of P85 at the interface, we prepared a symmetric simulation box, so that the water slab was in the middle of the box surrounded by air at each side (Figure 6.4A). This allowed us to consider two P85 molecules and therefore improve on our statistics. Using the same symmetry arrangement for the box in the P188 simulation case would require much more computational resources due to the size of the extended poloxamer and, therefore, only one P188 was considered (Figure 6.5A). The average density of PEO and PPO over the course of the simulation was calculated and shown in Figures

6.4B and 6.5B. A typical configuration of the P85 and P188 polymers are also depicted in Figures 6.4A and 6.5A. As expected, the PPO (hydrophobic block) stays at the interface while the PEO (hydrophilic block) spends the majority of its time inside the water. To further investigate the configuration of the PPO component at the interface, the radii of gyration (Figures 6.6 and 6.7) for the middle block of both P85 and P188 poloxamers were calculated (the values we present are the averages over the last 50 ns of the trajectories). The average R_g for the PPO block of the two P85 molecules was 0.96 ± 0.09 nm and 0.97 ± 0.07 nm and for the P188 it was 0.80 ± 0.06 nm. As observed from Figures 6.4A and 6.5A, the PPO block of both P85 and P188 molecules tend to arrange in a globular structure at the hydrophobic/hydrophilic interface. This structure displays small size fluctuations, which is reflected in the small root-mean-square deviations (see also Figures 6.6 and 6.7).

6.3.3 Interaction of P85 and P188 Poloxamers with the DLPC Model Membrane

Following the verification of the force-field parameters by calculating the radii of gyration and obtaining the expected behavior of poloxamers at the air/water interface, simulations were performed to study the interaction of these poloxamers with a DLPC membrane. It has been suggested⁴¹ that a more hydrophobic-like poloxamer, such as P85, follows three steps upon interaction with lipid bilayers: absorption, insertion, and translocation, whereas a hydrophilic poloxamer, such as P188, gets adsorbed to the surface of the membrane and remains on the surface. Given the size of our systems and time scales one can probe with simulations that employ a united-atom force-field, we do not expect to observe the translocation step. Every system containing a DLPC bilayer, water, and either P85 or P188 poloxamer was simulated twice. For each case, the poloxamer was placed next to the surface of a patch of 200 DLPC lipids starting from different initial configurations in each of two simulations with the

same poloxamer. Simulations for P85 were performed for 600 ns, while for P188 they were extended to 800 ns. The results are shown in Figures 6.8A,B and 6.9A,B. In all cases, the poloxamers were adsorbed on the membrane surface, and, following this step, the PPO block (hydrophobic part) penetrated into the hydrophobic core of the bilayer and remained there for the rest of the simulation. This anchoring to the membrane is an important step, which emphasizes the amphipathic character of poloxamers molecules as surfactants. To better follow the time at which the PPO block penetrates into the membrane, we present graphs that show the distance between the center of mass of DLPC and PPO segments (Figures 6.8C and 6.9C). These graphs show that it takes a longer time for the hydrophobic block of P188 to penetrate the lipid bilayer, probably due to stronger adsorption of hydrophilic blocks of this poloxamer to the interface. Also notice that the hydrophobic block of P188 is shorter than in P85 molecule, which makes it less hydrophobic.

6.3.4 Self-Assembly of P85 Poloxamers, DLPC Lipid Monomers, and Water

We did not observe any translocation of the P85 molecule across the membrane in any of our two simulations performed on systems containing this poloxamer and lipid membrane. It is possible that to observe such a translocation we need to start with a conformation where the poloxamer is initially in a transmembrane configuration. However, since there is no information available on conformation of poloxamers in a transmembrane configuration, the results may depend on the choice of the initial configuration. We decided to avoid this bias by simulating the self-assembly of a system containing a P85 poloxamer, water, and DLPC lipids. Self-assembly allows the molecule to find a more favorable initial configuration that has a lower free energy. To perform a self-assembly simulation we used our newly developed coarse-grained force-field¹⁹⁰ and performed three independent simulations where one P85 molecule was

solvated in a box of 200 DLPC lipids and ~2800 polarizable water particles. Once the bilayer was formed and the P85 found its place in the membrane, the system resolution was transformed into the united-atom resolution and each of the three simulations was continued for an additional 400 ns under NPT ($T = 303$ K) ensemble. Figure 6.10 shows snapshots from one of the three simulations of P85 and DLPC lipid molecules, right after self-assembly and after 400 ns of united-atom simulation. We observed that in all three cases the poloxamer inserts into the membrane in such a way that its hydrophobic block resides in the hydrophobic core of the membrane, while the hydrophilic flanking segments protrude from each side of the bilayer and interact with water. During all the runs we performed, we did not observe a P85 translocation to the other side of the membrane, since such a translocation would require overcoming a significant free energy barrier.

6.3.5 Interaction of P85 and P188 Poloxamers with Damaged DLPC Model Membrane

It is known that poloxamers such as P188 have membrane-sealing properties and can be used as agents that restore the integrity of a damaged membrane^{39,40,42}. The molecular details of how this occurs are not known, and molecular dynamics simulations could potentially provide molecular resolution pictures of the possible mechanism by which these molecules work. Recently, using coarse-grained simulations, we studied the behavior of micelles of P188 next to a damaged membrane¹⁹⁰. In this work, to provide a more detailed picture, we performed united-atom simulations of systems containing P85 and system containing P188 molecules next to a model damaged DLPC membrane with the damage represented by a pore of 3 nm in diameter. Five poloxamers were placed in systems with P85 molecules and three when systems contained P188 molecules. The poloxamers were initially placed into the solution in some proximity of the pore. (Figures 6.11A and 6.12A). We performed a total of five simulations for systems

containing P85 poloxamer and three simulations for systems with P188. Every simulation we started with a different initial configuration of lipids (although the diameter of the pore stayed the same) and a different initial arrangement of the poloxamer molecules on the top of the bilayer. As we observed previously, the pore in the membrane contracted and closed after ~ 100 ns in the NPT simulation; therefore to have a stable pore and reach longer time scales in our simulations, we performed them under NP_zAT ensemble ($T = 303$ K). Each simulation was performed for 400 ns. We observed a partial pore closure in each simulation and quantified it by counting the number of water molecules within the pore (see Methods). Figure 6.11B shows the time history of the number of waters in one of the simulations with the pore and P85 and also in a control simulation with no poloxamer. In addition, we display a few snapshots from this simulation. All of the simulations with P85 produced similar qualitative results. As we observed, and the snapshots illustrate, in all cases P85 poloxamers initially located in solution tend to aggregate and adsorb on the surface of the membrane, but not in the place where there is a pore. Following the aggregation step, the hydrophobic block of the poloxamer penetrated the membrane and anchored in the tail region outside the pore. As a result the membrane got compressed, and consequently some of the water molecules in the pore were forced from the membrane. Similar processes occurred in cases when the poloxamer is P188, as shown in Figure 6.12A. Nevertheless, there is a difference between the cases with P85 and P188. Since P188 has two longer hydrophilic blocks, we observe that these blocks can also occupy the pore region. Figure 6.12B shows that during 400 ns of the run only partial closing of the pore occurred.

6.4 Discussion and Conclusions

We developed a united-atom force-field to treat systems containing triblock copolymer poloxamer molecules. To validate the performance of this force-field quantitatively, we

calculated the radii of gyration of two poloxamer molecules, P85 and P188, dissolved in water, and we observed that calculated values reproduced experimental data. For a qualitative validation of the force-field we studied the density of P85 and P188 poloxamer molecules at the air/water interface and observed that the density distributions were in agreement with the expected ones for these triblock copolymers.

Our choice of simulating P85 and P188 was dictated by their wide use in the pharmaceutical industry and their known effects on cellular membranes. In addition, we recently studied the behavior of the same two poloxamers by performing coarse-grained simulations using a modified MARTINI force-field¹⁹⁰; present united-atom force-field simulations allow us to compare poloxamer properties when observed at different resolution. Our simulations of systems containing one poloxamer molecule (P85 or P188) at the water/lipid bilayer interface demonstrated that, for both poloxamers, the results from the united-atoms simulations are qualitatively similar to the results we obtained from coarse-grained simulations. In both types of simulations and for both poloxamers, we observed that poloxamers behaved as surfactant molecules at the interfaces separating hydrophobic and hydrophilic regions. Thus, the hydrophobic blocks of poloxamers (PPO) entered the hydrophobic part of the bilayer containing aliphatic tails of lipid molecules, while the hydrophilic blocks of poloxamers (PEO) stayed in the hydrophilic region at the water/lipid headgroup interface. Our present unbiased simulations using united-atom force-field demonstrated that for poloxamers with large sized hydrophilic blocks, such as P188, relatively long runs are required to observe the penetration of the hydrophobic block into the membrane (~700 ns).

It was observed in experiments that poloxamers with a hydrophilic HLB index can protect lipids from peroxidation, while poloxamers with a hydrophobic HLB index did not

prevent lipids in membranes from peroxidation¹⁹⁶. To explain this observation, it was suggested that hydrophobic poloxamers penetrate the membrane, while hydrophilic poloxamers stay adsorbed on the membrane surface providing a barrier against oxidants¹⁹⁶. As we observed, the hydrophilic copolymer, P188, and the hydrophobic P85 behave similarly: they insert their hydrophobic block into the bilayer and anchor the poloxamer in the membrane. However, P188 has larger hydrophilic blocks that cover the surface of the membrane and therefore these blocks may still provide a barrier to prevent the free radical chain reaction needed for the peroxidation process to take place. The behavior of P188 and P85 poloxamers next to lipid bilayers observed in our simulations using united-atom force-field is therefore very similar to the one we observed in our simulations where we used coarse-grained force-field¹⁹⁰.

It was also observed that P188 poloxamer can “heal” damaged membranes¹⁸⁷. We represented a damaged membrane in some of our simulations with a pore in the membrane and to remove a tendency for the pore to close in the NPT ensemble simulation, we performed our simulations of systems with a pore at constant area per lipid, which is equivalent to having a nonzero tension. In our simulations with poloxamers and membranes containing a pore, we observed that poloxamers aggregate in water and insert their aggregated hydrophobic block into the lipid bilayer, so that the block is located next to the pore, but not in the pore. Poloxamer block insertion into the bilayer increases the pressure, thereby allowing the membrane to push out the waters from the pore and reduce the pore size. It is possible that a larger number of poloxamers next to a damaged membrane could completely remove the pore, but when the number of poloxamers is large, they tend to form micelles, a very time-consuming process to study with all-atoms or even united-atoms simulations. Our previous coarse-grained simulations of systems containing P188 micelles and bilayers with a pore showed that poloxamer micelles

close the pore by filling it up with the poloxamers from the micelle¹⁹⁰. It has been previously suggested that after the membrane is “healed” by poloxamers, the copolymers get dissociated from the membrane¹⁹⁶. The mechanism of this step is not known and our simulations do not reproduce it, since it may require much longer simulation time. It is also possible that “healing” of membranes with the help of poloxamers requires a presence of processes that involve activity of proteins from the cells or activity of membrane proteins and, clearly, this kind of process is not present in our simple model.

Table 6.1: The Gromos 53A6 bonded interactions used in this study.

		53A6 Code
Bond stretching	C — O	gb_13
	C — C	gb_27
Angle bending	C — O — C	ga_10
	C — C — O	ga_9
	C — C — C	ga_15
Dihedral torsion	C — C — O — C	gd_23
	O — C — C — O or C — C — C — O	gd_34
Improper dihedral angle	CH3 — CH2 — O — CH	gi_2 or gi_4 ^a

^a. gi_4 is the same as original Gromos 53A6 gi_2 improper dihedral except its angle is negative and accounts for the left handed isomer of the chiral center of PPO monomers.

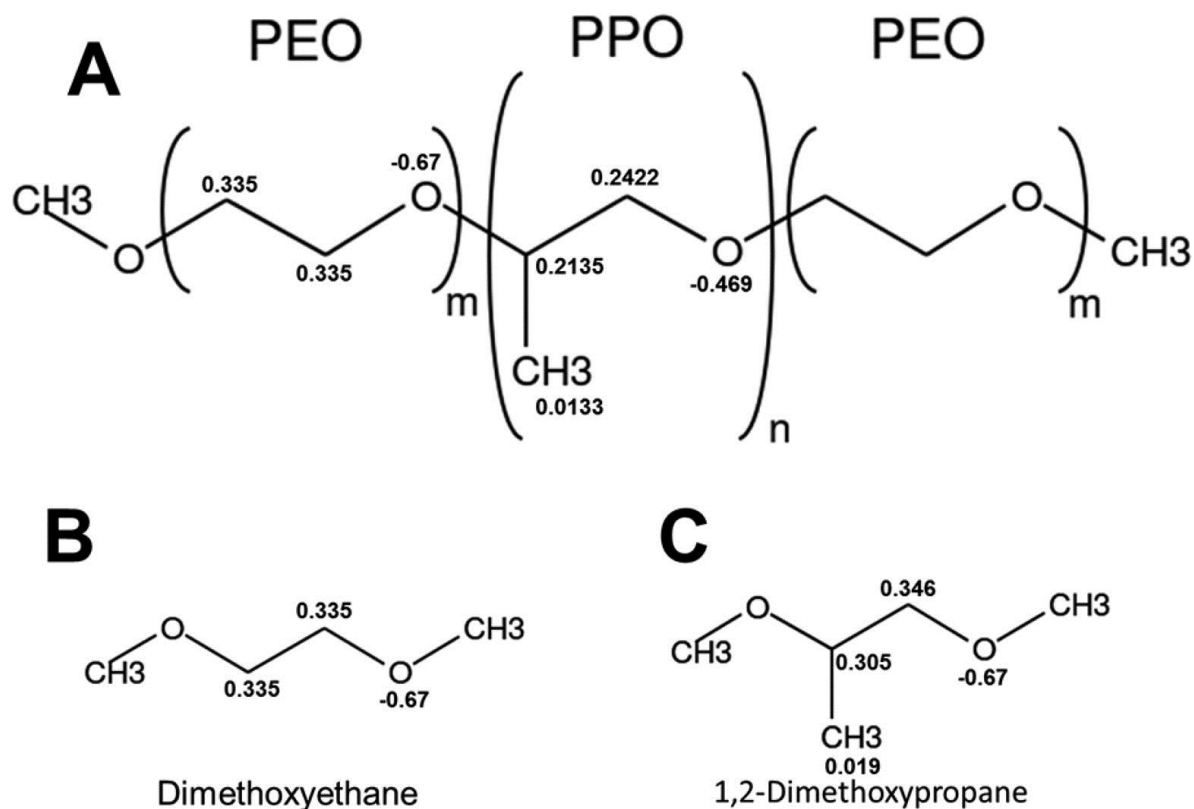


Figure 6.1: Chemical structure of poloxamers. (A) General structure of the poloxamers with the corresponding charges used in this paper. The letters m and n determine the number of monomers in each block. (B,C) Small molecules representing the building blocks of poloxamers used for quantum chemical calculations of charges.

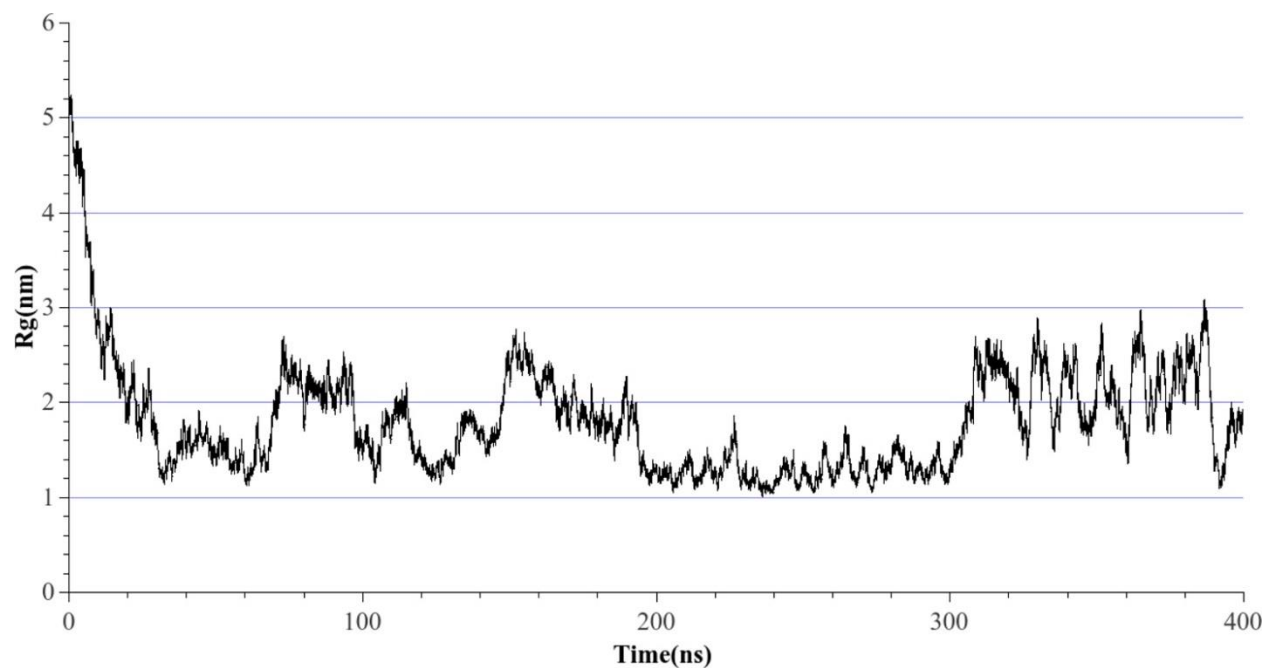


Figure 6.2: The radius of gyration of P85 in water. Fluctuation of Rg as a function of time throughout the 400 ns simulation. Data from the last 350 ns were used to calculate the average and also the rmsd from the average.

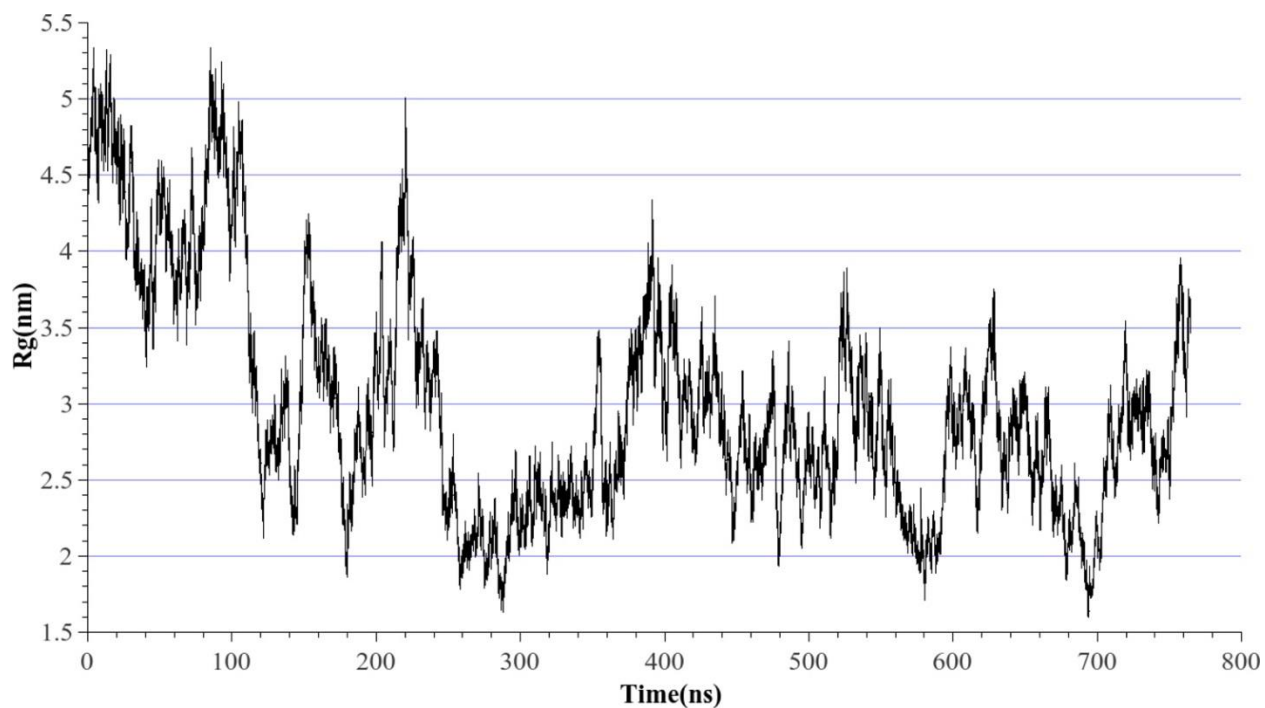


Figure 6.3: The radius of gyration of P188 in water. Fluctuation of Rg as a function of time throughout the 765 ns simulation. Data from the last 400 ns were used to calculate the average and the rmsd from the average.

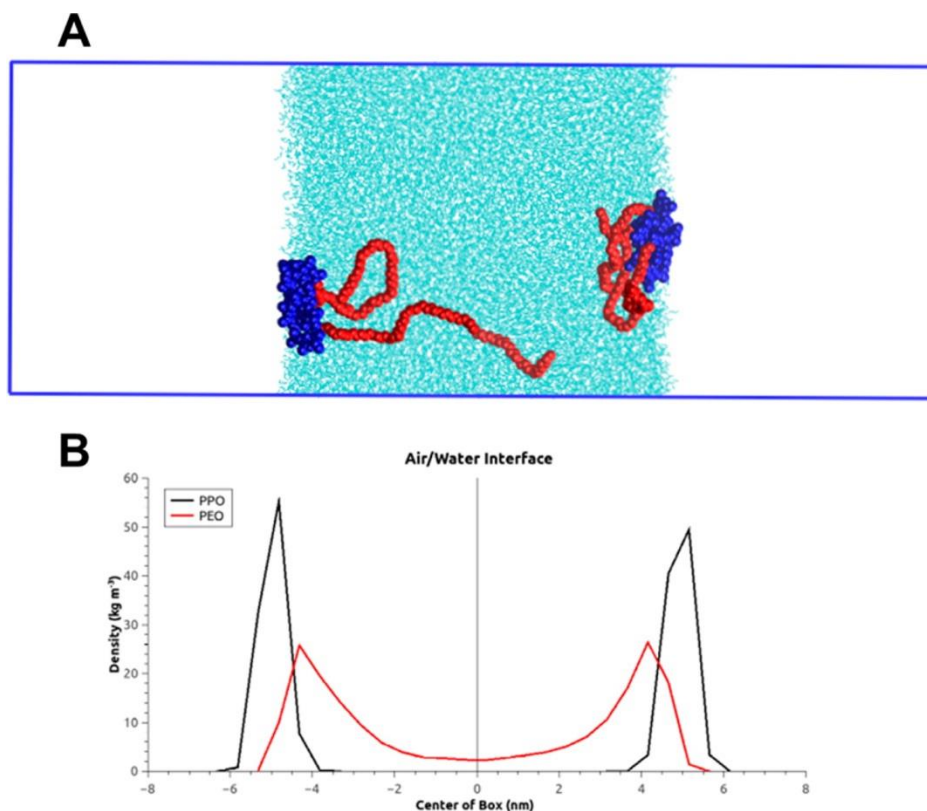


Figure 6.4: P85 molecules at the interface of air/water. Panel A shows the unit cell for the air/water system. The middle part of the cell (cyan) is the water slab. The hydrophobic part of the poloxamer is color coded blue, and the hydrophilic one is red. Panel B shows the average densities of PPO and PEO blocks obtained from the 100 ns simulation trajectory.

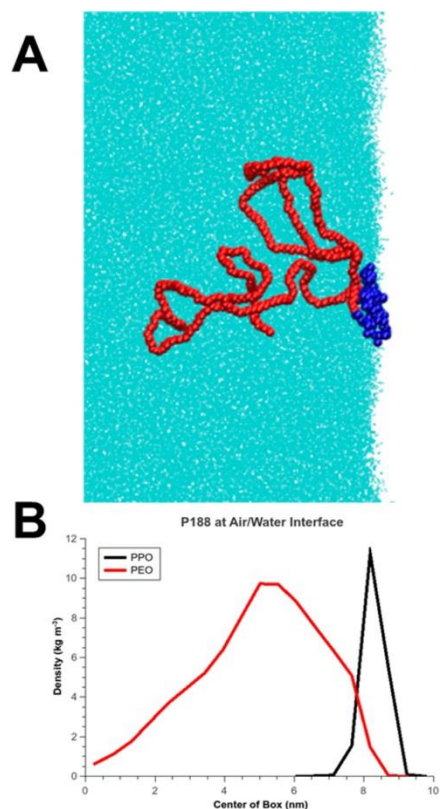


Figure 6.5: P188 molecule at the interface of air/water. Panel A shows the simulation cell for the air/water system. The water is color coded cyan, and the P188 poloxamer is placed on the interface. The hydrophobic part of the poloxamer is color coded blue, and the hydrophilic part is red. Panel B shows the average densities of PPO and PEO blocks obtained from the 75 ns simulation trajectory.

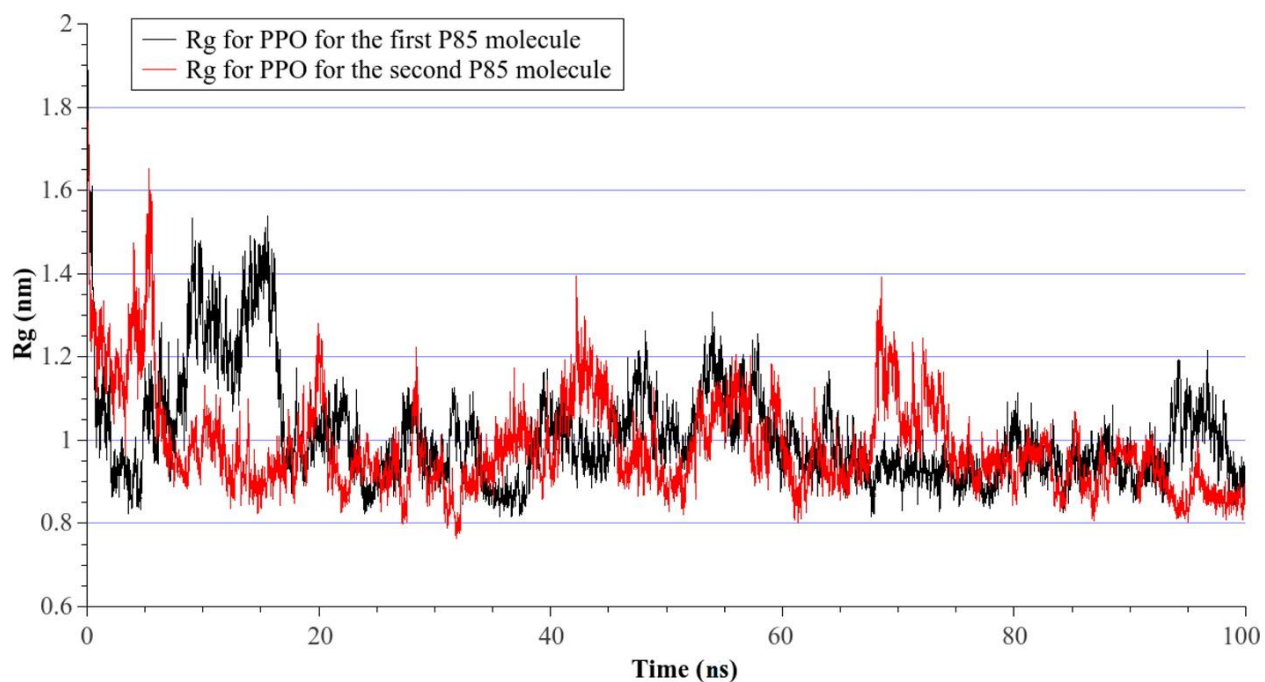


Figure 6.6: Radius of gyration of PPO block of P85 molecules at air/water interface. Data from the last 50 ns of the trajectory were used to calculate the average of Rg.

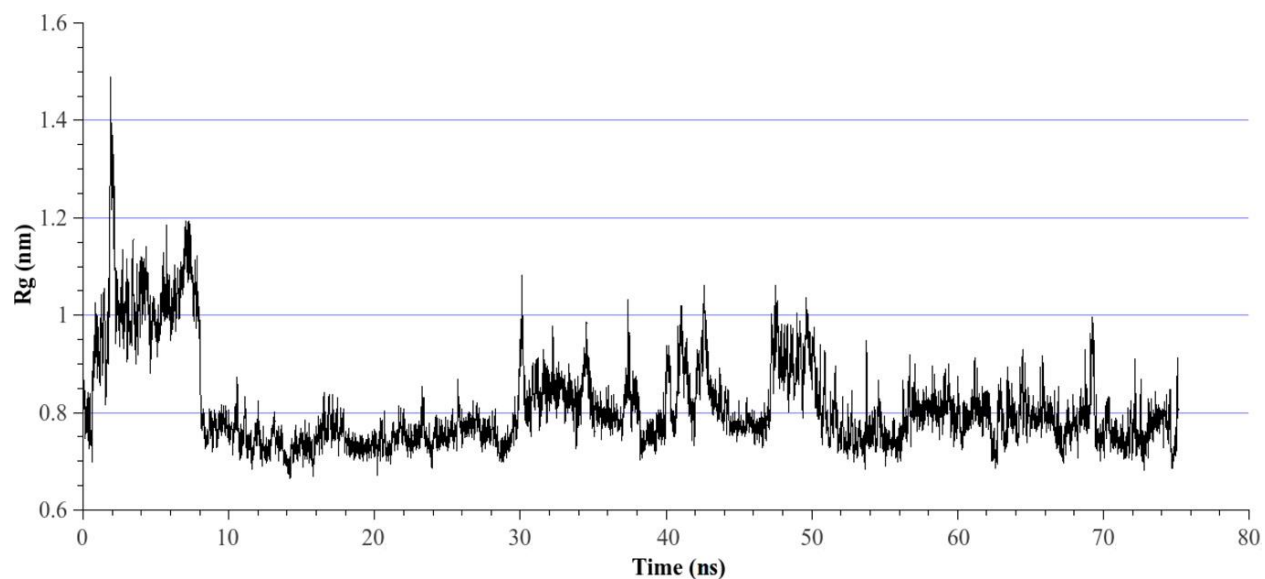


Figure 6.7: Radius of gyration of PPO block of the P188 molecule at the air/water interface. Data from the last 50 ns of the trajectory were used to calculate the average of Rg.

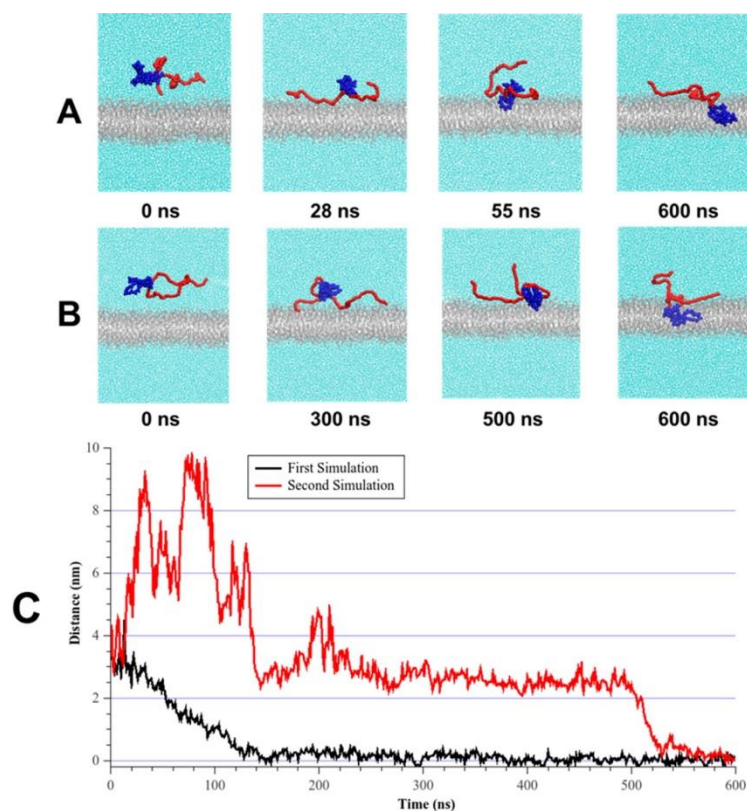


Figure 6.8: Interaction of P85 poloxamer with the DLPC model membrane. Panels A and B show the simulation cell used to study the interaction of P85 with the DLPC membrane. Two simulations were performed with different initial configurations of P85. The cyan background is water, the bilayer is color coded gray, hydrophobic part of P85 is blue and the hydrophilic tails are represented as red. (C) Progress in the permeation of the hydrophobic block of the poloxamer as a function of time. The plot displays the distance between the center of mass of the bilayer and the center of mass of the hydrophobic part of P85.

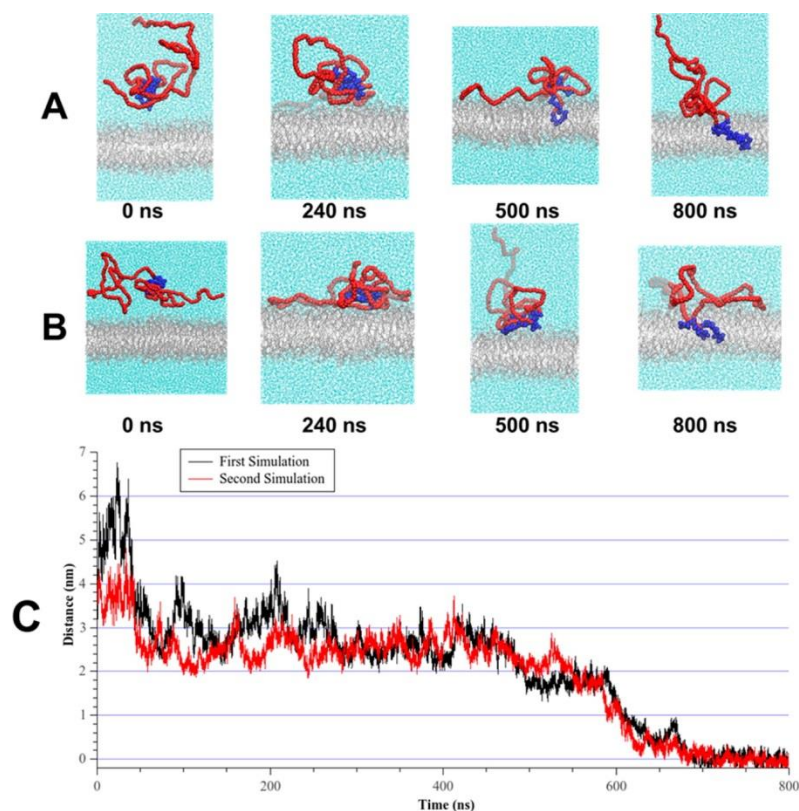


Figure 6.9: Interaction of P188 poloxamer with the DLPC model membrane. Panels A and B show the simulation cell used to study the interaction of P188 with the DLPC membrane. Two simulations were performed with different initial configurations of P188. The cyan background is water, the bilayer is color coded gray, hydrophobic part of P188 is blue, and the hydrophilic tails are represented as red. (C) Progress in the permeation of the hydrophobic block of poloxamer as a function of time. The plot displays the distance between the center of mass of the bilayer and the center of mass of the hydrophobic part of P188.

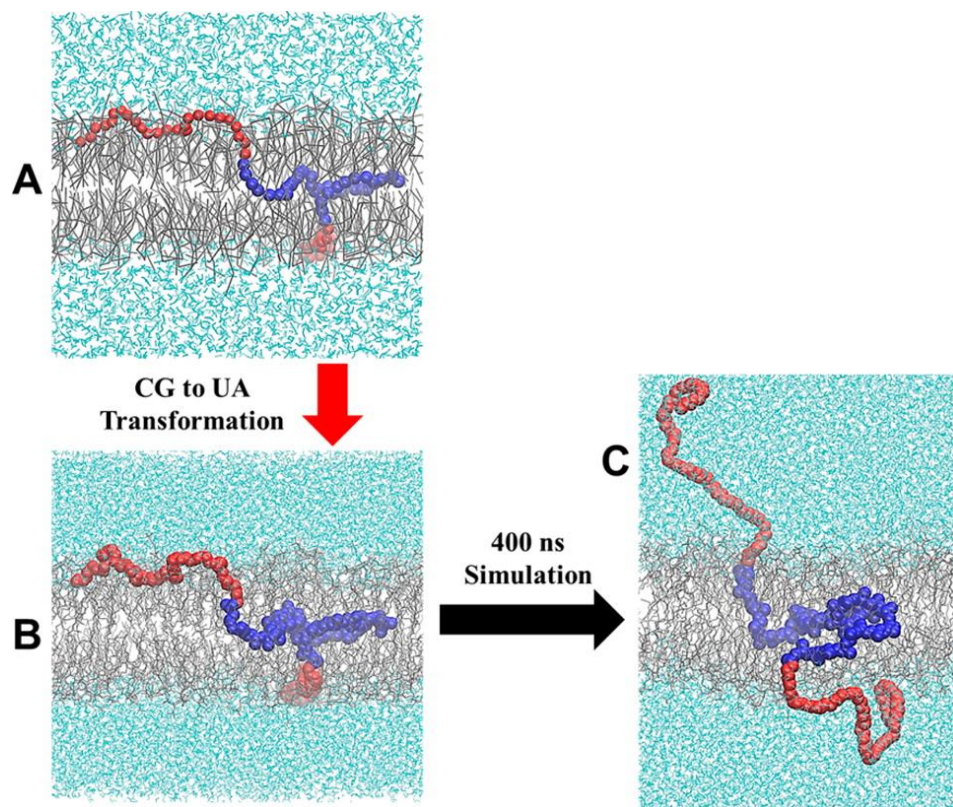


Figure 6.10: Self-assembly of P85 poloxamer, DLPC lipid monomers, and water molecules. (A) snapshot from a self-assembly simulation performed using a coarse-grained force-field. (B) The system after the transformation from coarse-grained resolution to a united-atom resolution. (C) The resulting configuration after 400 ns of simulation using united-atom force-field. In all panels, the cyan background is water, the bilayer is colored in gray, the hydrophobic block is shown by blue spheres, and the hydrophilic tails are presented in red.

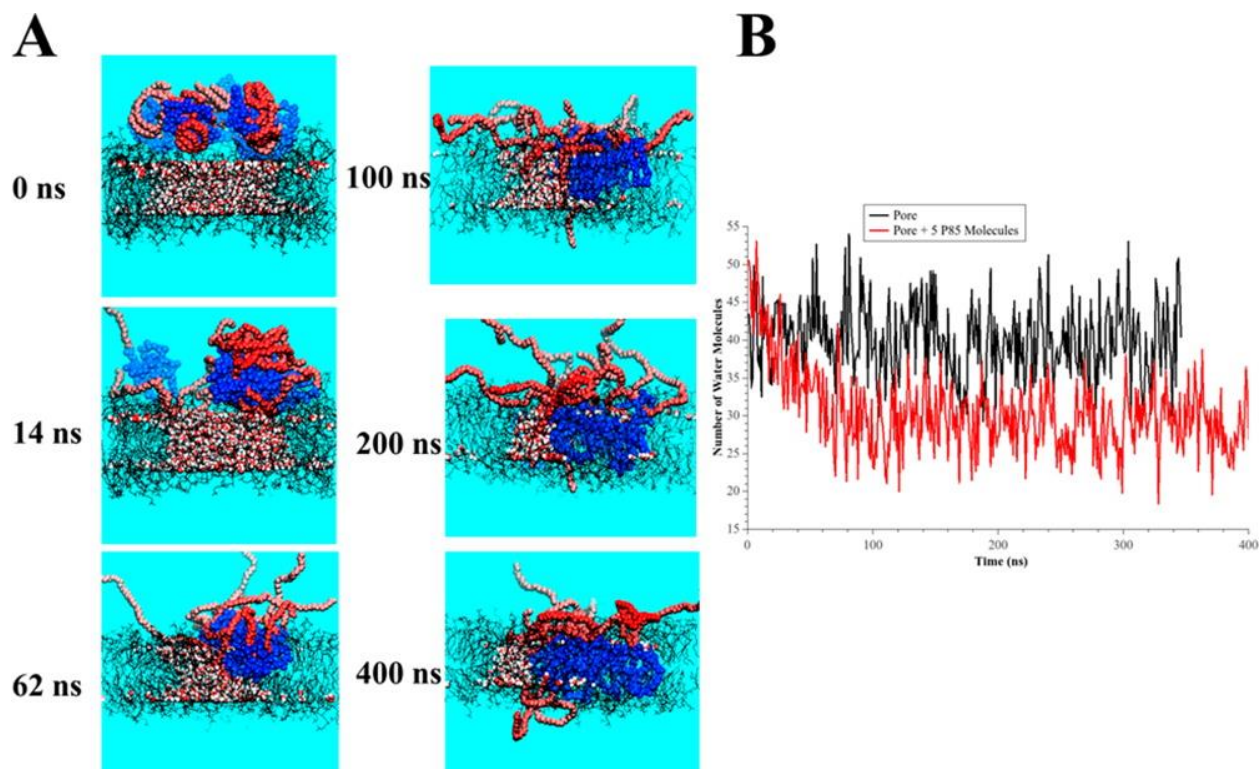


Figure 6.11: Interaction of five P85 poloxamers with a damaged DLPC model membrane. (A) Snapshots from the 400 ns simulation. Initially, five poloxamers were placed on the surface of DLPC membrane that had a pore (damaged membrane model). The cyan background is water; however, the water molecules that are in the pore are highlighted as red (oxygen) and white (hydrogen) spheres, the DLPC bilayer is shown as gray, the hydrophobic block of P85 molecules is presented in blue, and the hydrophilic tails are presented in red. (B) Number of water molecules in the middle of the bilayer as a function of time, during the 400 ns simulation run. The red curve is for the system containing poloxamers, while the black curve is for the system without poloxamers (control). For details of the measurements, refer to the Methods section.

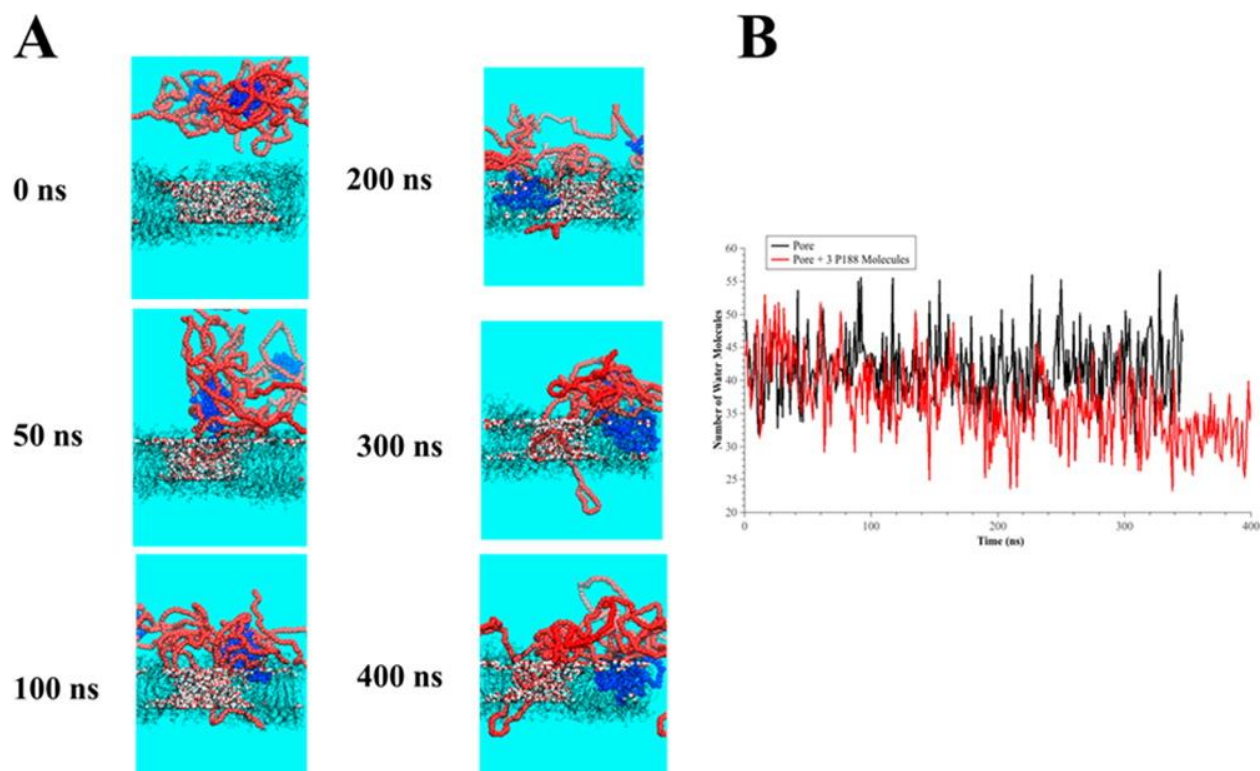


Figure 6.12: Interaction of three P188 poloxamers with damaged DLPC model membrane. (A) Snapshots from the 400 ns simulation. Initially, three poloxamers were placed on the surface of DLPC membrane that had a pore (damaged membrane model). The cyan background is water; however, the water molecules that are in the pore are highlighted as red (oxygen) and white (hydrogen) spheres, the DLPC bilayer is shown as gray, the hydrophobic block of P188 molecules is presented in blue, and the hydrophilic tails are presented in red. (B) Number of water molecules in the middle of the bilayer as a function of time, during the 400 ns simulation run. The red curve is for the system containing poloxamers, while the black curve is for the system without poloxamers (control). For details of the measurements refer to the Methods section.

Thesis conclusions and future directions

In this thesis we employed molecular dynamics computer simulations to study the integrity of lipid membranes when perturbed by cavitation (bubble collapse) or by interactions with antimicrobial peptides or with polymers. In all our investigations we provided molecular resolution pictures of the processes under study and tried to compare our findings with the experimental observations.

Our study of the antimicrobial peptides, as peptides that generate pores in the membrane, confirmed the experimental suggestions²⁵. We observed a difference in the amount of tension on the membrane produced by adsorbed magainin when compared to tension due to melittin. In addition, we studied in detail the tension profiles calculated using two different ensembles NPT and NP_zAT to understand what ensemble is more appropriate for simulations of the initial stage of poration. Since tension and curvature in the membrane are interconnected, further investigation of this connection and how antimicrobial peptides influence this connection is very desirable.

To understand the connection between the damage to neural cells and the traumatic brain injury (TBI) we studied the role of cavitation in membrane poration. We observed that poration of lipid membranes caused by an implosion of nanobubbles due to the interaction of an impinging shock wave is due to shear that is created by an inhomogeneous pressure on the membrane surface. In the pursuit of our further understanding of the TBI, we studied the damage to a model blood-brain barrier (BBB) due to cavitation phenomenon. Thus, for the very first time we constructed a simple model of a tight junction in (BBB) and studied the behavior of this tight junction under the impact of a shock wave induced bubble collapse. Future work needs

to be done using a more complex model of a tight junction that includes more proteins of different variety.

Our computational studies of membrane sealing polymers, such as poloxamers, were performed using two different resolutions: coarse-grained (CG) and united-atom (UA). We developed two sets of force-fields (united atom, UA, and coarse-grained, CG) to study membrane restoring properties of triblock copolymers (poloxamers). We observed similar results whether we used CG or UA representations and they were in line with experimental observations. The fact that we reached the same results using two different resolutions adds credibility to our parameter development. To extend further our work, investigations of the interactions of triblock copolymers with proteins, especially *p*-glycoproteins would be very desirable. Since our work provides a UA force-field for poloxamers, it can be used in future detailed studies of protein-poloxamer interactions. This research will provide benefits from both therapeutic and/or pharmaceutical perspectives.

REFERENCES

- (1) van Meer, G., Voelker, D. R., and Feigenson, G. W. (2008) Membrane lipids: where they are and how they behave. *Nat. Rev. Mol. Cell Biol.* 9, 112–24.
- (2) Pogliano, J., Pogliano, N., and Silverman, J. A. (2012) Daptomycin-mediated reorganization of membrane architecture causes mislocalization of essential cell division proteins. *J. Bacteriol.* 194, 4494–504.
- (3) Hof, H. (2006) A new, broad-spectrum azole antifungal: posaconazole--mechanisms of action and resistance, spectrum of activity. *Mycoses* 49 Suppl 1, 2–6.
- (4) Gambihler, S., and Delius, M. (1992) Transient increase in membrane permeability of L1210 cells upon exposure to lithotripter shock waves in vitro. *Naturwissenschaften* 79, 328–9.
- (5) Doukas, A. G., McAuliffe, D. J., and Flotte, T. J. (1993) Biological effects of laser-induced shock waves: structural and functional cell damage in vitro. *Ultrasound Med. Biol.* 19, 137–46.
- (6) Gambihler, S., Delius, M., and Ellwart, J. W. (1994) Permeabilization of the plasma membrane of L1210 mouse leukemia cells using lithotripter shock waves. *J. Membr. Biol.* 141, 267–75.
- (7) Delius, M., and Adams, G. (1999) Shock wave permeabilization with ribosome inactivating proteins: a new approach to tumor therapy. *Cancer Res.* 59, 5227–32.
- (8) Rosenthal, I., Sostaric, J. Z., and Riesz, P. (2004) Sonodynamic therapy—a review of the synergistic effects of drugs and ultrasound. *Ultrason. Sonochem.* 11, 349–363.
- (9) Rosenfeld, J. V., McFarlane, A. C., Bragge, P., Armonda, R. A., Grimes, J. B., and Ling, G. S. (2013) Blast-related traumatic brain injury. *Lancet. Neurol.* 12, 882–93.
- (10) Nagle, J. F., and Tristram-Nagle, S. (2000) Structure of lipid bilayers. *Biochim. Biophys. Acta - Rev. Biomembr.* 1469, 159–195.
- (11) Roduit, C., Longo, G., Dietler, G., and Kasas, S. (2015) Measuring Cytoskeleton and Cellular Membrane Mechanical Properties by Atomic Force Microscopy, pp 153–159.
- (12) Demchenko, A. P., Duportail, G., Oncul, S., Klymchenko, A. S., and Mély, Y. (2015) Introduction to Fluorescence Probing of Biological Membranes, pp 19–43.
- (13) Tyler, A. I. I., Clarke, J. A., Seddon, J. M., and Law, R. V. (2015) Solid State NMR of Lipid Model Membranes, pp 227–253.
- (14) Feller, S. E., and Pastor, R. W. (1999) Constant surface tension simulations of lipid bilayers: The sensitivity of surface areas and compressibilities. *J. Chem. Phys.* 111, 1281.
- (15) Shinoda, W., Shimizu, M., and Okazaki, S. (1998) Molecular Dynamics Study on

Electrostatic Properties of a Lipid Bilayer: Polarization, Electrostatic Potential, and the Effects on Structure and Dynamics of Water near the Interface. *J. Phys. Chem. B* 102, 6647–6654.

(16) Petrache, H. I., Tu, K., and Nagle, J. F. (1999) Analysis of Simulated NMR Order Parameters for Lipid Bilayer Structure Determination. *Biophys. J.* 76, 2479–2487.

(17) Nagle, J. F., Zhang, R., Tristram-Nagle, S., Sun, W., Petrache, H. I., and Suter, R. M. (1996) X-ray structure determination of fully hydrated L alpha phase dipalmitoylphosphatidylcholine bilayers. *Biophys. J.* 70, 1419–1431.

(18) Brooks, B. R., Bruccoleri, R. E., Olafson, B. D., States, D. J., Swaminathan, S., and Karplus, M. (1983) CHARMM: A program for macromolecular energy, minimization, and dynamics calculations. *J. Comput. Chem.* 4, 187–217.

(19) Case, D. A., Cheatham, T. E., Darden, T., Gohlke, H., Luo, R., Merz, K. M., Onufriev, A., Simmerling, C., Wang, B., and Woods, R. J. (2005) The Amber biomolecular simulation programs. *J. Comput. Chem.* 26, 1668–1688.

(20) Jorgensen, W. L., Maxwell, D. S., and Tirado-Rives, J. (1996) Development and Testing of the OPLS All-Atom Force Field on Conformational Energetics and Properties of Organic Liquids. *J. Am. Chem. Soc.* 118, 11225–11236.

(21) Scott, W. R. P., Hünenberger, P. H., Tironi, I. G., Mark, A. E., Billeter, S. R., Fennen, J., Torda, A. E., Huber, T., Krüger, P., and van Gunsteren, W. F. (1999) The GROMOS Biomolecular Simulation Program Package. *J. Phys. Chem. A* 103, 3596–3607.

(22) Marrink, S. J., Risselada, H. J., Yefimov, S., Tieleman, D. P., and de Vries, A. H. (2007) The MARTINI force field: coarse grained model for biomolecular simulations. *J. Phys. Chem. B* 111, 7812–24.

(23) Oostenbrink, C., Villa, A., Mark, A. E., and van Gunsteren, W. F. (2004) A biomolecular force field based on the free enthalpy of hydration and solvation: the GROMOS force-field parameter sets 53A5 and 53A6. *J. Comput. Chem.* 25, 1656–76.

(24) Lee, M.-T., Sun, T.-L., Hung, W.-C., and Huang, H. W. (2013) Process of inducing pores in membranes by melittin. *Proc. Natl. Acad. Sci. U. S. A.* 110, 14243–8.

(25) Tamba, Y., Ariyama, H., Levadny, V., and Yamazaki, M. (2010) Kinetic pathway of antimicrobial peptide magainin 2-induced pore formation in lipid membranes. *J. Phys. Chem. B* 114, 12018–26.

(26) De Cock, I., Zagato, E., Braeckmans, K., Luan, Y., de Jong, N., De Smedt, S. C., and Lentacker, I. (2014) Ultrasound and microbubble mediated drug delivery: Acoustic pressure as determinant for uptake via membrane pores or endocytosis. *J. Control. Release.*

(27) Deng, C. X., Sieling, F., Pan, H., and Cui, J. (2004) Ultrasound-induced cell membrane porosity. *Ultrasound Med. Biol.* 30, 519–26.

- (28) Hernot, S., and Klivanov, A. L. (2008) Microbubbles in ultrasound-triggered drug and gene delivery. *Adv. Drug Deliv. Rev.* 60, 1153–66.
- (29) Postema, M., van Wamel, A., Lancée, C. T., and de Jong, N. (2004) Ultrasound-induced encapsulated microbubble phenomena. *Ultrasound Med. Biol.* 30, 827–40.
- (30) Prentice, P., Cuschieri, A., Dholakia, K., Prausnitz, M., and Campbell, P. (2005) Membrane disruption by optically controlled microbubble cavitation. *Nat. Phys.* 1, 107–110.
- (31) Kobayashi, K., Kodama, T., and Takahira, H. (2011) Shock wave-bubble interaction near soft and rigid boundaries during lithotripsy: numerical analysis by the improved ghost fluid method. *Phys. Med. Biol.* 56, 6421–40.
- (32) Shetty, A. K., Mishra, V., Kodali, M., and Hattiangady, B. (2014) Blood brain barrier dysfunction and delayed neurological deficits in mild traumatic brain injury induced by blast shock waves. *Front. Cell. Neurosci.* 8, 232.
- (33) Treat, L. H., McDannold, N., Vykhodtseva, N., Zhang, Y., Tam, K., and Hynynen, K. (2007) Targeted delivery of doxorubicin to the rat brain at therapeutic levels using MRI-guided focused ultrasound. *Int. J. cancer* 121, 901–7.
- (34) McDannold, N., Vykhodtseva, N., Raymond, S., Jolesz, F. A., and Hynynen, K. (2005) MRI-guided targeted blood-brain barrier disruption with focused ultrasound: histological findings in rabbits. *Ultrasound Med. Biol.* 31, 1527–37.
- (35) Mesiwala, A. H., Farrell, L., Wenzel, H. J., Silbergeld, D. L., Crum, L. A., Winn, H. R., and Mourad, P. D. (2002) High-intensity focused ultrasound selectively disrupts the blood-brain barrier in vivo. *Ultrasound Med. Biol.* 28, 389–400.
- (36) Pereira, G. G., Dimer, F. A., Guterres, S. S., Kechinski, C. P., Granada, J. E., and Cardozo, N. S. M. (2013) Formulation and characterization of poloxamer 407®: thermoreversible gel containing polymeric microparticles and hyaluronic acid. *Quim. Nova* 36, 1121–1125.
- (37) Batrakova, E. V., and Kabanov, A. V. (2008) Pluronic block copolymers: evolution of drug delivery concept from inert nanocarriers to biological response modifiers. *J. Control. Release* 130, 98–106.
- (38) Shubhra, Q. T. H., Tóth, J., Gyenis, J., and Feczko, T. (2014) Poloxamers for Surface Modification of Hydrophobic Drug Carriers and Their Effects on Drug Delivery. *Polym. Rev.* 54, 112–138.
- (39) Wu, G., Frey, S. L., Maskarinec, S. A., and Lee, K. Y. C. (2006) Triblock Copolymer as an Effective Membrane-Sealing Material. *MRS Bull.* 31, pp. 532–535.
- (40) Maskarinec, S. A., Wu, G., and Lee, K. Y. C. (2005) Membrane sealing by polymers. *Ann. N. Y. Acad. Sci.* 1066, 310–20.
- (41) Alakhova, D. Y., and Kabanov, A. V. (2014) Pluronics and MDR reversal: an update. *Mol.*

Pharm. 11, 2566–78.

(42) Moloughney, J. G., and Weisleder, N. (2012) Poloxamer 188 (p188) as a membrane resealing reagent in biomedical applications. *Recent Pat. Biotechnol.* 6, 200–11.

(43) Winger, M., de Vries, A. H., and van Gunsteren, W. F. (2009) Force-field dependence of the conformational properties of α,ω -dimethoxypolyethylene glycol. *Mol. Phys.* 107, 1313–1321.

(44) Wimley, W. C., and Hristova, K. (2011) Antimicrobial peptides: successes, challenges and unanswered questions. *J. Membr. Biol.* 239, 27–34.

(45) Wimley, W. C. (2010) Describing the mechanism of antimicrobial peptide action with the interfacial activity model. *ACS Chem. Biol.* 5, 905–17.

(46) Sato, H., and Feix, J. B. (2006) Peptide-membrane interactions and mechanisms of membrane destruction by amphipathic alpha-helical antimicrobial peptides. *Biochim. Biophys. Acta* 1758, 1245–56.

(47) Brogden, K. A. (2005) Antimicrobial peptides: pore formers or metabolic inhibitors in bacteria? *Nat. Rev. Microbiol.* 3, 238–50.

(48) Almeida, P. F., and Pokorny, A. (2009) Mechanisms of antimicrobial, cytolytic, and cell-penetrating peptides: from kinetics to thermodynamics. *Biochemistry* 48, 8083–93.

(49) Tamba, Y., and Yamazaki, M. (2009) Magainin 2-induced pore formation in the lipid membranes depends on its concentration in the membrane interface. *J. Phys. Chem. B* 113, 4846–52.

(50) Santo, K. P., Irudayam, S. J., and Berkowitz, M. L. (2013) Melittin creates transient pores in a lipid bilayer: results from computer simulations. *J. Phys. Chem. B* 117, 5031–42.

(51) Li, Y., and Guo, H. (2012) Atomistic simulations of an antimicrobial molecule interacting with a model bacterial membrane. *Theor. Chem. Acc.* 132, 1303.

(52) Irudayam, S. J., Pobandt, T., and Berkowitz, M. L. (2013) Free energy barrier for melittin reorientation from a membrane-bound state to a transmembrane state. *J. Phys. Chem. B* 117, 13457–63.

(53) Horn, J. N., Romo, T. D., and Grossfield, A. (2013) Simulating the mechanism of antimicrobial lipopeptides with all-atom molecular dynamics. *Biochemistry* 52, 5604–10.

(54) Parton, D. L., Akhmatskaya, E. V., and Sansom, M. S. P. (2012) Multiscale simulations of the antimicrobial peptide maculatin 1.1: water permeation through disordered aggregates. *J. Phys. Chem. B* 116, 8485–93.

(55) Mihajlovic, M., and Lazaridis, T. (2012) Charge distribution and imperfect amphipathicity affect pore formation by antimicrobial peptides. *Biochim. Biophys. Acta* 1818, 1274–83.

- (56) Woo, H.-J., and Wallqvist, A. (2011) Spontaneous buckling of lipid bilayer and vesicle budding induced by antimicrobial peptide magainin 2: a coarse-grained simulation study. *J. Phys. Chem. B* 115, 8122–9.
- (57) Irudayam, S. J., and Berkowitz, M. L. (2011) Influence of the arrangement and secondary structure of melittin peptides on the formation and stability of toroidal pores. *Biochim. Biophys. Acta* 1808, 2258–66.
- (58) Mihajlovic, M., and Lazaridis, T. (2010) Antimicrobial peptides in toroidal and cylindrical pores. *Biochim. Biophys. Acta* 1798, 1485–93.
- (59) Manna, M., and Mukhopadhyay, C. (2009) Cause and effect of melittin-induced pore formation: a computational approach. *Langmuir* 25, 12235–42.
- (60) Vivcharuk, V., Tomberli, B., Tolokh, I. S., and Gray, C. G. (2008) Prediction of binding free energy for adsorption of antimicrobial peptide lactoferricin B on a POPC membrane. *Phys. Rev. E. Stat. Nonlin. Soft Matter Phys.* 77, 031913.
- (61) Sengupta, D., Leontiadou, H., Mark, A. E., and Marrink, S.-J. (2008) Toroidal pores formed by antimicrobial peptides show significant disorder. *Biochim. Biophys. Acta* 1778, 2308–17.
- (62) Mátyus, E., Kandt, C., and Tieleman, D. P. (2007) Computer simulation of antimicrobial peptides. *Curr. Med. Chem.* 14, 2789–98.
- (63) Leontiadou, H., Mark, A. E., and Marrink, S. J. (2006) Antimicrobial peptides in action. *J. Am. Chem. Soc.* 128, 12156–61.
- (64) Chen, F.-Y., Lee, M.-T., and Huang, H. W. (2003) Evidence for membrane thinning effect as the mechanism for peptide-induced pore formation. *Biophys. J.* 84, 3751–8.
- (65) de Jong, D. H., Singh, G., Bennett, W. F. D., Arnarez, C., Wassenaar, T. A., Schäfer, L. V., Periole, X., Tieleman, D. P., and Marrink, S. J. (2013) Improved Parameters for the Martini Coarse-Grained Protein Force Field. *J. Chem. Theory Comput.* 9, 687–697.
- (66) Yesylevskyy, S. O., Schäfer, L. V., Sengupta, D., and Marrink, S. J. (2010) Polarizable water model for the coarse-grained MARTINI force field. *PLoS Comput. Biol.* (Levitt, M., Ed.) 6, e1000810.
- (67) Hess, B., Kutzner, C., van der Spoel, D., and Lindahl, E. (2008) GROMACS 4: Algorithms for Highly Efficient, Load-Balanced, and Scalable Molecular Simulation. *J. Chem. Theory Comput.* 4, 435–447.
- (68) Berendsen, H. J. C., Postma, J. P. M., van Gunsteren, W. F., DiNola, A., and Haak, J. R. (1984) Molecular dynamics with coupling to an external bath. *J. Chem. Phys.* 81, 3684.
- (69) Tironi, I. G., Sperb, R., Smith, P. E., and van Gunsteren, W. F. (1995) A generalized reaction field method for molecular dynamics simulations. *J. Chem. Phys.* 102, 5451.

- (70) Terwilliger, T. C., and Eisenberg, D. (1982) The structure of melittin. I. Structure determination and partial refinement. *J. Biol. Chem.* 257, 6010–6015.
- (71) Terwilliger, T. C., and Eisenberg, D. (1982) The structure of melittin. II. Interpretation of the structure. *J. Biol. Chem.* 257, 6016–22.
- (72) Raghuraman, H., and Chattopadhyay, A. (2007) Melittin: a membrane-active peptide with diverse functions. *Biosci. Rep.* 27, 189–223.
- (73) Monticelli, L., Kandasamy, S. K., Periole, X., Larson, R. G., Tieleman, D. P., and Marrink, S.-J. (2008) The MARTINI Coarse-Grained Force Field: Extension to Proteins. *J. Chem. Theory Comput.* 4, 819–834.
- (74) Gesell, J., Zasloff, M., and Opella, S. J. (1997) Two-dimensional ^1H NMR experiments show that the 23-residue magainin antibiotic peptide is an α -helix in dodecylphosphocholine micelles, sodium dodecylsulfate micelles, and trifluoroethanol/water solution. *J. Biomol. NMR* 9, 127–35.
- (75) Schrodinger LLC. (2010) The PyMOL Molecular Graphics System, Version 1.3r1.
- (76) Vanegas, J. M., Torres-Sánchez, A., and Arroyo, M. (2014) Importance of Force Decomposition for Local Stress Calculations in Biomembrane Molecular Simulations. *J. Chem. Theory Comput.* 10, 691–702.
- (77) Ollila, O., Risselada, H., Louhivuori, M., Lindahl, E., Vattulainen, I., and Marrink, S. (2009) 3D Pressure Field in Lipid Membranes and Membrane-Protein Complexes. *Phys. Rev. Lett.* 102, 078101.
- (78) Humphrey, W., Dalke, A., and Schulten, K. (1996) VMD: Visual molecular dynamics. *J. Mol. Graph.* 14, 33–38.
- (79) Choubey, A., Vedadi, M., Nomura, K., Kalia, R. K., Nakano, A., and Vashishta, P. (2011) Poration of lipid bilayers by shock-induced nanobubble collapse. *Appl. Phys. Lett.* 98, 023701.
- (80) Kodama, T., Hamblin, M. R., and Doukas, A. G. (2000) Cytoplasmic molecular delivery with shock waves: importance of impulse. *Biophys. J.* 79, 1821–32.
- (81) Koshiyama, K., Kodama, T., Yano, T., and Fujikawa, S. (2006) Structural change in lipid bilayers and water penetration induced by shock waves: molecular dynamics simulations. *Biophys. J.* 91, 2198–205.
- (82) Mediavilla Varas, J., Philippens, M., Meijer, S. R., van den Berg, A. C., Sibma, P. C., van Bree, J. L. M. J., and de Vries, D. V. W. M. (2011) Physics of IED Blast Shock Tube Simulations for mTBI Research. *Front. Neurol.* 2, 58.
- (83) Santo, K. P., and Berkowitz, M. L. (2014) Shock wave interaction with a phospholipid membrane: coarse-grained computer simulations. *J. Chem. Phys.* 140, 054906.

- (84) Steinhauser, M. O., and Schmidt, M. (2014) Destruction of cancer cells by laser-induced shock waves: recent developments in experimental treatments and multiscale computer simulations. *Soft Matter* 10, 4778–88.
- (85) Nakagawa, A., Manley, G. T., Gean, A. D., Ohtani, K., Armonda, R., Tsukamoto, A., Yamamoto, H., Takayama, K., and Tominaga, T. (2011) Mechanisms of primary blast-induced traumatic brain injury: insights from shock-wave research. *J. Neurotrauma* 28, 1101–19.
- (86) Espinosa, S., Asproulis, N., and Drikakis, D. (2013) Chemotherapy efficiency increase via shock wave interaction with biological membranes: a molecular dynamics study. *Microfluid. Nanofluidics* 16, 613–622.
- (87) Afadzi, M., Strand, S. P., Nilssen, E. A., Måsøy, S.-E., Johansen, T. F., Hansen, R., Angelsen, B. A., and de L Davies, C. (2013) Mechanisms of the ultrasound-mediated intracellular delivery of liposomes and dextrans. *IEEE Trans. Ultrason. Ferroelectr. Freq. Control* 60, 21–33.
- (88) Ahmed, S. E., Martins, A. M., and Hussein, G. A. (2014) The use of ultrasound to release chemotherapeutic drugs from micelles and liposomes.
- (89) Arun, P., Abu-Taleb, R., Oguntayo, S., Tanaka, M., Wang, Y., Valiyaveetil, M., Long, J. B., Zhang, Y., and Nambiar, M. P. (2013) Distinct patterns of expression of traumatic brain injury biomarkers after blast exposure: role of compromised cell membrane integrity. *Neurosci. Lett.* 552, 87–91.
- (90) Horie, S., Watanabe, Y., Chen, R., Mori, S., Matsumura, Y., and Kodama, T. (2010) Development of localized gene delivery using a dual-intensity ultrasound system in the bladder. *Ultrasound Med. Biol.* 36, 1867–75.
- (91) Hussein, G. A., Pitt, W. G., and Martins, A. M. (2014) Ultrasonically triggered drug delivery: breaking the barrier. *Colloids Surf. B. Biointerfaces* 123, 364–86.
- (92) Ng, K., and Liu, Y. (2002) Therapeutic ultrasound: its application in drug delivery. *Med. Res. Rev.* 22, 204–23.
- (93) Panzer, M. B., Matthews, K. A., Yu, A. W., Morrison, B., Meaney, D. F., and Bass, C. R. (2012) A Multiscale Approach to Blast Neurotrauma Modeling: Part I - Development of Novel Test Devices for in vivo and in vitro Blast Injury Models. *Front. Neurol.* 3, 46.
- (94) Ravin, R., Blank, P. S., Steinkamp, A., Rappaport, S. M., Ravin, N., Bezrukov, L., Guerrero-Cazares, H., Quinones-Hinojosa, A., Bezrukov, S. M., and Zimmerberg, J. (2012) Shear forces during blast, not abrupt changes in pressure alone, generate calcium activity in human brain cells. *PLoS One* (Barnes, S., Ed.) 7, e39421.
- (95) Slonberg, Y., and Chantawansri, T. (2014) Damage in spherical cellular membrane generated by the shock waves: Coarse-grained molecular dynamics simulation of lipid vesicle. *J. Chem. Phys.* 141, 184904.

- (96) Lentacker, I., De Cock, I., Deckers, R., De Smedt, S. C., and Moonen, C. T. W. (2014) Understanding ultrasound induced sonoporation: definitions and underlying mechanisms. *Adv. Drug Deliv. Rev.* 72, 49–64.
- (97) Qiu, Y., Luo, Y., Zhang, Y., Cui, W., Zhang, D., Wu, J., Zhang, J., and Tu, J. (2010) The correlation between acoustic cavitation and sonoporation involved in ultrasound-mediated DNA transfection with polyethylenimine (PEI) in vitro. *J. Control. Release* 145, 40–8.
- (98) Ohl, C.-D., Arora, M., Ikink, R., de Jong, N., Versluis, M., Delius, M., and Lohse, D. (2006) Sonoporation from jetting cavitation bubbles. *Biophys. J.* 91, 4285–95.
- (99) KODAMA, T., TOMITA, Y., WATANABE, Y., KOSHIYAMA, K., YANO, T., and FUJIKAWA, S. (2009) Cavitation Bubbles Mediated Molecular Delivery During Sonoporation. *J. Biomech. Sci. Eng.* 4, 124–140.
- (100) Santo, K. P., and Berkowitz, M. L. (2014) Shock Wave Induced Collapse of Arrays of Nanobubbles Located Next to a Lipid Membrane: Coarse-Grained Computer Simulations. *J. Phys. Chem. B* DOI: 10.1021/jp505720d.
- (101) Attard, P. (2013) The stability of nanobubbles. *Eur. Phys. J. Spec. Top.* 1–22.
- (102) Borkent, B., Dammer, S., Schönherr, H., Vancso, G., and Lohse, D. (2007) Superstability of Surface Nanobubbles. *Phys. Rev. Lett.* 98, 204502.
- (103) Craig, V. S. J. (2011) Very small bubbles at surfaces—the nanobubble puzzle. *Soft Matter* 7, 40.
- (104) Lukianova-Hleb, E. Y., Ren, X., Sawant, R. R., Wu, X., Torchilin, V. P., and Lapotko, D. O. (2014) On-demand intracellular amplification of chemoradiation with cancer-specific plasmonic nanobubbles. *Nat. Med.* 20, 778–84.
- (105) Weijs, J., and Lohse, D. (2013) Why Surface Nanobubbles Live for Hours. *Phys. Rev. Lett.* 110, 054501.
- (106) Attard, P., Moody, M. P., and Tyrrell, J. W. G. (2002) Nanobubbles: the big picture. *Phys. A Stat. Mech. its Appl.* 314, 696–705.
- (107) Van Der Spoel, D., Lindahl, E., Hess, B., Groenhof, G., Mark, A. E., and Berendsen, H. J. C. (2005) GROMACS: fast, flexible, and free. *J. Comput. Chem.* 26, 1701–18.
- (108) Lindahl, E., Hess, B., and Spoel, D. van der. (2001) GROMACS 3.0: a package for molecular simulation and trajectory analysis. *Mol. Model. Annu.* 7, 306–317.
- (109) Berendsen, H. J. C., van der Spoel, D., and van Drunen, R. (1995) GROMACS: A message-passing parallel molecular dynamics implementation. *Comput. Phys. Commun.* 91, 43–56.
- (110) Marrink, S. J., de Vries, A. H., and Mark, A. E. (2004) Coarse Grained Model for

Semiquantitative Lipid Simulations. *J. Phys. Chem. B* 108, 750–760.

(111) Vedadi, M., Choubey, A., Nomura, K., Kalia, R. K., Nakano, A., Vashishta, P., and van Duin, A. C. T. (2010) Structure and Dynamics of Shock-Induced Nanobubble Collapse in Water. *Phys. Rev. Lett.* 105, 014503.

(112) Nomura, K.-I., Kalia, R. K., Nakano, A., Vashishta, P., van Duin, A. C. T., and Goddard, W. A. (2007) Dynamic transition in the structure of an energetic crystal during chemical reactions at shock front prior to detonation. *Phys. Rev. Lett.* 99, 148303.

(113) Zhao, Y.-Z., Du, L.-N., Lu, C.-T., Jin, Y.-G., and Ge, S.-P. (2013) Potential and problems in ultrasound-responsive drug delivery systems. *Int. J. Nanomedicine* 8, 1621–33.

(114) Liu, H.-L., Fan, C.-H., Ting, C.-Y., and Yeh, C.-K. (2014) Combining microbubbles and ultrasound for drug delivery to brain tumors: current progress and overview. *Theranostics* 4, 432–44.

(115) Sheikov, N., McDannold, N., Vykhodtseva, N., Jolesz, F., and Hynynen, K. (2004) Cellular mechanisms of the blood-brain barrier opening induced by ultrasound in presence of microbubbles. *Ultrasound Med. Biol.* 30, 979–89.

(116) Vykhodtseva, N., McDannold, N., and Hynynen, K. (2008) Progress and problems in the application of focused ultrasound for blood-brain barrier disruption. *Ultrasonics* 48, 279–96.

(117) Liu, H.-L., Hua, M.-Y., Chen, P.-Y., Chu, P.-C., Pan, C.-H., Yang, H.-W., Huang, C.-Y., Wang, J.-J., Yen, T.-C., and Wei, K.-C. (2010) Blood-brain barrier disruption with focused ultrasound enhances delivery of chemotherapeutic drugs for glioblastoma treatment. *Radiology* 255, 415–25.

(118) McDannold, N., Arvanitis, C. D., Vykhodtseva, N., and Livingstone, M. S. (2012) Temporary disruption of the blood-brain barrier by use of ultrasound and microbubbles: safety and efficacy evaluation in rhesus macaques. *Cancer Res.* 72, 3652–63.

(119) Shlosberg, D., Benifla, M., Kaufer, D., and Friedman, A. (2010) Blood–brain barrier breakdown as a therapeutic target in traumatic brain injury. *Nat. Rev. Neurol.* 6, 393–403.

(120) Hue, C. D., Cao, S., Haider, S. F., Vo, K. V., Effgen, G. B., Vogel, E., Panzer, M. B., Bass, C. R. D., Meaney, D. F., and Morrison, B. (2013) Blood-brain barrier dysfunction after primary blast injury in vitro. *J. Neurotrauma* 30, 1652–63.

(121) Abdul-Muneer, P. M., Schuetz, H., Wang, F., Skotak, M., Jones, J., Gorantla, S., Zimmerman, M. C., Chandra, N., and Haorah, J. (2013) Induction of oxidative and nitrosative damage leads to cerebrovascular inflammation in an animal model of mild traumatic brain injury induced by primary blast. *Free Radic. Biol. Med.* 60, 282–91.

(122) Yeoh, S., Bell, E. D., and Monson, K. L. (2013) Distribution of blood-brain barrier disruption in primary blast injury. *Ann. Biomed. Eng.* 41, 2206–14.

- (123) Cho, H. J., Sajja, V. S. S. S., VandeVord, P. J., and Lee, Y. W. (2013) Blast induces oxidative stress, inflammation, neuronal loss and subsequent short-term memory impairment in rats. *Neuroscience* 253, 9–20.
- (124) Tompkins, P., Tesiram, Y., Lerner, M., Gonzalez, L. P., Lightfoot, S., Rabb, C. H., and Brackett, D. J. (2013) Brain injury: neuro-inflammation, cognitive deficit, and magnetic resonance imaging in a model of blast induced traumatic brain injury. *J. Neurotrauma* 30, 1888–97.
- (125) Del Razo, M. J., Morofuji, Y., Meabon, J. S., Huber, B. R., Peskind, E. R., Banks, W. A., Mourad, P. D., Leveque, R. J., and Cook, D. G. (2015) Computational and in vitro studies of blast-induced blood-brain barrier disruption arXiv:1503.09157.
- (126) Warshel, A. (2002) Molecular Dynamics Simulations of Biological Reactions. *Acc. Chem. Res.* 35, 385–395.
- (127) Karplus, M., and Kuriyan, J. (2005) Molecular dynamics and protein function. *Proc. Natl. Acad. Sci.* 102, 6679–6685.
- (128) Adcock, S. A., and McCammon, J. A. (2006) Molecular dynamics: survey of methods for simulating the activity of proteins. *Chem. Rev.* 106, 1589–615.
- (129) Dodson, G. G., Lane, D. P., and Verma, C. S. (2008) Molecular simulations of protein dynamics: new windows on mechanisms in biology. *EMBO Rep.* 9, 144–50.
- (130) Marrink, S. J., and Tieleman, D. P. (2013) Perspective on the Martini model. *Chem. Soc. Rev.* 42, 6801–22.
- (131) Santo, K. P., and Berkowitz, M. L. (2012) Difference between magainin-2 and melittin assemblies in phosphatidylcholine bilayers: results from coarse-grained simulations. *J. Phys. Chem. B* 116, 3021–30.
- (132) Goliaei, A., Santo, K. P., and Berkowitz, M. L. (2014) Local Pressure Changes in Lipid Bilayers Due to Adsorption of Melittin and Magainin-h2 Antimicrobial Peptides: Results from Computer Simulations. *J. Phys. Chem. B* 118, 12673–12679.
- (133) Adhikari, U., Goliaei, A., and Berkowitz, M. L. (2015) Mechanism of Membrane Poration by Shock Wave Induced Nanobubble Collapse: A Molecular Dynamics Study. *J. Phys. Chem. B* 119, 6225–6234.
- (134) Suzuki, H., Nishizawa, T., Tani, K., Yamazaki, Y., Tamura, A., Ishitani, R., Dohmae, N., Tsukita, S., Nureki, O., and Fujiyoshi, Y. (2014) Crystal structure of a claudin provides insight into the architecture of tight junctions. *Science* 344, 304–7.
- (135) Krause, G., Winkler, L., Mueller, S. L., Haseloff, R. F., Piontek, J., and Blasig, I. E. (2008) Structure and function of claudins. *Biochim. Biophys. Acta* 1778, 631–45.
- (136) Haseloff, R. F., Dithmer, S., Winkler, L., Wolburg, H., and Blasig, I. E. (2015)

Transmembrane proteins of the tight junctions at the blood–brain barrier: Structural and functional aspects. *Semin. Cell Dev. Biol.* 38, 16–25.

(137) Tribello, G. A., Bonomi, M., Branduardi, D., Camilloni, C., and Bussi, G. (2014) PLUMED 2: New feathers for an old bird. *Comput. Phys. Commun.* 185, 604–613.

(138) Zhao, Y., Alakhova, D. Y., Kim, J. O., Bronich, T. K., and Kabanov, A. V. (2013) A simple way to enhance Doxil® therapy: drug release from liposomes at the tumor site by amphiphilic block copolymer. *J. Control. Release* 168, 61–9.

(139) Spurney, C. F., Guerron, A. D., Yu, Q., Sali, A., van der Meulen, J. H., Hoffman, E. P., and Nagaraju, K. (2011) Membrane sealant Poloxamer P188 protects against isoproterenol induced cardiomyopathy in dystrophin deficient mice. *BMC Cardiovasc. Disord.* 11, 20.

(140) Wu, G., Majewski, J., Ege, C., Kjaer, K., Weygand, M. J., and Lee, K. Y. C. (2005) Interaction between lipid monolayers and poloxamer 188: an X-ray reflectivity and diffraction study. *Biophys. J.* 89, 3159–73.

(141) Maskarinec, S. A., Hannig, J., Lee, R. C., and Lee, K. Y. C. (2002) Direct observation of poloxamer 188 insertion into lipid monolayers. *Biophys. J.* 82, 1453–9.

(142) Sharma, V., Stebe, K., Murphy, J. C., and Tung, L. (1996) Poloxamer 188 decreases susceptibility of artificial lipid membranes to electroporation. *Biophys. J.* 71, 3229–41.

(143) Frey, S. L., and Lee, K. Y. C. (2007) Temperature dependence of poloxamer insertion into and squeeze-out from lipid monolayers. *Langmuir* 23, 2631–7.

(144) Wu, G., Majewski, J., Ege, C., Kjaer, K., Weygand, M. J., and Lee, K. Y. C. (2004) Lipid corralling and poloxamer squeeze-out in membranes. *Phys. Rev. Lett.* 93, 028101.

(145) Nawaz, S., Redhead, M., Mantovani, G., Alexander, C., Bosquillon, C., and Carbone, P. (2012) Interactions of PEO–PPO–PEO block copolymers with lipid membranes: a computational and experimental study linking membrane lysis with polymer structure. *Soft Matter* 8, 6744.

(146) Hezaveh, S., Samanta, S., De Nicola, A., Milano, G., and Roccatano, D. (2012) Understanding the interaction of block copolymers with DMPC lipid bilayer using coarse-grained molecular dynamics simulations. *J. Phys. Chem. B* 116, 14333–45.

(147) Panizon, E., Bochicchio, D., Monticelli, L., and Rossi, G. (2015) MARTINI Coarse-Grained Models of Polyethylene and Polypropylene. *J. Phys. Chem. B* 119, 8209–8216.

(148) Rossi, G., Fuchs, P. F. J., Barnoud, J., and Monticelli, L. (2012) A coarse-grained MARTINI model of polyethylene glycol and of polyoxyethylene alkyl ether surfactants. *J. Phys. Chem. B* 116, 14353–62.

(149) Lee, H., de Vries, A. H., Marrink, S.-J., and Pastor, R. W. (2009) A coarse-grained model for polyethylene oxide and polyethylene glycol: conformation and hydrodynamics. *J. Phys. Chem. B* 113, 13186–94.

- (150) Hatakeyama, M., and Faller, R. (2007) Coarse-grained simulations of ABA amphiphilic triblock copolymer solutions in thin films. *Phys. Chem. Chem. Phys.* 9, 4662–72.
- (151) Nawaz, S., and Carbone, P. (2014) Coarse-graining poly(ethylene oxide)-poly(propylene oxide)-poly(ethylene oxide) (PEO-PPO-PEO) block copolymers using the MARTINI force field. *J. Phys. Chem. B* 118, 1648–59.
- (152) MORTENSEN, K. (1993) PEO-PPO-PEO triblock copolymer in aqueous solution. Micelle formation and crystallization. *Le J. Phys. IV* 03, C8–157–C8–160.
- (153) Hammouda, B. (2010) SANS from Pluronic P85 in d-water. *Eur. Polym. J.* 46, 2275–2281.
- (154) Zhou, Z., and Chu, B. (1988) Light-scattering study on the association behavior of triblock polymers of ethylene oxide and propylene oxide in aqueous solution. *J. Colloid Interface Sci.* 126, 171–180.
- (155) Bharatiya, B., Aswal, V. K., and Bahadur, P. (2009) Small angle neutron scattering study on the aggregation behaviour of PEO-PPO-PEO copolymers in the presence of a hydrophobic diol. *Pramana* 71, 1009–1013.
- (156) Borbély, S. (1997) Small-angle neutron scattering study of Pluronic F68 tri-block copolymer solutions. *Phys. B Condens. Matter* 241-243, 1016–1018.
- (157) Gelbart, W. M., Ben-Shaul, A., and Roux, D. (Eds.). (1994) Micelles, Membranes, Microemulsions, and Monolayers. Springer New York, New York, NY.
- (158) Bussi, G., Donadio, D., and Parrinello, M. (2007) Canonical sampling through velocity rescaling. *J. Chem. Phys.* 126, 014101.
- (159) Parrinello, M., and Rahman, A. (1981) Polymorphic transitions in single crystals: A new molecular dynamics method. *J. Appl. Phys.* 52, 7182.
- (160) Nosé, S., and Klein, M. L. (2006) Constant pressure molecular dynamics for molecular systems. *Mol. Phys.* 50, 1055–1076.
- (161) Kabanov, A. V., Nazarova, I. R., Astafieva, I. V., Batrakova, E. V., Alakhov, V. Y., Yaroslavov, A. A., and Kabanov, V. A. Micelle Formation and Solubilization of Fluorescent Probes in Poly(oxyethylene-b-oxypropylene-b-oxyethylene) Solutions. *Macromolecules* 28, 2303–2314.
- (162) Wassenaar, T. A., Ingólfsson, H. I., Böckmann, R. A., Tieleman, D. P., and Marrink, S. J. (2015) Computational Lipidomics with insane: A Versatile Tool for Generating Custom Membranes for Molecular Simulations. *J. Chem. Theory Comput.* 11, 2144–55.
- (163) Patterson, J. P., Robin, M. P., Chassenieux, C., Colombani, O., and O'Reilly, R. K. (2014) The analysis of solution self-assembled polymeric nanomaterials. *Chem. Soc. Rev.* 43, 2412–25.
- (164) MacKerell, A. D. (1995) Molecular Dynamics Simulation Analysis of a Sodium Dodecyl

Sulfate Micelle in Aqueous Solution: Decreased Fluidity of the Micelle Hydrocarbon Interior. *J. Phys. Chem.* 99, 1846–1855.

(165) Salaniwal, S., Cui, S. T., Cochran, H. D., and Cummings, P. T. (2001) Molecular Simulation of a Dichain Surfactant/Water/Carbon Dioxide System. 1. Structural Properties of Aggregates. *Langmuir* 17, 1773–1783.

(166) Bruce, C. D., Berkowitz, M. L., Perera, L., and Forbes, M. D. E. (2002) Molecular Dynamics Simulation of Sodium Dodecyl Sulfate Micelle in Water: Micellar Structural Characteristics and Counterion Distribution. *J. Phys. Chem. B* 106, 3788–3793.

(167) Bennett, W. F. D., and Tieleman, D. P. (2011) Water Defect and Pore Formation in Atomistic and Coarse-Grained Lipid Membranes: Pushing the Limits of Coarse Graining. *J. Chem. Theory Comput.* 7, 2981–2988.

(168) Bennett, W. F. D., Sapay, N., and Tieleman, D. P. (2014) Atomistic simulations of pore formation and closure in lipid bilayers. *Biophys. J.* 106, 210–9.

(169) Alexandridis, P., and Alan Hatton, T. (1995) Poly(ethylene oxide)-poly(propylene oxide)-poly(ethylene oxide) block copolymer surfactants in aqueous solutions and at interfaces: thermodynamics, structure, dynamics, and modeling. *Colloids Surfaces A Physicochem. Eng. Asp.* 96, 1–46.

(170) Almgren, M., Brown, W., and Hvidt, S. (1995) Self-aggregation and phase behavior of poly(ethylene oxide)-poly(propylene oxide)-poly(ethylene oxide) block copolymers in aqueous solution. *Colloid Polym. Sci.* 273, 2–15.

(171) Hecht, E., Mortensen, K., Gradzielski, M., and Hoffmann, H. (1995) Interaction of ABA Block Copolymers with Ionic Surfactants: Influence on Micellization and Gelation. *J. Phys. Chem.* 99, 4866–4874.

(172) Jeong, B., Bae, Y. H., Lee, D. S., and Kim, S. W. (1997) Biodegradable block copolymers as injectable drug-delivery systems 388, 860–862.

(173) Moghimi, S. M., and Hunter, A. C. (2000) Poloxamers and poloxamines in nanoparticle engineering and experimental medicine. *Trends Biotechnol.* 18, 412–420.

(174) Ivanova, R., Alexandridis, P., and Lindman, B. (2001) Interaction of poloxamer block copolymers with cosolvents and surfactants. *Colloids Surfaces A Physicochem. Eng. Asp.* 183-185, 41–53.

(175) Maskarinec, S. A., and Lee, K. Y. C. (2003) Comparative Study of Poloxamer Insertion into Lipid Monolayers. *Langmuir* 19, 1809–1815.

(176) Frey, S. L., Zhang, D., Carignano, M. A., Szleifer, I., and Lee, K. Y. C. (2007) Effects of block copolymer's architecture on its association with lipid membranes: experiments and simulations. *J. Chem. Phys.* 127, 114904.

- (177) Wu, G., Khant, H. A., Chiu, W., and Lee, K. Y. C. (2009) Effects of bilayer phases on phospholipid-poloxamer interactions. *Soft Matter* 5, 1496.
- (178) Wu, G., and Lee, K. Y. C. (2009) Interaction of poloxamers with liposomes: an isothermal titration calorimetry study. *J. Phys. Chem. B* 113, 15522–31.
- (179) Wu, G., and Lee, K. Y. C. (2009) Effects of poloxamer 188 on phospholipid monolayer morphology: an atomic force microscopy study. *Langmuir* 25, 2133–9.
- (180) Alvarez-Lorenzo, C., Sosnik, A., and Concheiro, A. (2011) PEO-PPO Block Copolymers for Passive Micellar Targeting and Overcoming Multidrug Resistance in Cancer Therapy. *Curr. Drug Targets* 12, 1112–1130.
- (181) Pembouong, G., Morellet, N., Kral, T., Hof, M., Scherman, D., Bureau, M.-F., and Mignet, N. (2011) A comprehensive study in triblock copolymer membrane interaction. *J. Control. Release* 151, 57–64.
- (182) Cheng, C.-Y., Wang, J.-Y., Kausik, R., Lee, K. Y. C., and Han, S. (2012) Nature of interactions between PEO-PPO-PEO triblock copolymers and lipid membranes: (II) role of hydration dynamics revealed by dynamic nuclear polarization. *Biomacromolecules* 13, 2624–33.
- (183) Fusco, S. (2006) Perspectives on: PEO-PPO-PEO Triblock Copolymers and their Biomedical Applications. *J. Bioact. Compat. Polym.* 21, 149–164.
- (184) Redhead, M., Mantovani, G., Nawaz, S., Carbone, P., Gorecki, D. C., Alexander, C., and Bosquillon, C. (2012) Relationship between the affinity of PEO-PPO-PEO block copolymers for biological membranes and their cellular effects. *Pharm. Res.* 29, 1908–18.
- (185) Rabbel, H., Werner, M., and Sommer, J.-U. (2015) Interactions of Amphiphilic Triblock Copolymers with Lipid Membranes: Modes of Interaction and Effect on Permeability Examined by Generic Monte Carlo Simulations. *Macromolecules* 48, 4724–4732.
- (186) Kreuter, J. (2013) Mechanism of polymeric nanoparticle-based drug transport across the blood-brain barrier (BBB). *J. Microencapsul.* 30, 49–54.
- (187) Lee, R. C., River, L. P., Pan, F. S., Ji, L., and Wollmann, R. L. (1992) Surfactant-induced sealing of electroporabilized skeletal muscle membranes in vivo. *Proc. Natl. Acad. Sci. U. S. A.* 89, 4524–8.
- (188) Karplus, M., and McCammon, J. A. (2002) Molecular dynamics simulations of biomolecules. *Nat. Struct. Biol.* 9, 646–52.
- (189) Durrant, J. D., and McCammon, J. A. (2011) Molecular dynamics simulations and drug discovery. *BMC Biol.* 9, 71.
- (190) Adhikari, U., Goliaei, A., Tsereteli, L., and Berkowitz, M. L. (2016) Properties of Poloxamer Molecules and Poloxamer Micelles Dissolved in Water and Next to Lipid Bilayers: Results from Computer Simulations. *J. Phys. Chem. B* DOI: 10.1021/acs.jpcc.5b11448.

- (191) Rossi, G., and Monticelli, L. (2014) Modeling the effect of nano-sized polymer particles on the properties of lipid membranes. *J. Phys. Condens. Matter* 26, 503101.
- (192) Samanta, S., Hezaveh, S., and Roccatano, D. (2013) Theoretical study of binding and permeation of ether-based polymers through interfaces. *J. Phys. Chem. B* 117, 14723–31.
- (193) Nielsen, S. O., Buló, R. E., Moore, P. B., and Ensing, B. (2010) Recent progress in adaptive multiscale molecular dynamics simulations of soft matter. *Phys. Chem. Chem. Phys.* 12, 12401–14.
- (194) Praprotnik, M., Site, L. D., and Kremer, K. (2008) Multiscale simulation of soft matter: from scale bridging to adaptive resolution. *Annu. Rev. Phys. Chem.* 59, 545–71.
- (195) Gutteridge, J. M. C., and Halliwell, B. (1990) The measurement and mechanism of lipid peroxidation in biological systems. *Trends Biochem. Sci.* 15, 129–135.
- (196) Wang, J.-Y., Marks, J., and Lee, K. Y. C. (2012) Nature of interactions between PEO-PPO-PEO triblock copolymers and lipid membranes: (I) effect of polymer hydrophobicity on its ability to protect liposomes from peroxidation. *Biomacromolecules* 13, 2616–23.
- (197) Frisch, M., Trucks, G., Schlegel, H., Scuseria, G., Robb, M., Cheeseman, J., Scalmani, G., Barone, V., Mennucci, B., Petersson, G., Nakatsuji, H., Caricato, M., Li, X., Hratchian, H., Izmaylov, A., Bloino, J., Zheng, G., Sonnenberg, J., Hada, M., Ehara, M., Toyota, K., Fukuda, R., Hasegawa, J., Ishida, M., Nakajima, T., Honda, Y., Kitao, O., Nakai, H., Vreven, T., Montgomery, J., Peralta, J., Ogliaro, F., Bearpark, M., Heyd, J., Brothers, E., Kudin, K., Staroverov, V., Kobayashi, R., Normand, J., Raghavachari, K., Rendell, A., Burant, J., Iyengar, S., Tomasi, J., Cossi, M., Rega, N., Millam, J., Klene, M., Knox, J., Cross, J., Bakken, V., Adamo, C., Jaramillo, J., Gomperts, R., Stratmann, R., Yazyev, O., Austin, A., Cammi, R., Pomelli, C., Ochterski, J., Martin, R., Morokuma, K., Zakrzewski, V., Voth, G., Salvador, P., Dannenberg, J., Dapprich, S., Daniels, A., Farkas, Foresman, J., Ortiz, J., Cioslowski, J., and Fox, D. (2009) Gaussian 09, Revision B.01. *Gaussian 09, Revis. B.01, Gaussian, Inc., Wallingford CT*.
- (198) Reed, A. E., Weinhold, F., Curtiss, L. A., and Pochatko, D. J. (1986) Natural bond orbital analysis of molecular interactions: Theoretical studies of binary complexes of HF, H₂O, NH₃, N₂, O₂, F₂, CO, and CO₂ with HF, H₂O, and NH₃. *J. Chem. Phys.* 84, 5687.
- (199) Berendsen, H., Postma, J., van Gunsteren, W., and Hermans, J. (1981) Interaction models for water in relation to protein hydration. *Intermol. Forces* 331 – 342.
- (200) Poger, D., Van Gunsteren, W. F., and Mark, A. E. (2010) A new force field for simulating phosphatidylcholine bilayers. *J. Comput. Chem.* 31, 1117–25.
- (201) Darden, T., York, D., and Pedersen, L. (1993) Particle mesh Ewald: An N·log(N) method for Ewald sums in large systems. *J. Chem. Phys.* 98, 10089.
- (202) Essmann, U., Perera, L., Berkowitz, M. L., Darden, T., Lee, H., and Pedersen, L. G. (1995) A smooth particle mesh Ewald method. *J. Chem. Phys.* 103, 8577.

- (203) Nosé, S. (1984) A unified formulation of the constant temperature molecular dynamics methods. *J. Chem. Phys.* *81*, 511.
- (204) Hoover, W. (1985) Canonical dynamics: Equilibrium phase-space distributions. *Phys. Rev. A* *31*, 1695–1697.
- (205) Wassenaar, T. A., Pluhackova, K., Böckmann, R. A., Marrink, S. J., and Tieleman, D. P. (2014) Going Backward: A Flexible Geometric Approach to Reverse Transformation from Coarse Grained to Atomistic Models. *J. Chem. Theory Comput.* *10*, 676–690.